Multiple-Device and Multiple-Resonator Low Phase-Noise Microwave Oscillators

by

Jonghoon Choi

A dissertation submitted in partial fulfillment
of the requirements for the degree of
Doctor of Philosophy
(Electrical Engineering)
in The University of Michigan
2007

Doctoral Committee:
       Professor Amir Mortazawi, Chair
       Professor Kamal Sarabandi
       Professor Kim A. Winick
       Associate Professor Michael Flynn

UMI Number: 3276115

INFORMATION TO USERS

The quality of this reproduction is dependent upon the quality of the copy submitted. Broken or indistinct print, colored or poor quality illustrations and photographs, print bleed-through, substandard margins, and improper alignment can adversely affect reproduction.

In the unlikely event that the author did not send a complete manuscript and there are missing pages, these will be noted. Also, if unauthorized copyright material had to be removed, a note will indicate the deletion.

UMI®

UMI Microform 3276115

If we knew what we were doing, it wouldn't be called research

— Albert Einstein

To my wife Unyoung, my daughter Kaylyn, and my son Lucas

Acknowledgments

Concluding my five years in Michigan, there are so many people I would like to thank.

First and foremost, I would like to express my deepest appreciation to my advisor, Professor Amir Mortazawi, for his support, guidance, and encouragement for the past five years. He offered me an opportunity to work on this field despite my lack of background in microwave engineering. Without his trust on my potential and an opportunity he provided, I would not have been an RF/microwave engineer as today. Moreover, his critiques, intriguing questions, and comments led me to delve into critical issues more rigorously and helped me to become a better researcher. I also would like to thank Professor Kamal Sarabandi, Professor Michael Flynn, and Professor Kim Winick for their valuable support, insightful advice and time by serving members of my thesis committee.

I have learned a lot from my friends in my group and enjoyed discussing many research issues with them. I want to thank my group members Ayman Al-Zayed, Ali Tombak, Xin Jiang, Zhang Jin, Lora Schulwitz, Navin Gupta, Jia-Shiang Fu, Xinen Zhu, Meng-Hung Chen, Danial Ehyaie, and Morteza Nick. I have also enjoyed friendship, advice and help from many friends in Radiation Laboratory. I specially thank Pouya Valizadeh and Juseop Lee for helping 1/f noise measurement and filter design. I am grateful to Wonbin Hong and Kate Musgrave for revising my dissertation.

I would like to acknowledge NASA, Korean Ministry of Information and Communication, and the University of Michigan for providing me with the financial support throughout my graduate study. I also owe much to Rogers Corporation, Dielectric Laboratories and Fujitsu for sending me free samples of their products for my circuit design.

I am grateful to my Korean EECS graduate students and church members. Thanks to

iii

their friendship and support, Michigan became my second home town. Occasional gathering with them also helped me to release stress and to be recharged. Last but not the last, I would like to thank my parents Insook and Suyoung, who raised me in God, and my sister Eunju and my brother Jongmin. Their prayer and endless love made my today possible. I am most thankful to my wife, Unyoung for sharing my joy and sorrow throughout my graduate study. Two precious childlen I got in Michigan, my daughter Kaylyn and my son Lucas, you are the reason of my life and a source of my energy.

Table of Contents

List of Tables

List of Figures

x

Abstract

There have been increasing demands for low phase-noise and low-cost microwave frequency sources due to the rapidly growing market for wireless communication systems in the recent years. This thesis demonstrates novel multiple-device and multiple-resonator low phase-noise microwave oscillators with a potential to address the phase-noise requirements of modern communication systems.

The first proposed design methodology is based on high-order resonant circuits. By properly connecting multiple resonators and optimizing coupling relations between those resonators, high-order resonant circuits can be designed to produce higher oscillator Qs compared to the conventional single resonators. This work proposes two new high-order resonant circuits based on the extended resonance technique and multiple-pole filters. The extended-resonance multiple-device oscillator is capable of improving the phase noise as a result of high oscillator Q from cascading of multiple resonant circuits as well as power combining. In multiple-pole elliptic-filter oscillators, high oscillator Qs can be achieved by utilizing group delay peaks formed at the passband edges of the filters. A SiGe HBT extended-resonance oscillator and a SiGe HBT four-pole elliptic-filter oscillator are demonstrated with phase noises of -138 dBc/Hz and -140 dBc/Hz at 1 MHz offset frequency, respectively.

The $1/f$ noise upconversion in push-push and triple-push oscillators has also been studied. Because the 1/f noise upconversion is strongly dependent on the harmonic contents of waveforms, it should be carefully treated in push-push and triple-push oscillators that utilize harmonic components as output signals. The low phase-noise design requirements for minimizing 1/f noise upconversion in such oscillators are presented and the experi-

mental demonstration at C band using MESFET oscillators shows 12-15 dB phase-noise improvement in $1/f^3$ phase noise region.

Chapter 1

Introduction

1.1 Motivation

The last decade has witnessed an exponential growth in wireless communication markets, in the process, accelerating innovations in wireless communication technology. Innovations in this area have not only provided easy access to communication and information through cell phones and wireless LANs but are also opening new possibilities in other areas such as long distance health monitoring in the medical field, remote sensing in the environmental field, etc. Along with their rapid growth, wireless communication systems demand wider bandwidths for high data-rate transmission in multimedia applications. To meet this demand, the development of high-performance wireless transmitter and receiver systems at microwave and millimeter-wave frequencies has accelerated.

Oscillators are among the main building blocks of wireless transceiver systems. In transceiver systems, oscillators generate reference sinusoidal signals for modulation and demodulation. One of the key issues in oscillator design is the minimization of oscillator phase noise, which is generated by noise from both active devices and passive components. Oscillator phase noise in wireless transceivers limits the overall performance of communication systems in a variety of ways. Phase noise directly affects adjacent-channel interference and bit error rate. Phase noise of the local oscillator in a wireless receiver downconverts the adjacent channels into intermediate frequency (IF) thereby limiting a receiver's immunity to nearby interference and jamming signals. Phase noise in a wire-

1

less transmitter can also overwhelm adjacent weak channels. In general, oscillator phase noise compromises the overall capability of communication systems and places stringent requirements on the performance of transceiver building blocks such as the noise figure of low noise amplifiers, the rejection factor of filters and the output power of power amplifiers. Because the number of wireless subscribers and thus, the amount of RF interference continue to increase, modern communication standards demand the highest possible level of phase-noise performance from local oscillators in transceivers.

The design of low phase-noise oscillators faces many challenges at the microwave and millimeter-wave frequencies. The main limiting factor in designing low phase-noise oscillators at these frequencies is the low quality factor of resonators attributable to high conductor and dielectric losses. In current microwave systems, therefore, dielectric resonator oscillators (DROs) are widely employed, given that dielectric resonators (DRs) present high unloaded quality factors. However, DROs still evince several major drawbacks. The main drawback of DROs is their large size as compared to the rest of the oscillator circuit. Further, DROs are not amenable to integration and are unsuitable for mass production because they necessitate fine post-production tuning. Another challenge in designing low phase-noise oscillators stems from the occurrence of low-frequency $1/f$ noise upconversion that significantly degrades spectral purity in the proximity of carrier frequency. This $1/f$ noise upconversion issue is particularly important at microwave frequencies, because common microwave devices such as MESFETs and HEMTs demonstrate poor $1/f$ noise performance.

1.2 Thesis Overview

In response to the above technology needs, this thesis proposes novel low phase-noise microwave oscillators that are compatible with current integrated circuit (IC) technologies. In particular, it focuses on the development of multiple-device and multiple-resonator os-

2
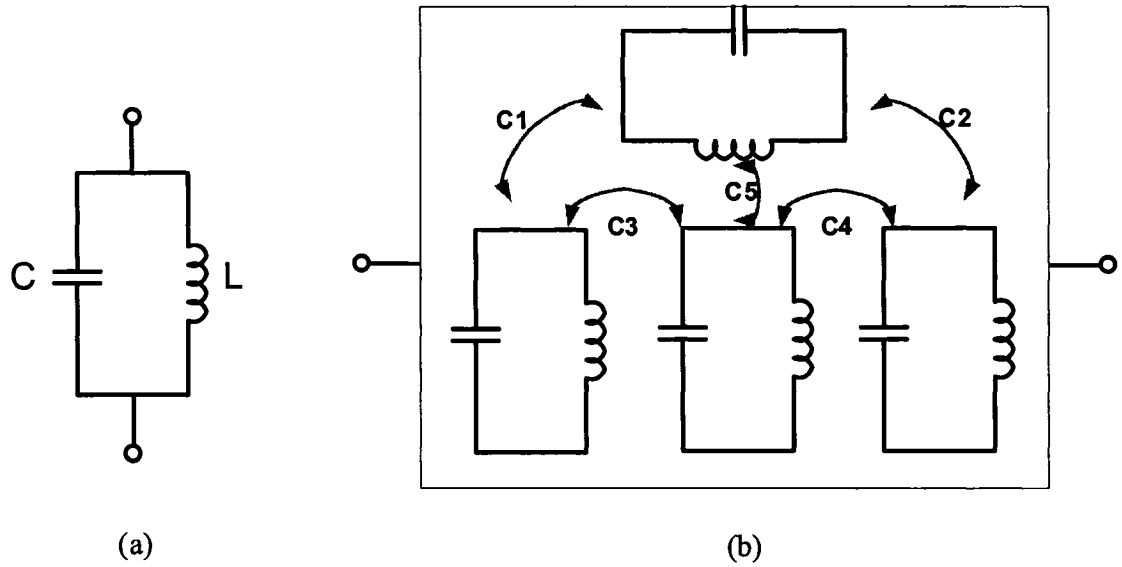
Figure 1.1: (a) Single resonator (b) high-order resonant circuit composed of multiple resonators. C_1 - C_5 represent the coupling coefficients between resonators

cillators to achieve low phase noise. The use of a single resonator limits the achievable oscillator Q based on the resonator technologies used. For instance, conductor and substrate losses in LC or transmission-line resonators limit their achievable Q. Given these limitations, conventional low phase-noise design techniques rely on improving conductor and dielectric losses in single resonators by manipulating circuit layout and integration techniques. This work investigates high-order resonant circuits capable of overcoming the fundamental limit on quality factor posed by current IC technologies. High-order resonant circuits are composed of multiple resonators thus providing more than two poles and zeros while single resonators possess only two poles. By optimal design of a coupling mechanism between multiple resonators, the high-order resonant circuit characteristics that multiple-device and multiple-resonator oscillators offer, can significantly enhance the overall oscillator Q.

Another contribution of this work is investigation of low phase-noise design techniques for reducing 1/f noise upconversion in push-push and triple-push multiple-device oscillators. The low phase-noise design of push-push and triple-push oscillators is complex

3

because the 1/f noise upconversion is strongly dependent on the harmonic contents of oscillator waveforms and in push-push and triple-push oscillators, harmonic components are used as output signals. This is the first work that takes advantage of naturally generated harmonic waveforms in such oscillators to optimize the phase noise performance. The organization of the thesis is as follows.

Chapter 2 gives an introduction to oscillator phase noise, starting by the definition of phase noise and then moving on describing the effect of phase noise on communication and radar systems. Two existing phase-noise models essential to understanding the design techniques are presented.

Chapter 3 reviews other reported multiple-device and multiple-resonator oscillators emphasizing on their phase-nose characteristics. It covers multiple-device power-combining oscillators, mutually coupled oscillators, series-cascaded multiple-device and multiple-resonator oscillators, and multiple-pole filter oscillators.

Chapter 4 presents a novel power-combining multiple-device oscillator with low phase-noise performance. This oscillator is based on the extended-resonance power-combining circuit which resembles a ladder-type filter structure. For low phase-noise design, the extended resonance circuit is analyzed and the design methodologies are presented. For experimental validation, C-band HEMT and X-band SiGe HBT multiple-device extended-resonance oscillators are demonstrated.

Chapter 5 presents a new type of high-order resonant circuits for the design of low phase-noise oscillators. This circuit is based on elliptic-response bandpass filters that provide high group-delay peaks at their passband edges. The filter optimization for low phase-noise design is presented. The simulation and measurement results for a 9 GHz SiGe HBT oscillator employing a four-pole bandpass filter are then given and discussed.

Chapter 6 discusses the effect of waveform symmetry on phase noise in push-push and triple-push oscillators based on a time-variant phase-noise theory. Push-push and triple-push oscillators are frequency doubling and tripling multiple-device oscillators utilizing

4

the second and third harmonic components, respectively. The effect of harmonic power levels on 1/f noise upconversion is analyzed and the design requirements for minimizing 1/f noise upconversion are suggested and experimentally verified.

Finally, Chapter 7 concludes the thesis with the summary of work presented herein and suggests some future works regarding IC applications of the proposed techniques at millimeter-wave frequencies.

Chapter 2

Phase Noise Fundamentals

The spectral purity of an oscillator can be degraded by random fluctuations of its amplitude, frequency, and phase. That is, noise generated in both the active device and passive components modulates the signal produced by the oscillator. The sources of random sideband noise in an oscillator include thermal noise, shot noise, and flicker (1/f) noise, all of which result in amplitude and phase noise. In general, the output of a noisy oscillator is represented by:

$$v_t = (A + a(t)) \cdot cos(\omega_0 t + \phi(t)) \tag{2.1}$$

where A and ω_0 are deterministic amplitude and frequency and $a(t)$ and $\phi(t)$ are random amplitude and phase noise, respectively. In practice, amplitude noise can be substantially attenuated by use of the amplitude-restoring mechanism of oscillators. When an oscillator has large quantity of amplitude noise, that noise can easily be eliminated by placing a limiter at the output of the oscillator. However, there is no mechanism or circuit that eliminates phase noise, which therefore plays a dominant role in the spectral purity performance of oscillators. As shown in Fig. 2.1, the existence of phase noise causes the frequency spectrum of a noisy oscillator output to broaden in the vicinity of the carrier frequency, while the frequency spectrum of an ideal oscillator output is represented by a delta function.

Normally, phase noise is measured as the ratio of noise power (P_n) in one sideband contained in a specified bandwidth (B) at an offset frequency $(\Delta \omega)$ when compared to the carrier output power herein referred to as (P_s) in Fig. 2.1(b). Such a power ratio is usually

6

ω_o

(a)

Power

P_s

P_n

B

ω_o $\omega_o + \Delta\omega$ Frequency

(b)
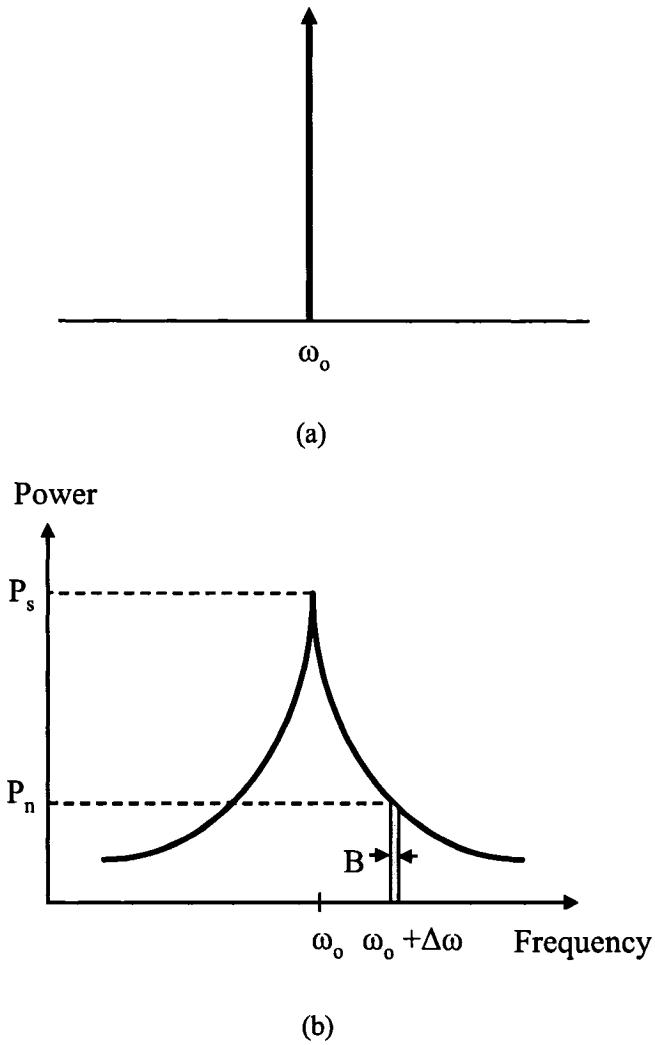
Figure 2.1: Frequency spectrum in (a) noiseless (b) noisy oscillators

expressed as decibels below carrier per Herz (dBc/Hz).

2.1   Effect of Phase Noise on Communication and Radar Systems

Phase noise from the local oscillators in radio receivers and transmitters sets fundamental limits on the performance of the communication system. Fig. 2.2 shows a block diagram of a typical front-end transceiver system composed of an antenna, a duplexer, a low noise amplifier (LNA), a power amplifier (PA), mixers, and local oscillators. When a

7

strong interfering signal is located close to a desired signal in receivers, as shown in Fig. 2.3(a), phase noise of the local oscillators downconverts the strong nearby channel to the intermediate frequency (IF) of the system. The desired signal is thus subject to interference by the phase noise from the adjacent signal, which degrades its signal-to-noise ratio (SNR) in an effect called reciprocal mixing. In RF transmitters, the phase noise of a strong transmitting signal is capable of overwhelming the nearby weak channels, as shown in Fig. 2.3(b).

Phase noise also limits the sensitivity and resolution of radar systems. To detect the velocity of moving targets, the correct determination of the received signal frequency is vital in Doppler radar systems. As target distance changes relative to the radar, the received signal frequency varies linearly. Phase noise contamination can disrupt a received signal to the point that a target located within clutter can go undetected. Therefore, phase noise of the local oscillators in radar systems degrades the velocity detection capability. Further, low phase-noise performance is required to improve the distinguishing of small targets from adjacent large targets in radar systems.
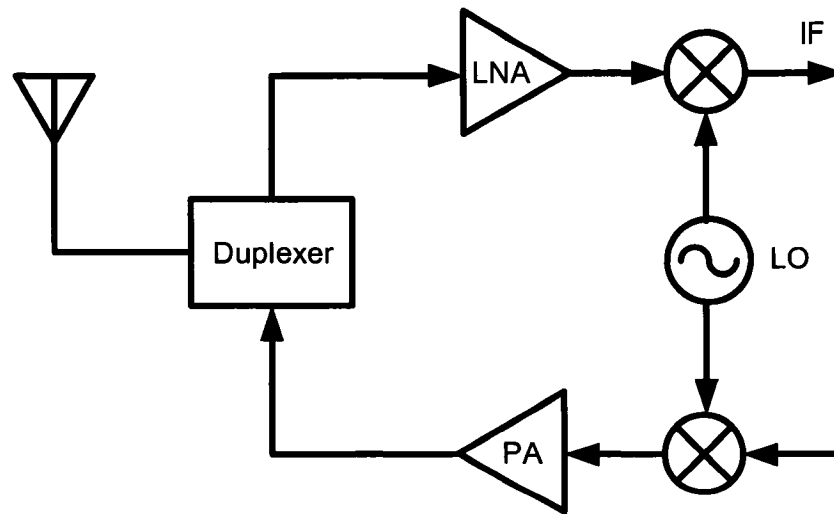
Figure 2.2: Block diagram of a typical front-end transceiver system

8
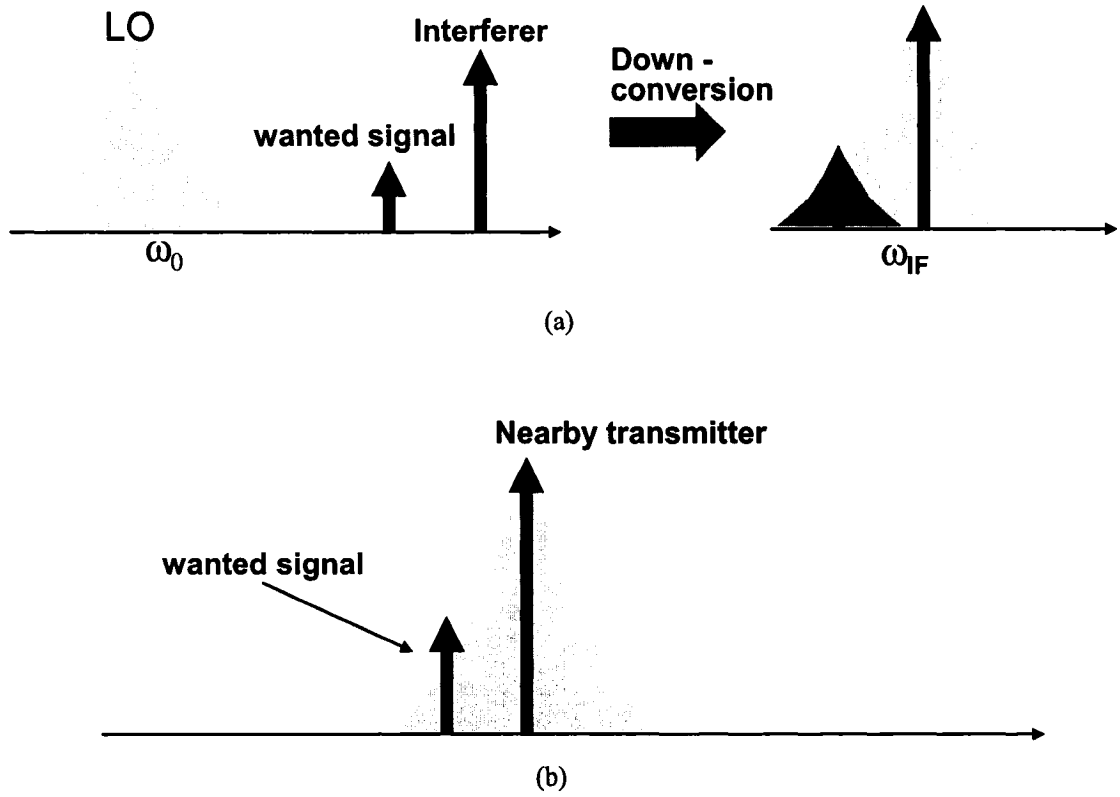
Figure 2.3: Effect of phase noise in (a) receivers and (b) transmitters

2.2 Review of the Existing Phase Noise Models

In explanation of the behavior of phase noise, several mathematical models should be addressed. Here, two existing phase noise models including Leeson's model and Hajimiri's model will be discussed. These models are employed to justify the low phase noise design techniques proposed in this thesis.

2.2.1 Leeson's Phase Noise Model

The most general model for phase noise in oscillators was described by Leeson [3]. This model, based on a feedback oscillator as shown in Fig. 2.4(b), is constructed under the assumption that the oscillator is a linear and time-invariant (LTI) system. When noise n(t) is added in the oscillator system as shown in Fig. 2.4(a), the noise generates the phase

9

uncertainty, represented by:

$$\Delta\theta(t) = atan\left(\frac{n(t)}{v(t)}\right) \approx \frac{n(t)}{v(t)} \tag{2.2}$$

The phase uncertainty $\Delta\theta(t)$ arises from two components. The first component is white additive noise at frequencies in the area of the oscillation frequency and the second is multiplicative noise that has been translated from noises, including low frequency $1/f$ noise, at other frequencies. If only white additive noise is considered, the power spectrum of the phase deviation is represented by:

$$S_{\Delta\theta}(\omega) = \frac{\overline{n(t)^2}}{\overline{v(t)^2}} = \frac{FkT}{P_s} \tag{2.3}$$

where F is the effective noise figure of the amplifier, K is Boltzmann's constant, T is the absolute temperature, and P_s is the signal power. By taking into account the effect of low frequency $1/f$ noise, the above equation is modified into:

$$S_{\Delta\theta}(\Delta\omega) = \frac{FkT}{P_s} + \frac{\alpha}{\Delta\omega} \tag{2.4}$$

where α is a constant determined by the variation of 1/f noise and $\Delta\omega$ is an offset frequency. If only the phase parameter is considered, the oscillator feedback model in Fig. 2.4(b) is convertible to the phase-feedback system as shown in Fig. 2.4(c). In the phase-feedback model, phase uncertainty at the input $\Delta\theta(t)$ will determine output phase noise $\Delta\phi(t)$ by means of the overall transfer function. The resonator is modeled as a low-pass filter, and the transfer function is represented by:

$$H(\Delta\omega) = \frac{1}{1 + j2Q_L\dfrac{\Delta\omega}{\omega_0}} \tag{2.5}$$

where ω_0 is the oscillation frequency and Q_L represents the loaded quality factor of the resonator. The transfer function between input phase uncertainty and output phase noise is

10
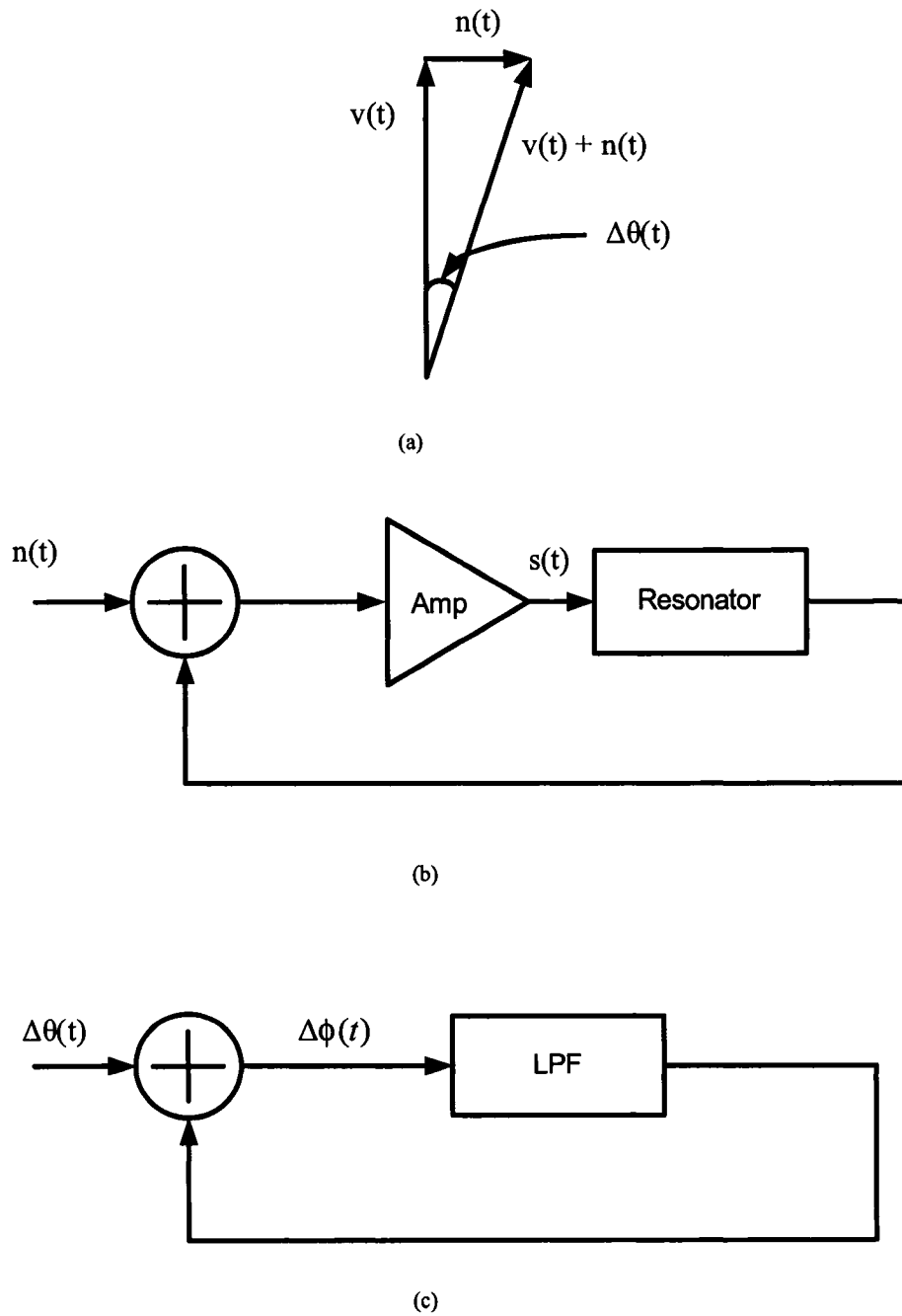
Figure 2.4: (a) Vector representation for the relationship between the signal, the added noise and the induced phase deviation (b) feedback oscillator model (c) Leeson's phase-feedback model

11

represented by:

$$\frac{\Delta\phi}{\Delta\theta} = \frac{1}{1 - H(\Delta\omega)} = 1 + \frac{\omega_0}{j2Q_L\,\Delta\omega} \qquad (2.6)$$

The power spectral density for the output phase noise becomes:

$$S_{\Delta\phi}(\Delta\omega) = \left[1 + \left(\frac{\omega_0}{2Q_L\Delta\omega}\right)^2\right] S_{\Delta\theta}(\Delta\omega) \qquad (2.7)$$

Finally, the phase noise is represented by:

$$L(\Delta\omega) = \frac{S_{\Delta\phi}(\Delta\omega)}{2} = \frac{FkTR}{2P_s}\left[1 + \left(\frac{\omega_0}{2Q_L\Delta\omega}\right)^2\right]\left(1 + \frac{\Delta\omega_{1/f^3}}{\Delta\omega}\right) \qquad (2.8)$$

where $\Delta\omega_{1/f^3}$ is the $1/f^3$ phase noise corner frequency. The above representation of Leeson's formula is graphically depicted as shown in Fig. 2.5. The effect of $1/f$ noise is dominant in the proximity of the carrier frequency, which leads to the decrease of phase noise with offset frequency at 9 dB/octave up to $1/f^3$ corner frequency. From $1/f^3$ corner frequency to $\omega_0/2Q$, phase noise shows the decreasing slope of 6 dB/octave. Outside $\omega_0/2Q$, the phase noise spectrum flattens out.

Leeson's model also suggests the following methods of reducing the phase noise of an oscillator. The methods include:

1. Use of a high Q resonator given that phase noise is inversely proportional to the square of Q_L.

2. Increase in the signal output power.

3. Selection of an active device producing low flicker noise and low noise figure

Osillator Q and Insertion Loss

Leeson's formula (2.8) employs the term loaded Q "Q_L", the definition of which is critical to understanding the design techniques presented in the thesis. In a resonant circuit,

12
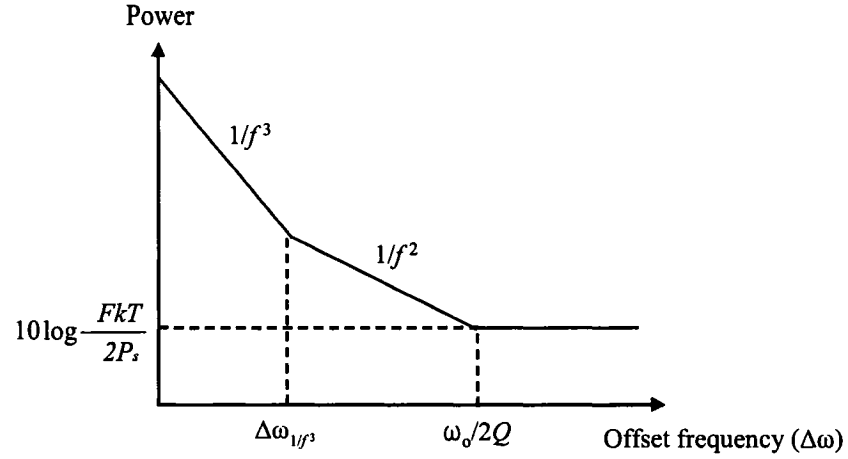
Power

Figure 2.5: Phase noise spectrum

the definition of the loaded Q is represented by:

$$Q_L = \omega_0 \frac{W_m + W_e}{P_l} \tag{2.9}$$

where W_m and W_e are the average magnetic and electric energy stored in the circuit and P_l is the average dissipated power per single cycle. This quantity shows the ratio of energy storage to energy loss in one cycle. Generally, resonator Q can be increased by reducing resonator loss.

However, a definition of Q differing from (2.9) must be used in the phase noise calculation based on Leeson's formula. To explain the definition of the oscillator Q, a simple LC feedback oscillator is considered as shown in Fig. 2.6(a) in which the deterministic phase of the amplifier is zero and the random phase fluctuation of the amplifier is denoted as $\Delta\phi_{amp}$. Fig. 2.6 shows the magnitude $H(j\omega)$ and phase $\phi_{res}(j\omega)$ of the frequency response for two resonators with different Q values. To satisfy the oscillation condition, the oscillator loop must maintain a 360° phase delay.

$$\phi_{res} + \Delta\phi_{amp} = 360° \tag{2.10}$$

Because the device noise in the amplifier results in random phase fluctuation $\Delta\phi_{amp}$, the

13

phase of the resonator is accordingly disturbed to sustain the above oscillation condition (2.10) as shown in Fig. 2.6(b). The fluctuation in the resonator phase results in the oscillation frequency disturbance depending on the phase slope of the resonator. Since the phase slope of resonator 1 is sharper than that of resonator 2, the carrier frequency of the oscillator employing resonator 1 fluctuates over a smaller range of frequency resulting in lower phase noise, as compared to the oscillator employing resonator 2. This implies that the important mechanism in determining phase noise is not the resonance sharpness in magnitude but the sharpness of the phase slope. For instance, very long fiber delay lines employed in optoelectronic microwave oscillators provide broad magnitude response but high group delay. Therefore, such oscillators show very low phase noise performance (-140 dBc/Hz at 10 kHz offset frequency at 10 GHz in [10])

The definition of the oscillator Q employed in Leeson's formula is therefore achieved by manipulating the phase of the open-loop transfer function [6]. An open-loop transfer function is obtained by breaking one point of the feedback loop of an oscillator as shown in Fig. 2.6(a). By differentiating the phase of the open-loop transfer, the oscillator loaded Q is determined to be:

$$Q_{osc} = \frac{\omega_0}{2} \cdot \left| \frac{d\phi(\omega)}{d\omega} \right| \qquad (2.11)$$

where ω_0 is the oscillation frequency and $\phi(\omega)$ is the phase of the open-loop transfer function. The above equation shows that the oscillator loaded Q is proportional to the absolute value of group delay, indicating that group delay is an important performance measure for phase noise.

It is worth mentioning that in oscillators where a single resonance is not clearly identified such as oscillators with high-order resonant circuits and inductor-less ring oscillators, the two definitions of Q shown in (2.9) and (2.11) result in different phase-noise estimations, while for oscillators employing a single resonator, the two definitions provide the same results in phase-noise calculation. The use of (2.9) for the design of low phase-noise

14
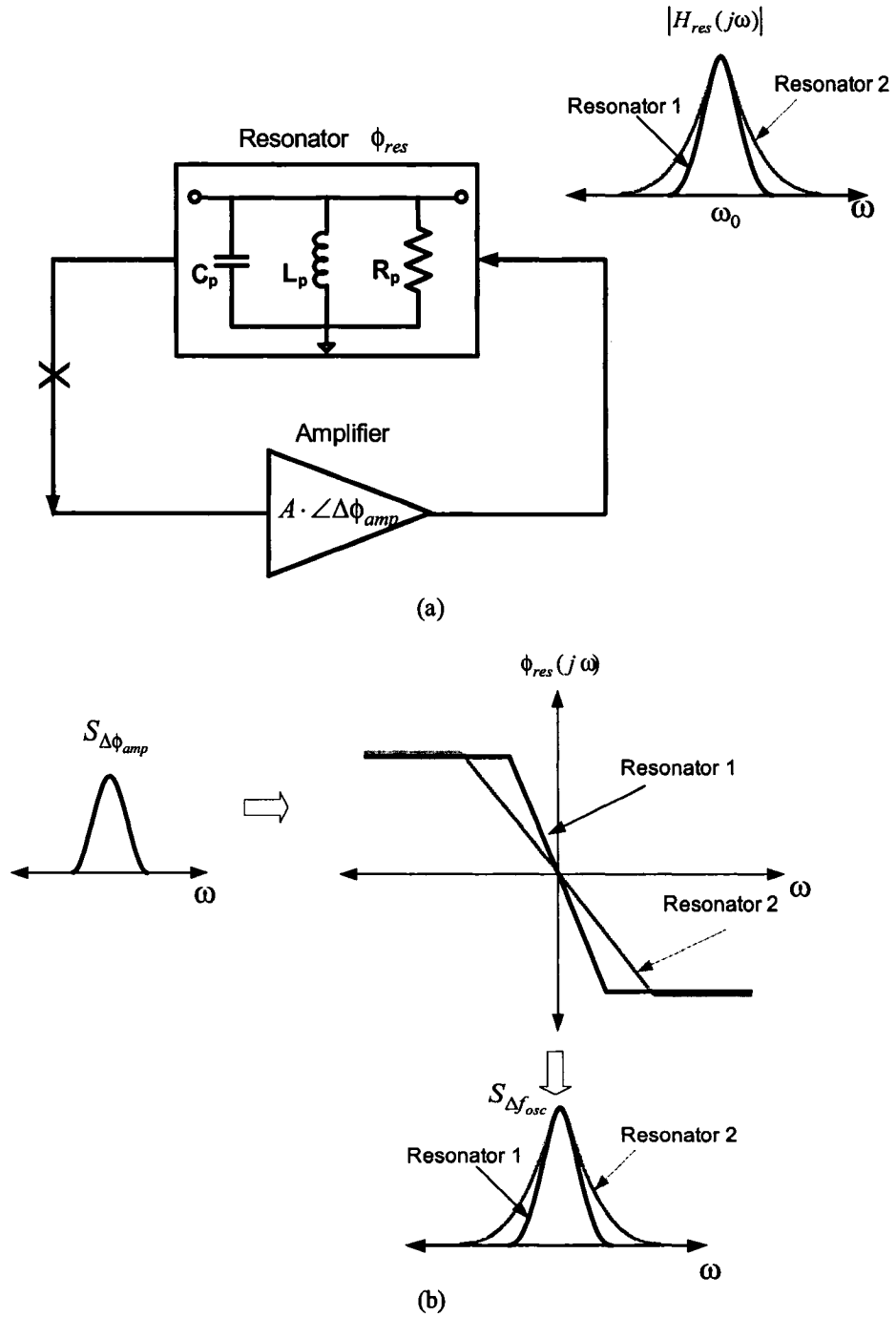
Figure 2.6: (a) Feedback LC oscillator (b) Conversion of the amplifier's phase fluctuation to oscillation frequency fluctuation
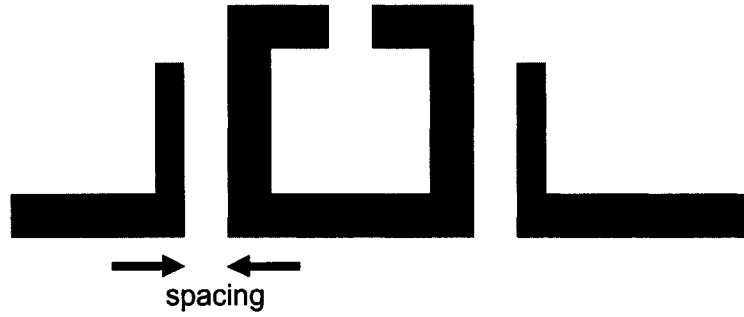
Figure 2.7: Microstrip-line resonator loaded with transmission lines

multiple-device and multiple-resonator oscillators can produce erroneous results.

Along with group delay, the insertion loss of microwave resonators constitutes another important parameter in determining phase noise in feedback oscillators. For certain microwave resonators such as dielectric and microstrip-line resonators, group delay and insertion loss are mutually coupled parameters depending on loading. For example, both group delay and insertion loss increase as the spacing between the microstrip-line resonator and the loaded transmission line increases, as shown in Fig. 2.7. It is therefore important to consider two quantities simultaneously for low phase-noise design. As the insertion loss of the resonator IL increases, the signal power decreases with the effect of degrading phase noise. Because phase noise is inversely proportional to the signal power, phase noise is proportional to the insertion loss of the resonator [8]. Based on this fact, phase-noise figure of merit (PNFOM) proportional to phase noise is defined in the dissertation as:

$$PNFOM(dB) = IL(dB) - 20 \cdot log(Q_{osc}) \qquad (2.12)$$

In the subsequent chapters, PNFOM is employed as a performance measure for the low phase-noise design of multiple-device and multiple-resonator oscillators.

16

2.2.2 Hajimiri's Phase Noise Model

Although Leeson's phase noise model provides valuable insights into oscillator designs from the engineering perspective, it cannot explain several phase noise phenomena including upconversion of $1/f$ noise and downconversion of noise from the harmonically related frequencies to the carrier frequency. To overcome this limitation, A. Hajimiri and T. Lee proposed a more accurate phase noise model [11] based on the time-variant property of an oscillator. To understand the time-variant property, an impulse current should first be injected into an ideal LC oscillator, as shown in Fig. 2.8(a). The injected impulse current perturbs the voltage across the capacitor by:

$$\Delta V = \frac{\Delta q}{C_{tot}} \qquad (2.13)$$

where Δq is the total charge injected by the impulse current and C_{tot} is the total capacitance at that node. When the impulse current is injected at the peak of the voltage signal, the amplitude changes but the excess phase does not change as shown in Fig. 2.8(b). Conversely, the amplitude does not change but the excess phase shifts when the impulse current is injected at the zero crossing of the voltage signal as shown in Fig. 2.8(c). In an actual oscillator, a small amount of amplitude disturbance can be restored by means of the amplitude-limiting mechanism. Thus the amplitude perturbation disappears after several oscillation cycles are completed. However, the excess phase shift resulting from the impulse current persists and settles permanently into a steady state. The above phenomena indicate that conversion from noise to phase noise is time variant in oscillators. Based on its time-variant property, an oscillator system can be modeled as a transfer function with an impulse current as its input and the excess phase as its output, as shown in Fig. 2.9. The impulse response for the excess phase can be represented by:

17
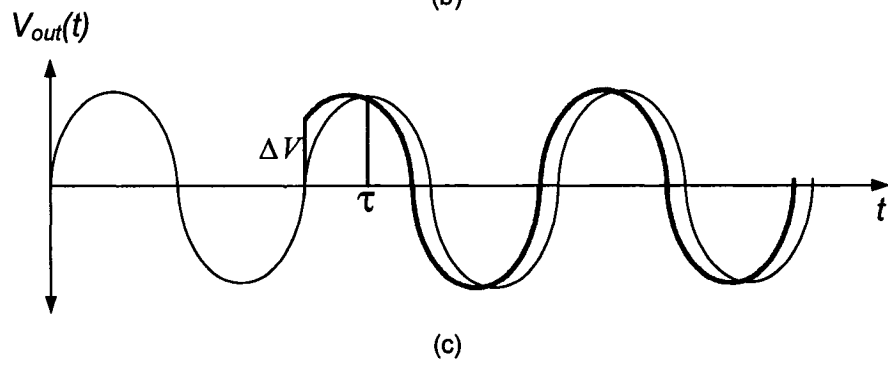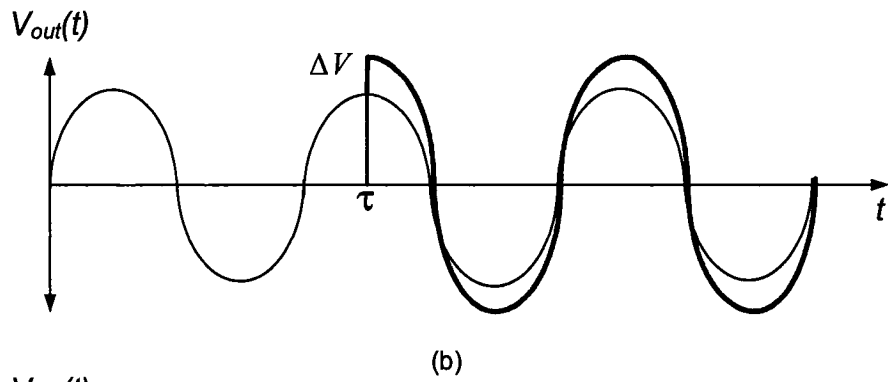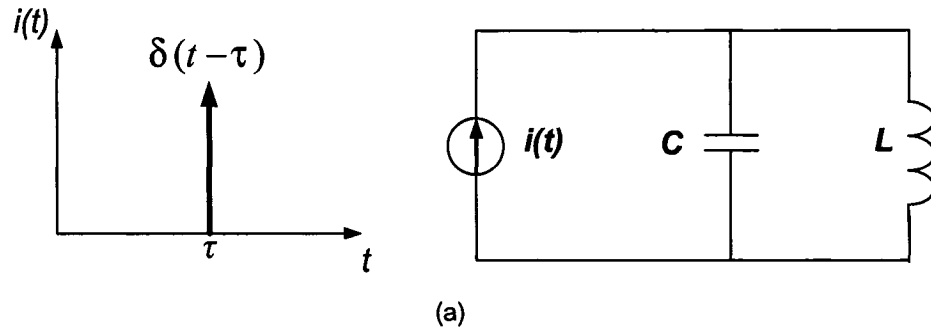
Figure 2.8: Impulse response of an LC oscillator
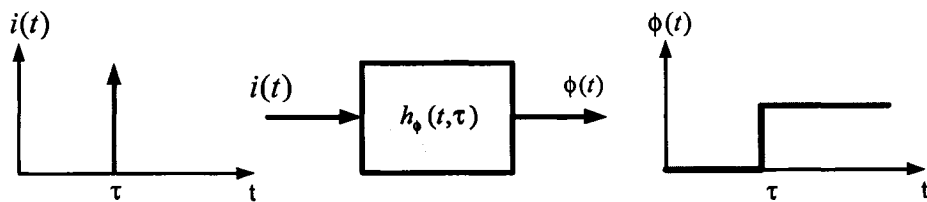
Figure 2.9: Phase impulse response model

18

$$h_\phi(t,\tau) = \frac{\Gamma(\omega_0\tau)}{q_{max}} \cdot u(t - \tau) \qquad (2.14)$$

where u(t) is the unit step function, q_{max} is the maximum charge displacement across the capacitor on the node, and $\Gamma(x)$ is the impulse sensitivity function (ISF). The ISF is a dimensionless function that indicates the amount of phase perturbation occurring when the impulse current is injected at time $t = \tau$. The ISF can be expressed in a Fourier series form represented by (2.15), because it is a periodic function dependent on the oscillation waveform.

$$\Gamma(\omega_0\tau) = \frac{c_0}{2} + \sum_{n=1}^{\infty} c_n \cdot \cos(n\omega_0\tau + \theta_n) \qquad (2.15)$$

where the c_n terms are real-valued coefficients and θ_n is the phase of the nth harmonic. Using (2.14) and (2.15), the output excess phase is represented by

$$\begin{aligned}
\phi(t) &= \int_{-\infty}^{\infty} h_\phi(t,\tau) i(\tau) d\tau \\
&= \frac{1}{q_{max}} \left[\frac{c_0}{2} \int_{-\infty}^{t} i(\tau) d\tau + \sum_{n=1}^{\infty} c_n \int_{-\infty}^{t} i(\tau)\cos(n\omega_0\tau + \theta_n) d\tau \right] \qquad (2.16)
\end{aligned}$$

Based on the above derivation, the final form of phase noise in $1/f^2$ region is represented by:

$$L(\Delta\omega) = 10 \, log \left(\frac{\Gamma_{rms}^2}{2q_{max}^2} \cdot \frac{\overline{i_n^2}/\Delta f}{\Delta\omega^2} \right) \qquad (2.17)$$

where Γ_{rms} is the root mean square (rms) value of the ISF. The phase noise in $1/f^3$ region is represented by:

$$L(\Delta\omega) = 10 \, log \left(\frac{c_0^2}{8q_{max}^2} \cdot \frac{\overline{i_n^2}/\Delta f}{\Delta\omega^2} \cdot \frac{\omega_{1/f}}{\Delta\omega} \right) \qquad (2.18)$$

19
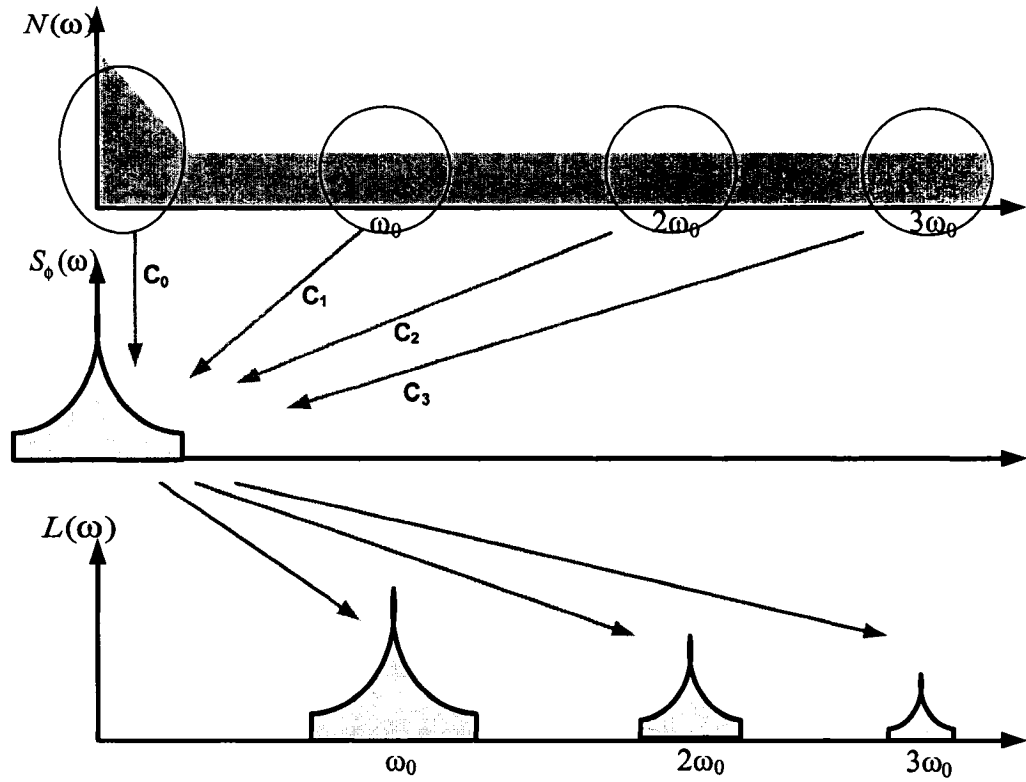
Figure 2.10: Conversion process of noise to phase noise

where $\omega_{1/f}$ is the device $1/f$ noise corner frequency.

Based on (2.16), the conversion process of noise to phase noise in frequency domain is shown in Fig. 2.10. The noise components in the vicinity of DC, the fundamental frequency, and the harmonic frequencies are multiplied by the corresponding Fourier coefficients of the ISF and then added into the output excess noise. The output excess noise is then transformed into the phase noise spectrum.

Hajimiri's time-variant model provides valuable insight into low phase-noise design techniques that Leeson's LTI model fails to provide. In oscillators, certain noise sources periodically change. For instance, since shot noise in BJT devices and white noise in FET devices are functions of periodic bias currents, they have a cyclostationary property. As previously described, oscillators have both noise sensitive and insensitive moments in an oscillation cycle; by concentrating majority of noise power on the least sensitive mo-

20

ment in the oscillation cycle, the contribution of active device noise to phase noise can be significantly reduced. Another design suggestion in Hajimiri's model is to create the waveform symmetry for suppressing 1/f noise upconversion. Given that suppression of 1/f noise upconverion is a major topic of Chapter 6, it will be extensively treated there.

Chapter 3

Overview of Multiple-Device and Multiple-Resonator Oscillators

Generally, oscillators are designed employing one device and one resonator [6]. However, several oscillator performance measures including phase noise, output power, tuning range, and high operation frequency can be improved by employing multiple devices and resonators. In this chapter, several types of multiple-device and multiple-resonator oscillators are discussed with reference to their phase noise characteristics.

3.1 Power-Combining Oscillators

High-power frequency sources are required in certain communication and radar applications [12]. At microwave and millimeter-wave frequencies, an individual solid-state active device possesses limited ability to produce high output power [13]. To attain high microwave power levels, a high-power oscillator can be constructed by combining the powers derived from several devices.

One representative power-combining oscillator is the resonant cavity power-combining oscillator, as first demonstrated at X-band in 1971 by Kurokawa and Magalhaes [15]. Fig. 3.1(a) presents the schematic of a resonant-cavity oscillator. Each IMPATT diode is mounted at the end of the coaxial lines, which are coupled to the sidewalls of the waveguide cavity. In this manner, the negative resistance presented by the IMPATT diodes compensates the load resistor, which satisfies the oscillation condition.

22
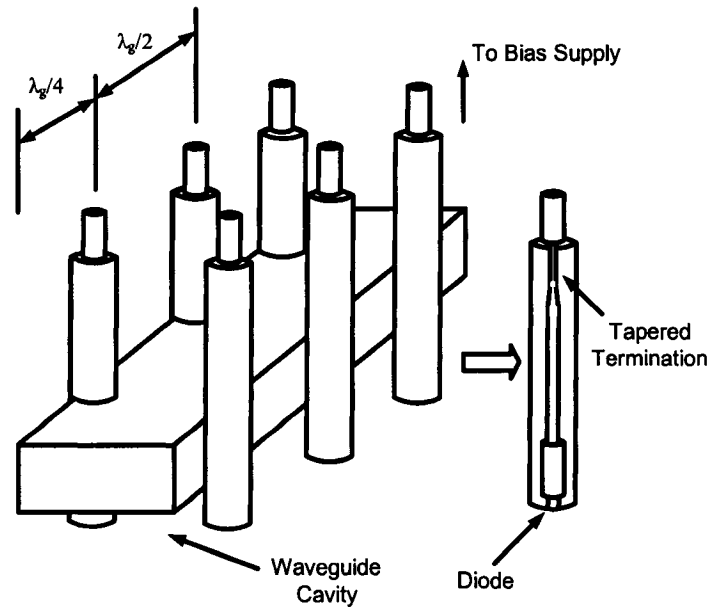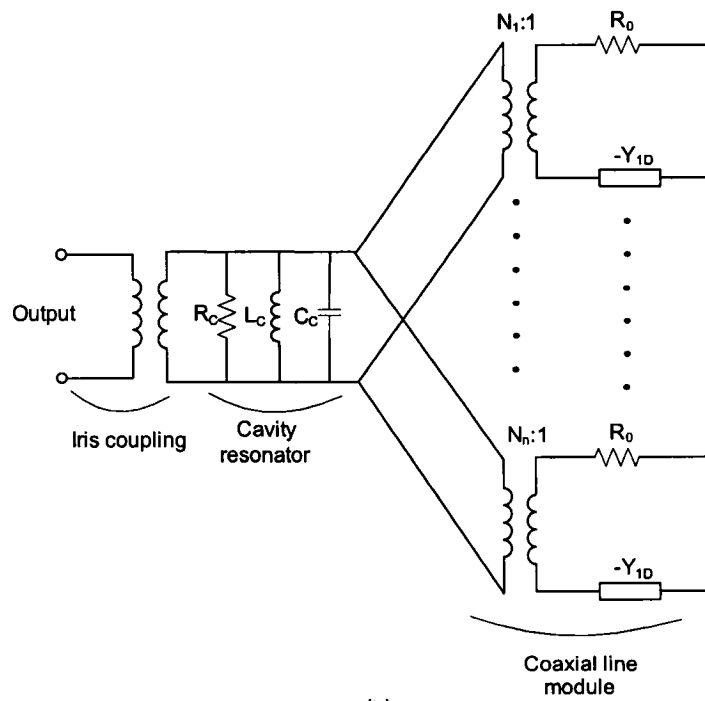
Figure 3.1: (a) Single-cavity multiple-device oscillator (b) equivalent circuit of the single-cavity multiple-device oscillator

23
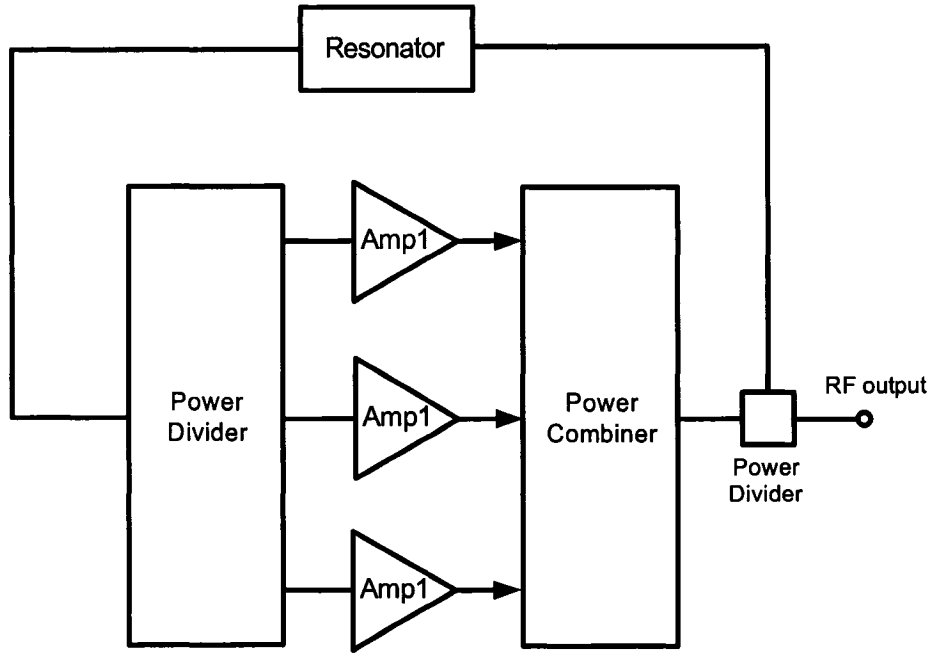
Figure 3.2: Power-combining oscillator composed of multiple amplifiers and one resonator

The equivalent circuit of the resonant-cavity oscillator is shown in Fig. 3.1(b). R_c, L_c, and C_c represent the equivalent circuit parameters of the cavity resonator and N_n represents the coupling coefficient between the cavity resonator and the nth coaxial line. Noise analysis based on the equivalent circuit model indicates that amplitude and phase noise are both inversely proportional to the number of devices N [16].

Another type of power-combining oscillators is shown in Fig. 3.2, in which the oscillator is composed of a resonator and multiple amplifiers. Using a hybrid power-divider and -combiner, multiple amplifiers are connected in a shunt configuration. The advantage of this circuit topology is that it provides isolation between amplifiers, minimizing device interaction and instability problems due to multiple-device operation [13]. In these types of oscillators, the carrier powers from multiple amplifiers are coherently added. However, the noise powers from multiple devices are not added constructively because the noise sources of multiple devices are uncorrelated. The N-device power-combining oscillator thus shows N times phase-noise improvement as compared to a single-device oscillator [14].

24

3.2 Mutually Coupled Oscillators

Oscillator injection locking is accomplished by applying a small signal to a free-running oscillator, provided that the frequency of the small signal is close enough to the frequency of the free-running oscillator [17]. The output phase of an injection-locked oscillator shown in 3.3 is determined by Adler's equation as follows.

$$\frac{d\phi}{dt} = \omega_0 - \omega_{inj} + \frac{A_{inj}}{A_0}\frac{\omega_0}{2Q}\,sin(\phi_{inj} - \phi_0) \tag{3.1}$$

where A_0 and ϕ_0 are amplitude and phase of the free-running oscillator, and Q is the quality factor of the free-running oscillator. At a steady state $(d\phi/dt = 0)$, the free-running oscillator achieves synchronization with the injected signal, and the phase difference between two signals becomes:

$$\Delta\phi = \phi_{inj} - \phi_0 = sin^{-1}(\frac{\omega_{inj} - \omega_0}{\Delta\omega_m}) \tag{3.2}$$

where

$$\Delta\omega_m = \frac{A_{inj}}{A_0}\frac{\omega_0}{2Q} \tag{3.3}$$

The above equation shows that the output phase of the free-running oscillator is adjustable to a new phase depending on the amplitude and frequency of an injected signal. It is further shown that the injection-locking phenomenon is only possible when the injected signal frequency lies within the locking bandwidth $\Delta\omega_m$.

By means of injection-locking of a free running oscillator to a low phase-noise and low-power source, the free-running frequency can be locked to the injected signal frequency, thereby improving both its frequency stability and phase noise [18]. Another scheme based on the injection-locking phenomena is to mutually synchronize several oscillators. By constructing appropriate coupling networks between oscillators, the signals of individual oscillators can be mutually injected into each other, thereby synchronizing the entire oscil-

25

Free-running
oscillator

$$A_0 \cos(\omega_0 t + \phi_0)$$

Injected Signal

$$A_{inj} \cos(\omega_{inj} t + \phi_{inj})$$
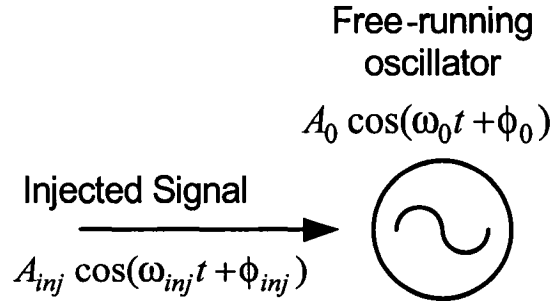
Figure 3.3: Injection-locked oscillator

(a)

(b)
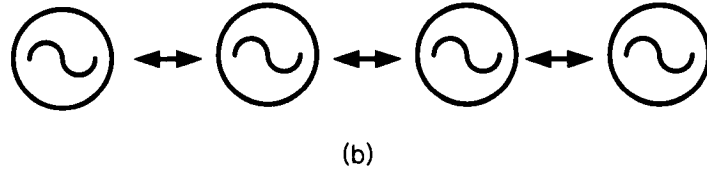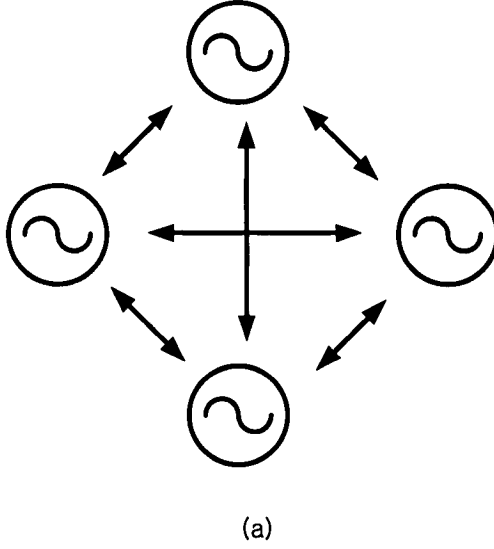
Figure 3.4: (a) Globally coupled oscillator array (b) bilaterally coupled oscillator array

lator array. This synchronization property of the inter-injection locked oscillator array can be used to advantage for power-combining and phased array beam-steering applications [18]. Fig. 3.4 shows two coupling topologies of N individual oscillators, including global and nearest-neighbor coupling configurations.

After mutual synchronization, the phase noise of each oscillator in the N-coupled oscillator array shows 1/N phase noise improvement when compared to that of a single free-

26
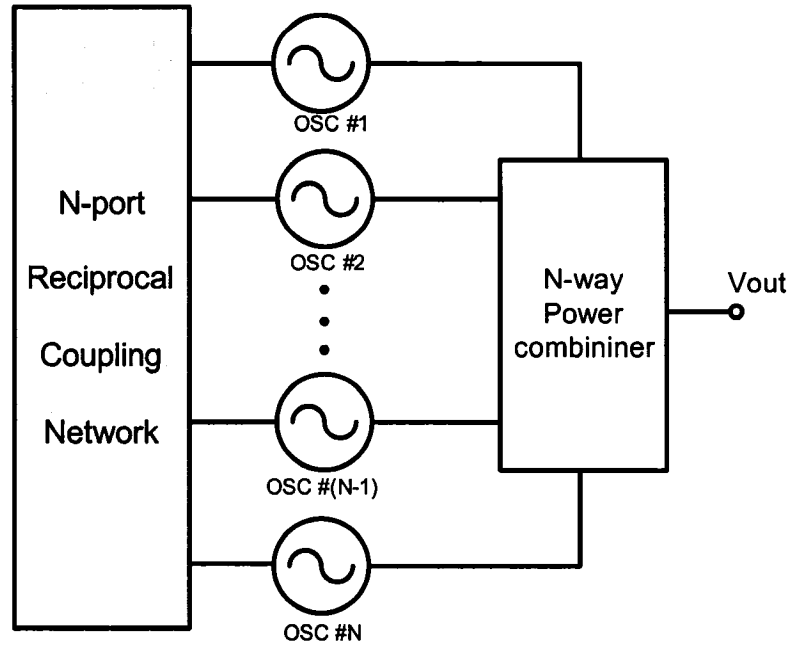
Figure 3.5: Block diagram of an N-coupled power-combining oscillator

running oscillator for the frequency offsets within the locking bandwidth. Inter-injection locking does not affect the phase noise of the oscillator array outside the locking range.

The phase noise of the mutually coupled oscillator should be considered after power combining. Fig. 3.5 shows N mutually coupled oscillators, where individual oscillators are mutually synchronized by injection locking through the N-port reciprocal coupling network. The outputs of each oscillator are then coherently combined with lossless power-combining techniques such as N-way hybrid combiner and quasi-optical techniques. Although in this system the N-port coupling network improves phase noise by 1/N, the N-way power combining does not contribute to further phase noise reduction. The phase noise of the combined output signal is therefore reduced to 1/N compared to a single free-running oscillator. This is due to the correlation between the phase noise components of the individual oscillators resulting from inter-injection locking.

27

3.3 Series-Cascaded Multiple-Device and Multiple-Resonator Oscillators

The oscillator loop group delay is a dominant factor in determining the phase noise, as described in Chapter 2. One method of increasing the loop group delay is to cascade several amplifiers and resonators. The schematic of a series cascaded oscillator composed of four amplifiers and resonators is shown in Fig. 3.6. Each output is separately extracted from one unit cell and then combined by means of a power combiner. This circuit topology is demonstrated with a 640 MHz oscillator employing SAW resonators [21]. By cascading four unit cells, the oscillator loop group delay increases by a factor of four, resulting in 12 dB phase noise improvement. However, because the four noise sources from the four amplifiers increase the noise power level by a factor of four, the phase noise degrades by 6 dB in comparison to a single oscillator. As a result, each RF output of the series cascaded oscillator shows 1/N phase noise reduction. When the phase noise of the power-combined output from four RF outputs is considered, the phase noise remains 1/N of a single oscillator due to the correlation of the phase noise components of the individual outputs. Therefore, the phase noise of the power-combined output signal shows similar 1/N phase noise reduction.
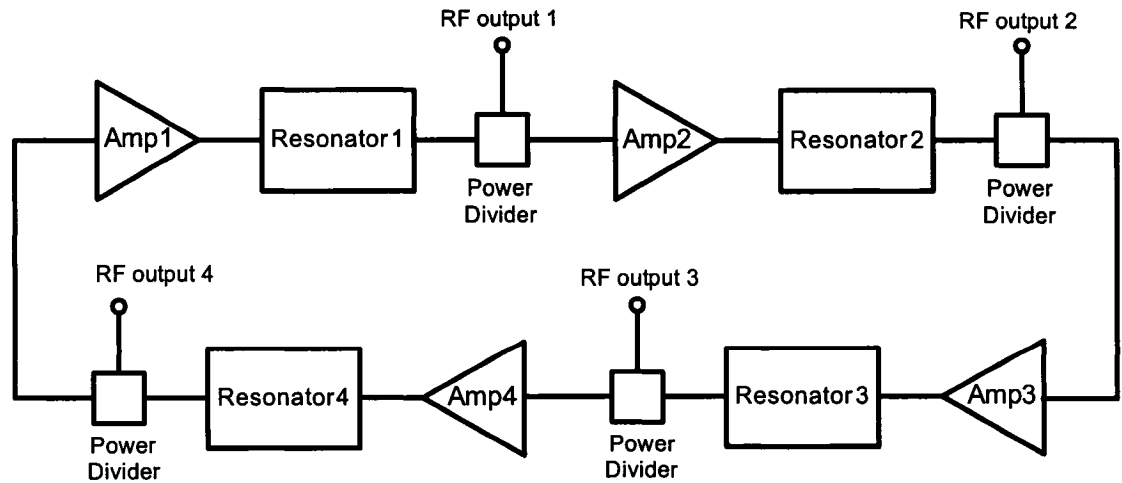
Figure 3.6: Circuit diagram of multiple series cascaded oscillator

28

Another example of series-cascaded oscillators is the quadrature LC oscillator [22]. Quadrature oscillator circuit topology is widely used for IQ generation in direct-conversion communication systems for cellular phone and wireless LAN applications. A simple quadrature LC oscillator is composed of two identical LC oscillators, as shown in Fig. 3.7(a). Two LC oscillators are coupled via coupling transistors M_{cl}, which then forces the four voltage outputs to synchronize in the quadrature.

The behavioral model of the quadrature oscillator is shown in Fig. 3.7(b) where g_m, L_p, C_p, and R_p represent an equivalent model of a single LC oscillator. Two in-phase and quadrature stages are coupled via transconductance $g_{m,couple}$. The oscillator loaded Q of the quadrature oscillator with N stages (Q_N) is thus expressed as:

$$Q_N \approx N \cdot Q_p \, sin(\phi_c) \tag{3.4}$$

where Q_p represents a loaded Q of an LC resonator, $\phi_{coupling}$ represents the phase difference between the total current and the coupling current (i_T and i_C in Fig. 3.7(b)). When ϕ_c is made equal to zero, the quadrature oscillator with N stages provides N times the group delay improvement and N noise sources, thereby resulting in 1/N phase noise improvement.

29
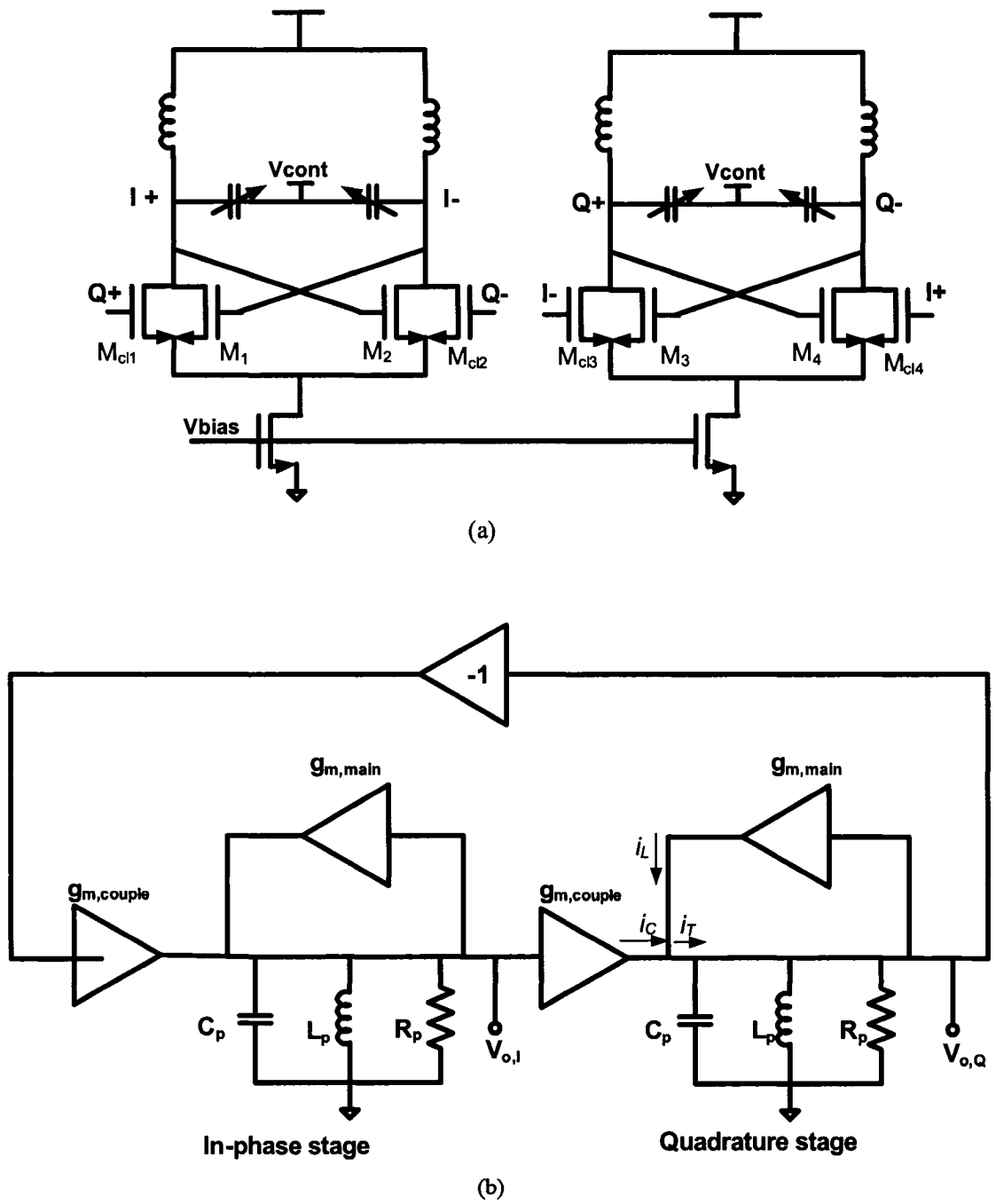
Figure 3.7: (a) Circuit schematic of a quadrature LC oscillator (b) Behavioral model of a quadrature LC oscillator

30

3.4 Multiple-Pole Filter Oscillators

To increase the oscillator group delay, a multiple-pole filter can be utilized as a frequency stabilization element in its feedback loop. An earlier study of the low phase noise oscillator using multiple-pole filters shows that group delay increases by 17 % to 60 % at the fixed insertion loss of 3 dB to 15 dB when the filter order increases from one to two [23]. Also shown is that increasing the filter order beyond two does not result in significant additional group delay increase. In this work, LC resonator-based filters shown in Fig. 3.8(b) are optimized to produce the largest group delay for a given insertion loss. The optimized filter response is similar to Butterworth or Chebyshev filters. Because this type of oscillators is a major topic of Chapter 5, it will be explained in details there.
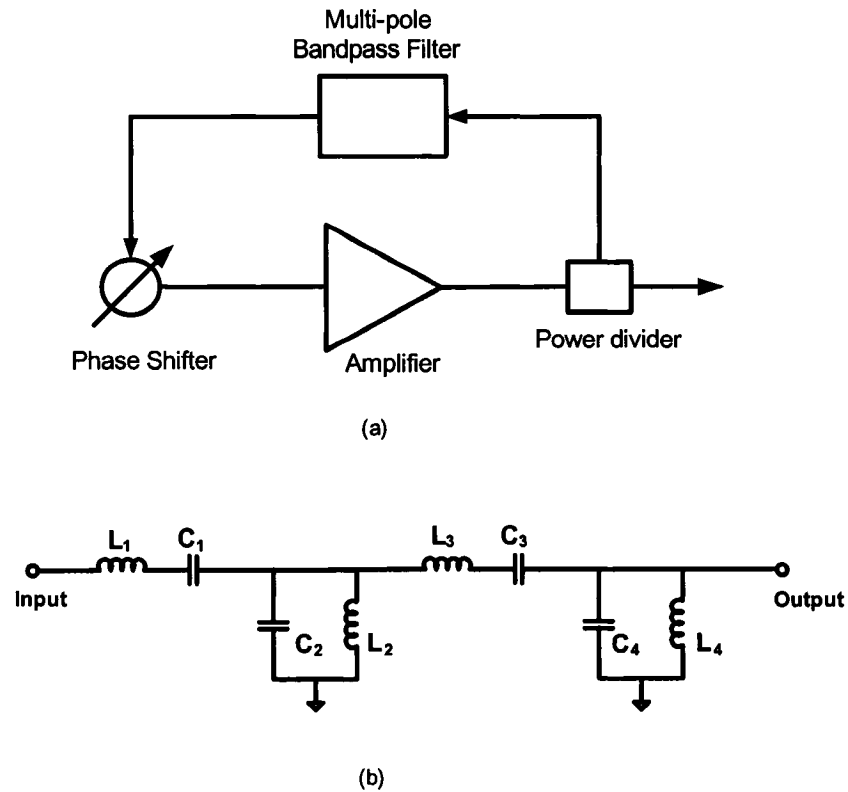
Figure 3.8: (a) Circuit diagram of a multiple-pole filter oscillator (b) LC multiple-pole bandpass filter

31

Chapter 4

Low Phase Noise Multiple-Device Oscillators Based on the Extended Resonance Technique

4.1 Introduction

As discussed in the previous chapter, the phase noise of N-device power-combining and N-coupled oscillators improves by 1/N in comparison to a single oscillator. However, the 1/N phase noise reduction is not significant enough to address the low phase-noise requirements of modern communication systems.

This chapter proposes a new low phase-noise multiple-device planar oscillator circuit based on the extended resonance technique [27]. The extended resonance technique is a power-dividing and -combining approach based on a ladder circuit structure resembling a filter. This circuit can be optimized to achieve a high group delay corresponding to a high oscillator loaded Q. Additionally, the usual 1/N phase-noise improvement can be obtained from the power-combining property of such circuits. In this manner, the extended resonance multiple-device oscillator can improve the phase noise beyond the 1/N rate relative to the number of devices employed.

In this chapter, the design of the extended resonance oscillator is discussed in Section 4.2. In Section 4.3, a power-dividing and -combining extended resonance circuit incorporating N-devices is analyzed to optimize circuit parameters for maximizing the oscillator Q, and the design approach for low phase noise is presented. In Section 4.4 and 4.5, the simulation and measurement results for C-Band HEMT and X-band SiGe HBT extended

32
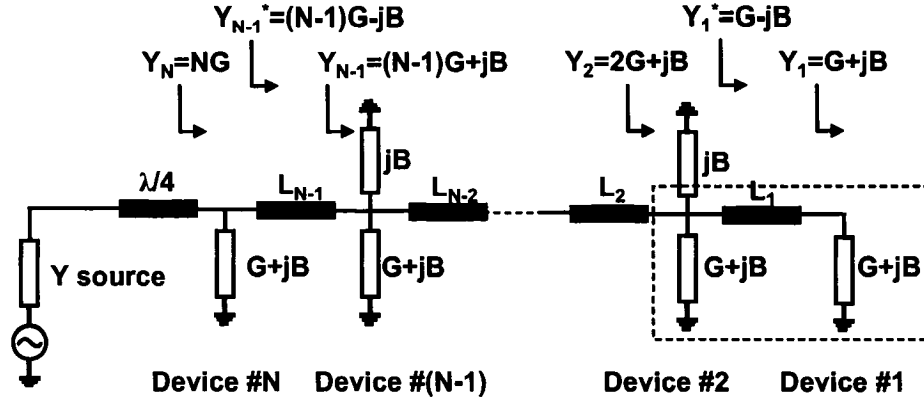
Figure 4.1: Extended resonance power dividing circuit with N two-terminal devices

resonance oscillators are presented and discussed.

4.2 Extended Resonance Oscillator Design

4.2.1 Extended Resonance Technique

To explain the theory of the extended resonance technique, we consider a circuit incorporating N two-terminal devices as shown in Fig. 4.1. The admittance of each device is assumed to be $Y = G + jB$. The length of transmission line L_1 can be chosen such that the admittance of the first device is transformed to its conjugate, namely $G - jB$. After adding a shunt element having susceptance jB at the second device, the total admittance looking into the terminals of the second device is $Y_2 = 2G + jB$. The length of the transmission line L_2 can then be chosen to convert $2G + jB$ to $2G - jB$, which cancels the susceptance of the third device. This process is repeated N times. Finally, the admittance seen at the terminals of the Nth device is NG, which is matched to the source admittance. In summary, the operation of this circuit is based on the admittance conjugate transformation at each stage. Circuit analysis of such a structure shows that the voltages at each device port are equal in amplitude and only differ in phase [27]. In this manner, the applied input power is equally divided to each device.

33
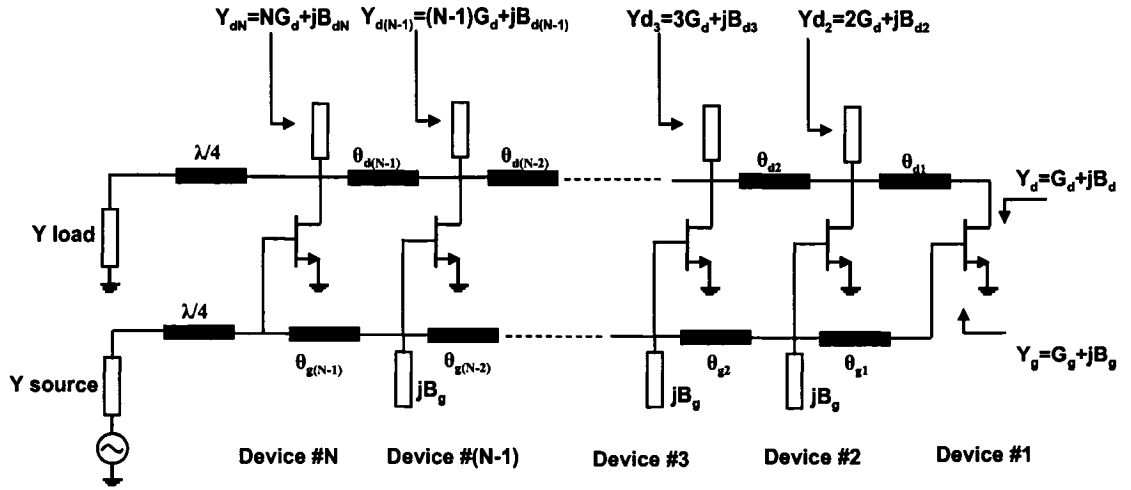
Figure 4.2: Circuit schematic of the extended resonance amplifier

4.2.2 Extended Resonance Amplifier Design

The extended resonance circuit forms an N-way power divider and combiner, which allows its application in the design of compact power-combining amplifiers. Fig. 4.2 shows a schematic of an N-device extended resonance amplifier. This technique yields compact circuits, does not require matching circuits for individual devices, and allows simple biasing of the devices. The extended resonance amplifier diagram is superficially similar to well-known distributed amplifier circuits. However, it is quite different in operation [27]. The extended resonance amplifier is a power-combining circuit where all the devices are uniformly excited, thus contributing equally to the output power. This type of circuit is generally a narrow-band resonant structure, while a distributed amplifier is a broadband circuit. Finally, there are no input and output terminations in the extended resonance circuit.

In the design of extended resonance amplifiers, the input power-dividing and output power-combining circuits should be consistently designed to achieve coherent power combining. Through large-signal simulations, the admittance looking into the gate of each device is determined at $Y_g = G_g + jB_g$, while the admittance looking into the drain of each device is $Y_d = G_d + jB_d$. Based on the device gate admittance, the input power dividing circuit design follows the extended resonance procedure, starting at the the first device and

34

ending at the Nth device. At the kth stage between two adjacent gates $k+1$ and k, the electrical length of the interconnection transmission line θ_{gk} is determined by:

$$\theta_{gk} = arctan\left(\frac{2B_g Y_0}{(kG_g)^2 + B_g^2 - Y_0^2}\right) \tag{4.1}$$

and the phase delay is represented by:

$$\phi_{gk} = arctan\left(\frac{2kG_g B_g}{(kG_g)^2 - B_g^2 - Y_0^2}\right) = -arctan\left(\frac{kG_g\, tan\theta_{gk}}{Y_0 - B_g tan\theta_{gk}}\right) \tag{4.2}$$

The phase delay between two adjacent drains k and $k+1$ is represented by:

$$\phi_{dk} = arctan\left(\frac{2kG_d B_{dk}}{(kG_d)^2 - B_{dk}^2 - Y_0^2}\right) = -arctan\left(\frac{kG_d\, tan\theta_{dk}}{Y_0 - B_{dk} tan\theta_{dk}}\right) \tag{4.3}$$

To achieve coherent power combination, the voltage phase delay between successive device output ports (ϕ_{dn}) should be equal in magnitude but opposite in sign to the voltage phase delay between the corresponding device input ports (ϕ_{gn}). Because G_g, G_d, and B_g are obtained from the large signal simulations, the drain susceptance at the kth stage B_{dk} is determined as:

$$B_{dk} = \frac{Y_0}{tan\theta_{dk}} + \frac{G_d\,(Y_0 - B_g\, tan\theta_{gk})}{G_g \cdot tan\theta_{gk}} \tag{4.4}$$

To obtain the required drain susceptances, appropriate reactive elements can be inserted at each drain port, as shown in Fig. 4.2.

4.2.3   Synthesis of Embedding Feedback Circuit

An extended resonance oscillator is constructed by employing a feedback around the extended resonance amplifier, as shown in Fig. 4.3. The circuit is designed based on the large-signal operation of the amplifier according to the substitution theory [30],[31]. The voltages and currents at the input and output terminals of the amplifier can be determined

35
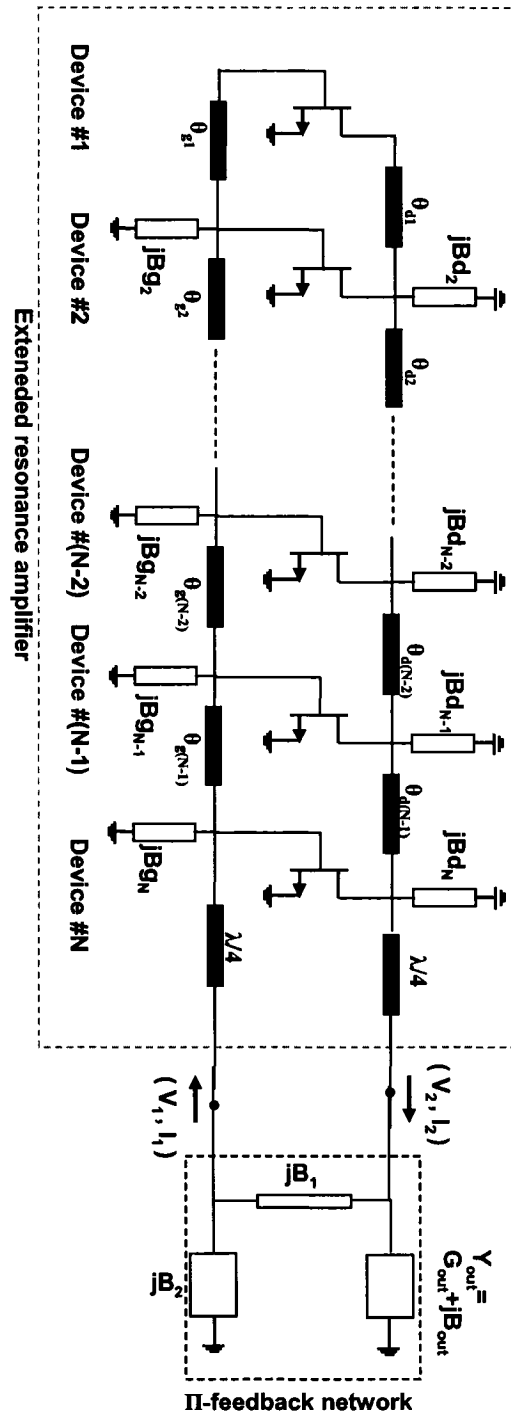
Figure 4.3: Circuit schematic of the extended resonance oscillator

at a specific RF input power level through circuit simulation. The feedback circuit that provides the same large-signal condition as the amplifier can then be designed by determining

36

the terminal voltages and currents. Here, a parallel Π-shaped feedback network consisting of one conductive element (G_{out}) and three susceptive elements (jB_{out}, jB_1, jB_2) is employed as the external feedback network. The susceptive elements and the output load in the Π-feedback network are calculated based on the input and output terminal voltages and currents [30].

$$Y_{out} = G_{out} + jB_{out} \tag{4.5}$$

$$G_{out} = (Y_1 + A_r Y_3 + A_i Y_4)/|A|^2 \tag{4.6}$$

$$B_{out} = \left[\frac{Y_1(A_r - |A|^2)}{A_i} - A_i Y_3 + A_r Y_4 \right]/|A|^2 \tag{4.7}$$

$$B_1 = Y_1/A_i \tag{4.8}$$

$$B_2 = Y_1(A_r - 1)/A_i + Y_2 \tag{4.9}$$

where

$$A = A_r + jA_i = V_2/V_1 \tag{4.10}$$

$$Y_1 = -Re(I_1/V_1) \tag{4.11}$$

$$Y_2 = -Im(I_1/V_1) \tag{4.12}$$

$$Y_3 = Re(I_2/V_1) \tag{4.13}$$

$$Y_4 = Im(I_2/V_1) \tag{4.14}$$

V_1 and I_1 are the input terminal voltage and current, and V_2 and I_2 are the output terminal voltage and current in the amplifier.

4.3 Extended Resonance Design for Low Phase Noise

The main design objective for the extended resonance oscillator is to minimize its phase noise while maximizing output power through power combining of multiple devices. In the extended resonance oscillator, low phase noise can be achieved through increasing the group delay and power combining.

It is well known that an important mechanism for lowering phase noise in an oscillator is through increasing the oscillator loaded Q. The oscillator loaded Q is defined in Chapter 2 by:

$$Q_{osc} = \frac{\omega_0}{2} \cdot \left| \frac{d\phi(\omega)}{d\omega} \right| \tag{4.15}$$

where $\phi(\omega)$ is the phase of the oscillator open-loop transfer function at a steady state. It must be noted that the oscillator loaded Q is proportional to the absolute value of the group delay in (4.15) [7]. In other words, the increase in the group delay leads to the increase in the frequency selectivity of the oscillator circuit, thus reducing the phase noise.

The extended resonance circuit is a ladder network, composed of multiple devices and their interconnecting transmission lines, that behaves like a filter. This can be explained by considering an extended resonance circuit incorporating N devices as shown in Fig. 4.1. At the nth stage, the admittance looking into the nth device $(nG + jB)$ is transformed to its conjugate admittance $(nG - jB)$, resonating out the susceptance of the next device. Therefore, multiple resonant circuits are cascaded in the extended resonant circuit, allowing the circuit to achieve high group delays.

In order to investigate how to achieve large group delay, an extended resonance power-dividing and -combining circuit incorporating N devices is analyzed. To simplify the task, a two-device extended resonance circuit is first analyzed. Subsequently, this analysis is extended to N devices. The two-device circuit shown in Fig. 4.4(a) is one possible circuit configuration among many possible extended resonance circuits [27], where G_m is

38

the large-signal transconductance of each device. The large-signal device input and output admittances are denoted by $G_{in} + jB_{in}$ and $G_{out} + jB_{out}$, respectively. $G_{in} + jB_{in}$ and $G_{out} + jB_{out}$ are transformed to $G_i + jB_i$ and $G_o + jB_o$ through transmission lines (T_1 and T_4) and open stubs (T_2 and T_3) respectively, as shown in Fig. 4.4(a). An equivalent circuit for a unit cell of this structure is shown in Fig. 4.4(b), where the transconductance G'_m incorporates the effect of the gate and drain transmission lines and open stubs (T_1 - T_4). An expression for the group delay in the extended resonance circuit can be found in terms of the device and circuit parameters. If G_i, G_o and B_i are given, B_o is chosen such that the phase difference between V_{o2} and V_{o1} is equal to the phase difference between V_{i2} and V_{i1} for coherent power combination. To simplify the analysis, G_{in} and G_{out} are transformed to an equal value G_i. The steady-state voltages at each device's input and output ports are determined when an input current source (I_i) is applied. Referring to the input dividing circuit in Fig. 4.4(a), Γ_{i1}, Γ_{i2}, and Γ_{iM} can be expressed as:

$$\Gamma_{i1} = \frac{(Y_0 - G_i - jB_i)}{(Y_0 + G_i + jB_i)} \tag{4.16}$$

$$\Gamma_{i2} = \frac{(Y_0 - 3G_i - jB_i)}{(Y_0 + 3G_i + jB_i)} \tag{4.17}$$

$$\Gamma_{iM} = \frac{(Y_0 - Y_{iM} - jB_{si})}{(Y_0 + Y_{iM} + jB_{si})} \tag{4.18}$$

where Y_0 is the characteristic admittance of the interconnecting transmission lines, and:

$$Y_{iM} = Y_0 \frac{G_i + jB_i + Y_0 tanh(\gamma l)}{Y_0 + (G_i + jB_i) tanh(\gamma l)} \tag{4.19}$$

where γ is the complex propagation constant and l is the physical length of the interconnecting transmission line.

Using the above reflection coefficients, the voltages V_{i1} and V_{i2} at the input terminals of

39
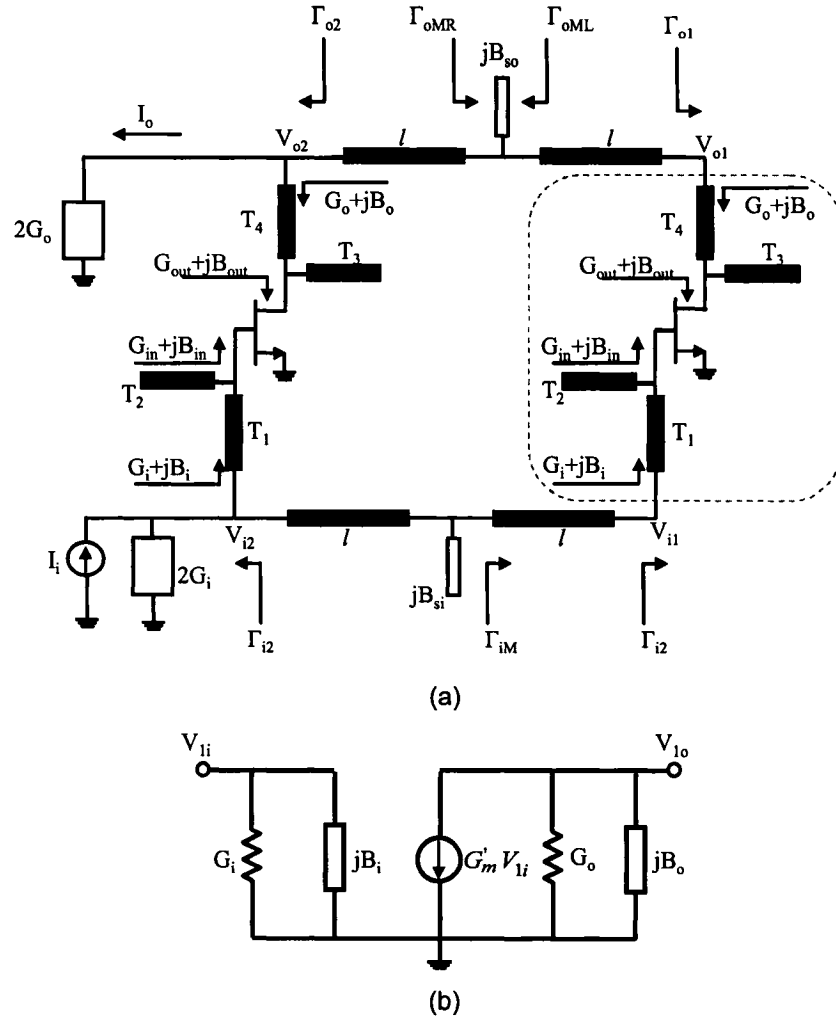
Figure 4.4: (a) Two-device extended resonance circuit (b) Equivalent circuit for the expanded device part marked by a dashed line box in Fig. 4.4(a)

the first and second devices can be written as:

$$V_{i1} = \frac{I_i(1+\Gamma_{i1})(1+\Gamma_{i2})(1+\Gamma_{iM})e^{-\gamma l}}{2Y_0(1-\Gamma_{i2}\Gamma_{iM}e^{-\gamma l})(e^{\gamma l}+\Gamma_{i1}e^{-\gamma l})} \tag{4.20}$$

$$V_{i2} = \frac{I_i(1+\Gamma_{i2})(1+\Gamma_{iM}e^{-2\gamma l})}{2Y_0(1-\Gamma_{i2}\Gamma_{iM}e^{-\gamma l})} \tag{4.21}$$

For the output combining circuit in Fig. 4.4(a), the voltages V_{1o} and V_{2o} at the output

40

terminals of the first and second devices can be determined as:

$$V_{1o} = -\frac{G'_m V_{i1}(1+\Gamma_{o1})(1+\Gamma_{oML}e^{-2\gamma l})}{2Y_0(1-\Gamma_{o1}\Gamma_{oML}e^{-2\gamma l})} - \frac{G'_m V_{i2}(1+\Gamma_{o2})(1+\Gamma_{oMR})(1+\Gamma_{o1})e^{-\gamma l}}{2Y_0(1-\Gamma_{o2}\Gamma_{oMR}e^{-2\gamma l})(e^{\gamma l}+\Gamma_{o1}e^{-\gamma l})}$$

(4.22)

$$V_{o2} = -\frac{G'_m V_{i2}(1+\Gamma_{o2})(1+\Gamma_{oMR}e^{-2\gamma l})}{2Y_0(1-\Gamma_{o2}\Gamma_{oMR}e^{-2\gamma l})} - \frac{G'_m V_{i1}(1+\Gamma_{o1})(1+\Gamma_{oML})(1+\Gamma_{o2})e^{-\gamma l}}{2Y_0(1-\Gamma_{o1}\Gamma_{oML}e^{-2\gamma l})(e^{\gamma l}+\Gamma_{o2}e^{-\gamma l})}$$

(4.23)

This analysis can be expanded to an N-device extended resonance circuit using a similar approach. A Matlab code was written to investigate the effect of the circuit parameters on the group delay. The group delay of the N-device extended resonance circuit can be expressed as:

$$\left.\frac{d\phi(\omega)}{d\omega}\right|_{\omega=\omega_0} = \frac{\phi(\omega_0+\Delta\omega) - \phi(\omega_0-\Delta\omega)}{2\Delta\omega}$$

(4.24)

where

$$\phi(\omega) = \angle\left(\frac{I_o(\omega)}{I_i(\omega)}\right) = \angle\left(\frac{V_{oN}(\omega)}{I_i(\omega)}\right),$$

(4.25)

I_i and I_o are the input and output currents and V_{oN} is the voltage at the output terminal of the Nth device. In the numerical analysis, the center frequency f_0 and the frequency deviation Δf are assumed to be 10 GHz and 10 MHz, respectively. To account for the losses, the parameters for Rogers TMM3 substrate are used ($\varepsilon_r = 3.27$, $H=15$mil, $tan\delta = 0.002$).

Based on the numerical analysis, the effect of the device admittance on the group delay and insertion loss is examined for the four-device extended resonance circuit. Fig. 4.5(a) and (b) show the plot of group delay and insertion loss versus the values of G_i and B_i. It is observed that the group delay and insertion loss are proportional to the absolute value of device susceptance B_i. Using the phase noise figure of merit (PNFOM) defined in (2.12),

41
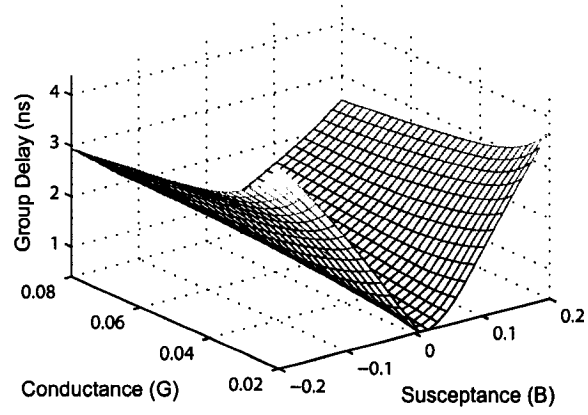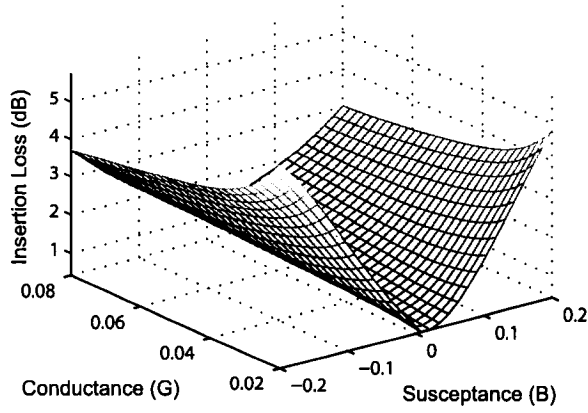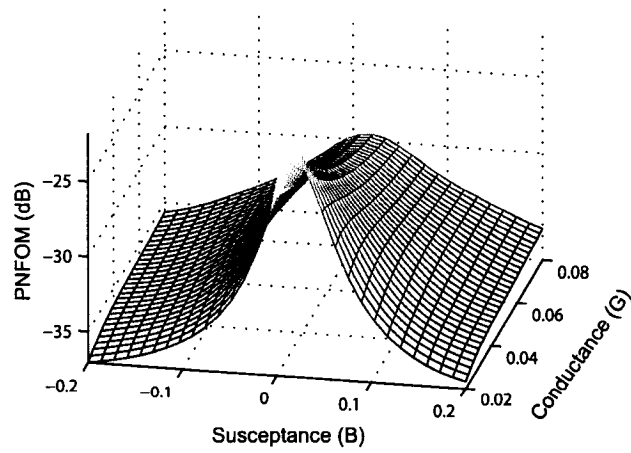
Figure 4.5: (a) Group delay, (b) insertion loss, and (c) PNFOM versus the device conductance and susceptance in the four-device extended resonance circuits

42
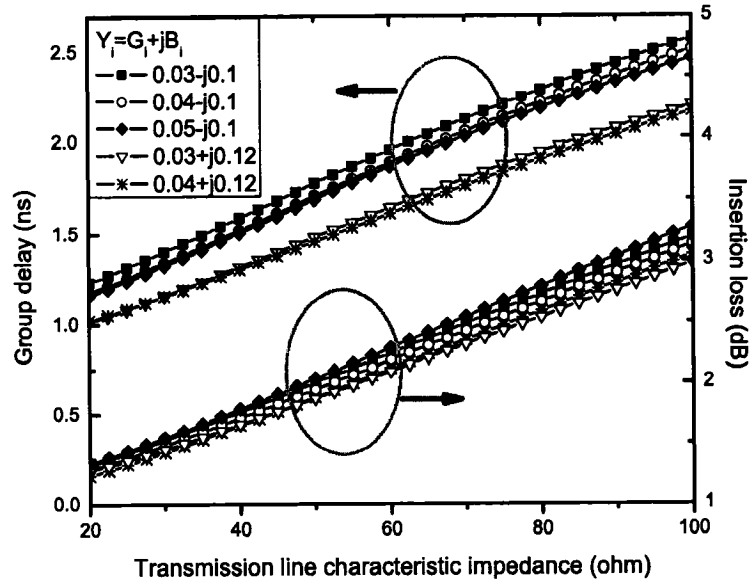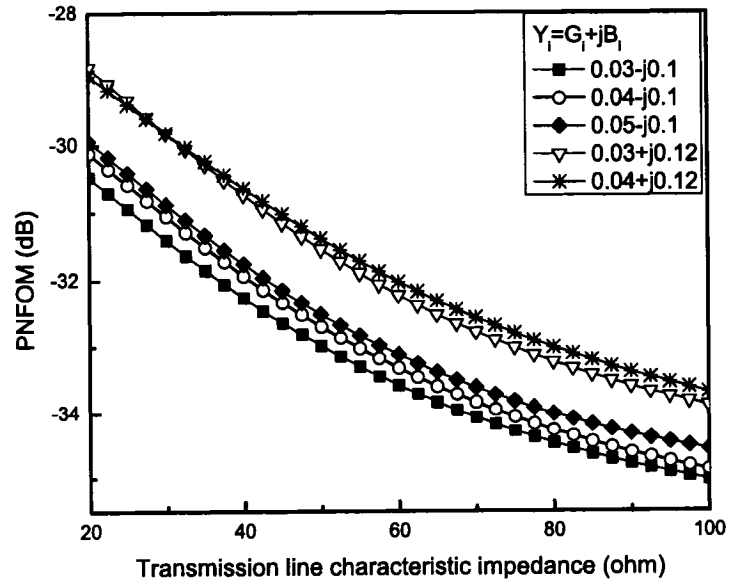
Figure 4.6: Effect of the characteristic impedance of the interconnecting transmission line on (a) group delay, insertion loss, and (b) PNFOM for the four-device extended resonance circuit with various device admittances.

43

the plot of PNFOM versus the device admittances is shown in Fig. 4.5(c). Since PNFOM is proportional to phase noise, a lower PNFOM indicates a lower phase noise. Fig. 4.5(c) indicates that large device susceptance B_i is advantageous for low phase noise.

Next to be considered is the effect of the characteristic impedance of the interconnecting transmission lines on the group delay and insertion loss. In Fig. 4.6(a) and (b), the plot of group delay, insertion loss, and PNFOM versus the characteristic impedance of the interconnecting transmission lines is given in four-device extended resonance circuits. The simulation result shows that phase noise is inversely proportional to the characteristic impedance of the interconnecting transmission lines.

Fig. 4.7 shows the circuit schematic of the extended resonance oscillator designed for low phase noise performance. Based on the above discussions, the low-phase noise design approaches for this oscillator are outlined as follows.

1. By using admittance transforming circuits (AT_i and AT_o in Fig. 4.7), the input and output device admittance values are transformed to new admittance values with the highest achievable susceptance.

2. The highest achievable characteristic impedance value is chosen for the interconnecting transmission lines.

3. The shunt susceptive stubs inserted halfway between the devices (jB_{on} and jB_{in} in Fig. 4.7) are selected in order to increase the group delay. Further, the susceptive stubs can reduce the overall circuit size.

In general, as the number of devices increases, more interconnecting stages with the resonance characteristics are cascaded, thereby increasing the overall oscillator Q. However, at the same time the circuit insertion loss also increases with the number of devices, thus impeding the phase noise improvement rate. Fig. 4.8 shows the group delay and insertion loss of the extended resonance circuit with the number of devices. Furthermore, the estimated phase noise improvement (PNI) of the N-device extended resonance oscillator

44
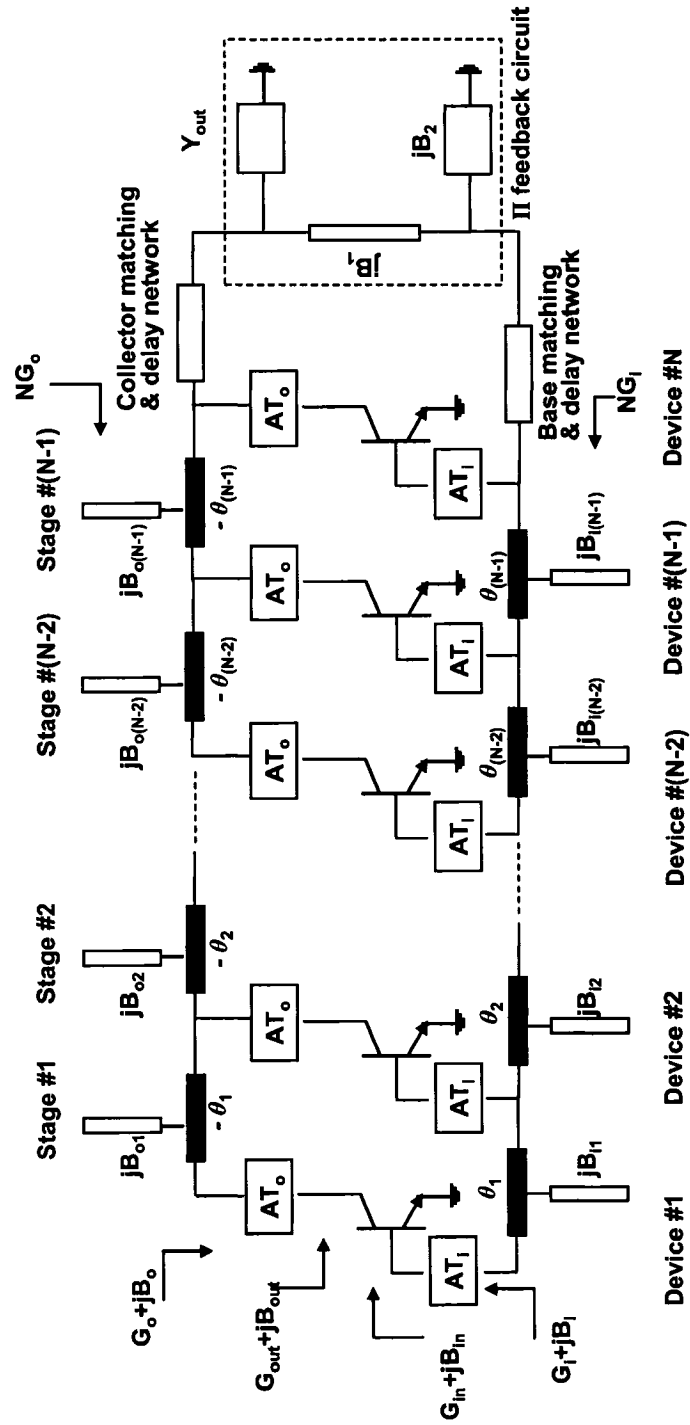
Figure 4.7: Circuit schematic of the extended resonance oscillator designed for the low phase-noise performance. AT_i and AT_o represent the input and output admittance transforming networks, respectively. The admittance transforming networks transform the input and output device admittances $G_{in} + jB_{in}$ and $G_{out} + jB_{out}$ into the new admittances $G_i + jB_i$ and $G_o + jB_o$, respectivley.

45

compared to the 2-device extended resonance oscillator is calculated using the following equation and shown in Fig. 4.8.

$$
\begin{aligned}
PNI(dB) \;=\;& 10\log\left(\frac{GD_N}{GD_2}\right)^2 - (IL_N - IL_2) \\
&+\; 10\log(N/2) \tag{4.26}
\end{aligned}
$$

where GD_N and IL_N represent the group delay (ns) and the insertion loss (dB) of the N-device extended resonance circuit, respectively. The above equation incorporates the effects of group delay, insertion loss, and power combining on phase noise. Fig. 4.8 shows that the four-device and eight-device oscillator are expected to achieve approximately 7.5 dB and 13 dB phase noise improvements over the two-device oscillator, respectively.
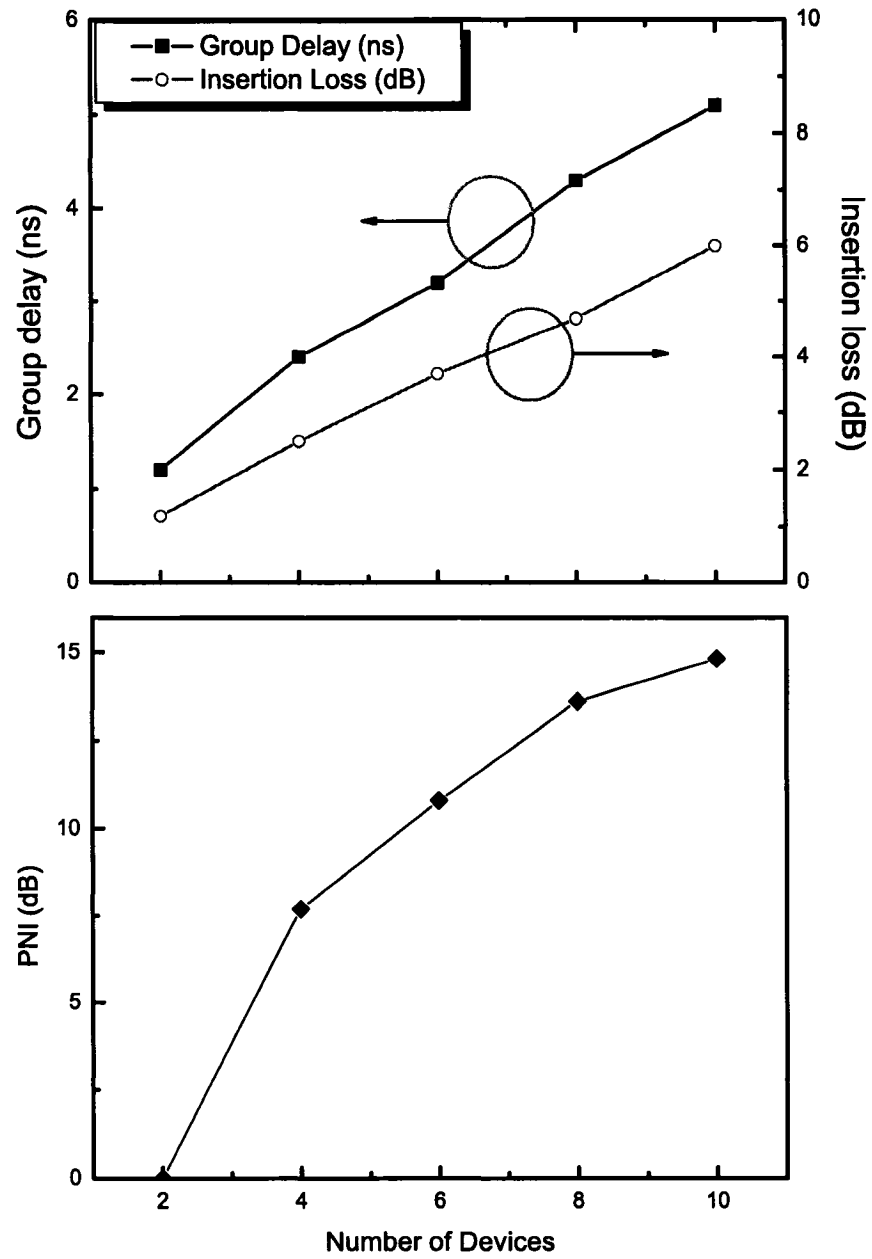
Figure 4.8: Group delay and insertion loss with the number of devices for TMM3 substrate.

4.4 C-Band HEMT Extended Resonance Oscillators

4.4.1 Circuit Design

To demonstrate the operation of the aforementioned design technique, a single-device oscillator and a two-device and a four- device extended resonance oscillators are designed and fabricated at 6 GHz. It should be mentioned that the HEMT extended resonance oscillators are designed based on group delay analysis of only power-dividing extended resonance circuits [26]. The transistors employed in this design are the packaged pHEMT devices (NE32584C). The devices are biased with 2 V on the drain and -0.4 V on the gate. Fig. 4.9(a)-(c) show the photographs of the fabricated oscillators. Through the large signal simulation, the gate and drain admittances are determined. Based on the substitution theory, a single-device oscillator was designed using the determined gate and drain admittance. Open stubs are connected to the source ports and a shorted stub is connected to the gate port in order to provide series-feedback operation, as shown in Fig. 4.9(a). For the design of the two-device and four-device extended resonance oscillators, these device admittance values are transformed to new admittance values. Also, the admittance converting network at each stage is optimized to satisfy the conditions for the extended resonance operation.

4.4.2 Experimental Results

The three HEMT oscillators are fabricated on Rogers TMM3 substrates with a dielectric constant of 3.27 and a thickness of 15 mils. Table 4.1 shows the measured output power and oscillation frequency. It is shown that the output power increases with the number of devices as a result of power combining.

48
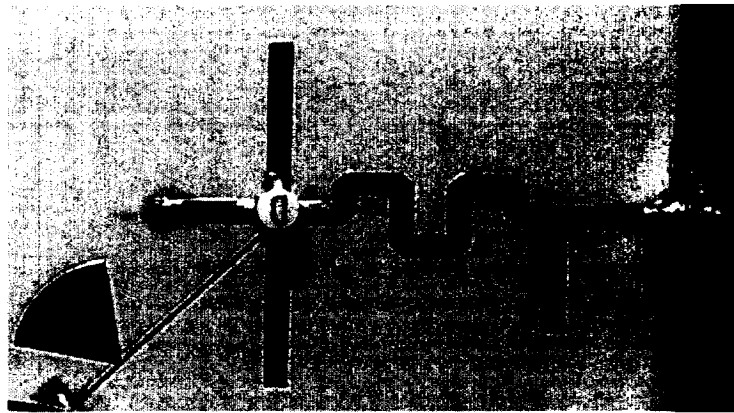
(a)
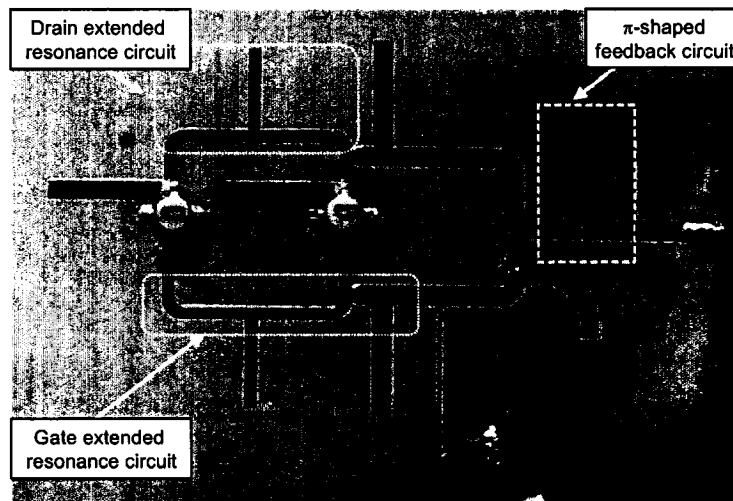
(b)
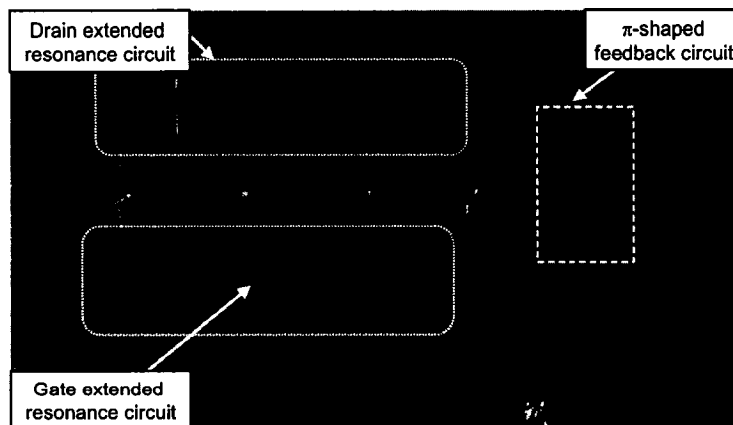
(c)

Figure 4.9: Photograph of the fabricated HEMT oscillators (a) the single-device oscillator (b) the two-device extended resonance oscillator (c) the four-device extended resonance oscillator

49
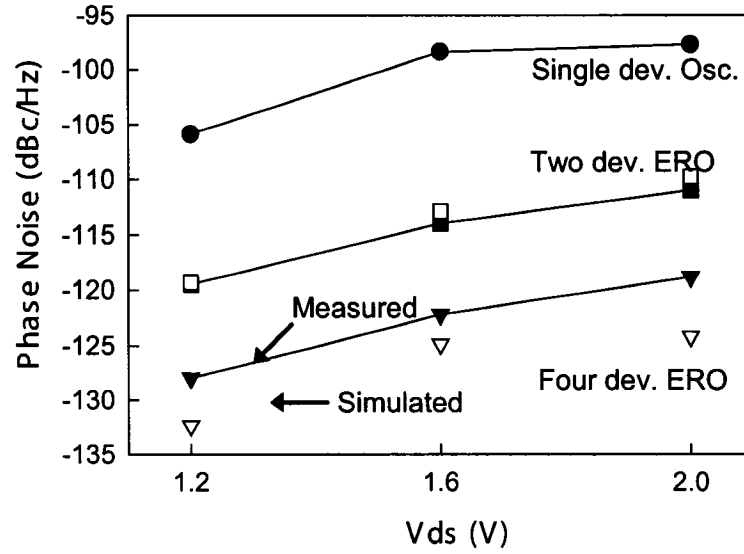
Figure 4.10: Measured phase noise comparison for the three designed HEMT oscillators at 1 MHz offset frequency (Vgs=-0.4V). The dotted lines indicate the expected phase noise improvements of the two-device and four-device extended resonance oscillators over the single device oscillator based on the simulation.

Table 4.1: The measured output power and frequency for three HEMT oscillators

	F_o (GHz)	P_o (dBm)
1-device oscillator	6.02	7.2
2-device oscillator	5.9	9.7
4-device oscillator	5.93	12.5

50
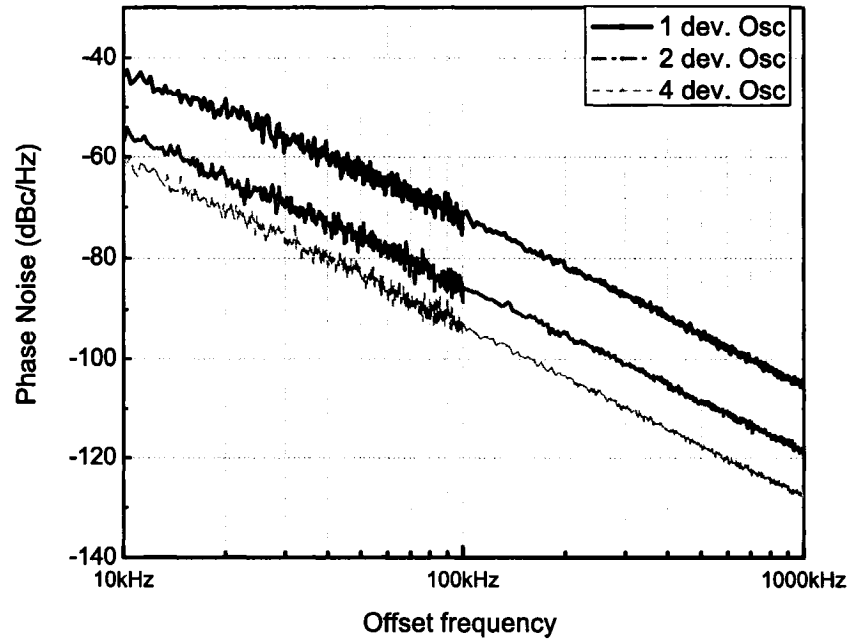
Figure 4.11: Phase noise measurement result for the single-device, two-device, and four-device oscillators

The phase noise of the three HEMT oscillators is measured based on the FM discriminator technique using Agilent E5504A phase noise measurement system. The phase noise measurement results are shown in Fig. 4.11. The two-device and four-device extended resonance oscillators show approximately 13 dB and 22 dB reduction of phase noise over the single-device oscillator, respectively. The measured phase noise of the four-device extended resonance oscillator at $V_{ds} = 1.2V$, $V_{gs} = -0.4V$ is -128 dBc at 1 MHz offset frequency. From the ADS simulation, the estimated phase noise improvements of the two-device and four-device extended resonance oscillators over the single-device oscillator are 13 dB and 26.6 dB, respectively, as shown in Fig. 4.11. The measured phase noise of the two-device extended resonance oscillator shows a good agreement with the simulation results, while there is a 4.6 dB discrepancy for the four-device extended resonance oscillator. This discrepancy can be attributed to the fabrication error and the imprecision of the feedback network.

51

4.5 X-Band Four-Device SiGe HBT Oscillator

4.5.1 Circuit Design

An X-band four-device extended resonance oscillator is designed employing the design methodologies described in Section 4.3. To further reduce the phase noise, packaged SiGe HBT devices (NEC NESG2031M05) with low 1/f noise are used in the extended resonance oscillator design. The oscillator is designed at 9 GHz and constructed on a Rogers TMM3 substrate. Fig. 4.12 shows the circuit layout and photograph of the four-device SiGe HBT extended resonance oscillator. Each device is biased at a collector-emitter voltage (V_{ce}) of 2 V with a collector current of 8 mA. The device input and output admittances are determined through large-signal simulations and transformed to input and output device admittances of 0.04 - j 0.1 and 0.04 + j 0.13. The characteristic impedance of 80 Ω is chosen for the inter-connecting transmission lines. The above device admittance and characteristic impedance are selected by taking into account the tolerance to fabrication error. The simulation results show that the oscillator Q of 90 is achieved in contrast to the oscillator Q of 55 for the pHEMT four-device extended oscillator. In the circuit simulation, a parasitic oscillation around 1 GHz was observed. To eliminate low frequency parasitic oscillations, a coupled line with an insertion loss of 0.2 dB is inserted in the feedback network. The use of the coupled line suppressed 1 GHz parasitic oscillation without affecting the output power level.

4.5.2 Experimental Results

The four-device SiGe HBT oscillator yields an output power of 9.7 dBm at 9.1 GHz. The total consumed dc power is 66 mW, which corresponds to a dc-rf efficiency of 14%. The oscillator phase noise is measured based on FM discriminator technique with an Agilent E5504A phase noise measurement system. The phase noise measurement results are shown in Fig. 4.13. The measured phase noise is -119 dBc/Hz and -138 dBc/Hz at 100

3.7 cm

Collector combining circuit

Π–feedback network

Output

2.3 cm

E C
B E

Coupled line

Base dividing circuit

(a)

(b)
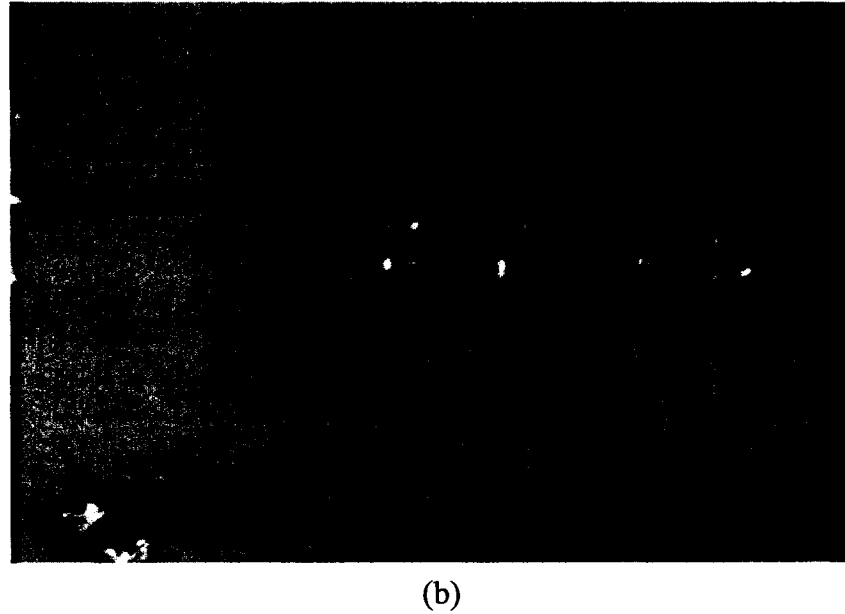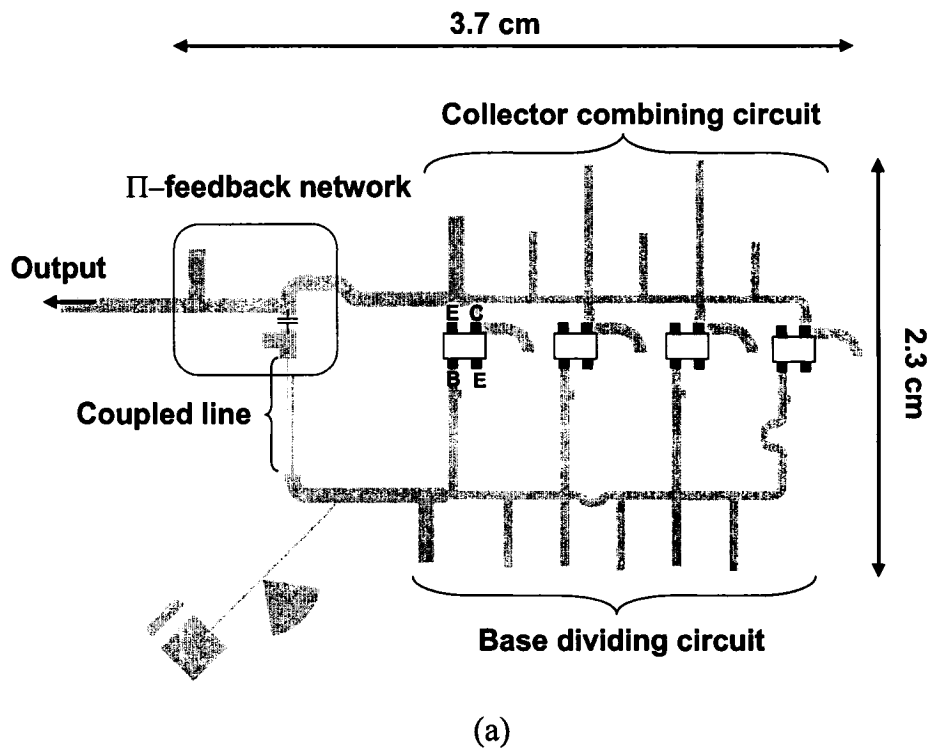
Figure 4.12: Circuit layout of the SiGe HBT X-band four-device extended resonance oscillator

53
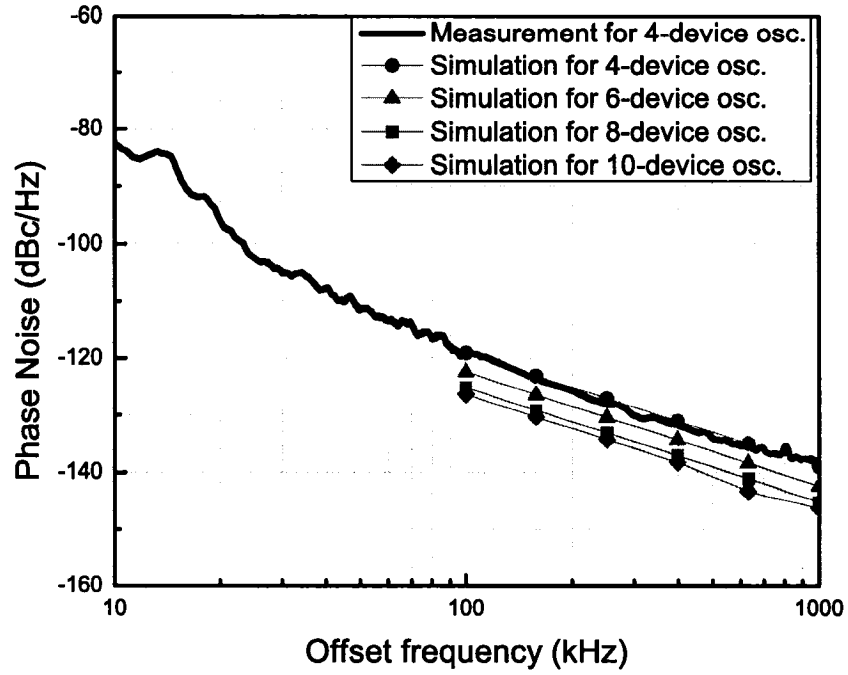
Figure 4.13: Phase-noise measurement and simulation result for the SiGe HBT X-band extended resonance oscillators. The black line shows the measured phase noise for the four-device extended resonance oscillator. The gray lines show the simulated phase noises for the four, six, eight, and ten-device extended resonance oscillators.

kHz and 1 MHz offset frequency, respectively. Since the transistor model does not include $1/f$ noise data, the phase noise is simulated only in $1/f^2$ region using Agilent ADS^{TM} simulator. The measured phase noise shows a good agreement with the simulations in the $1/f^2$ region, as shown in Fig. 4.13. This oscillator is evaluated in terms of the commonly used figure of merit (FOM) [32], defined as:

$$FOM = L(f_m) + 20\log\left(\frac{f_m}{f_o}\right) + 10\log(P_{dc}) \qquad (4.27)$$

where $L(f_m)$ is the phase noise at the offset frequency, f_m, f_o is the oscillation frequency, and P_{dc} is the dc power consumption (mW). The FOM of the four-device extended resonance oscillator is calculated as -200 dBc/Hz. The comparison with other published microwave oscillators is given in Chapter 5.

The simulated phase noise for a six-device, an eight-device, and a ten-device extended

54

resonance oscillator is also shown in Fig. 4.13. The predicted phase noise improvement for six-, eight-, and ten-device oscillators are 4.4 dB, 7.1 dB, 8.3 dB compared to the four-device oscillators, respectively

4.6 Conclusion

This chapter presented a new multiple-device extended resonance oscillator capable of improving the phase noise beyond the 1/N rate relative to the number of devices employed. A complete analysis of N-device extended resonance circuits was given to achieve low phase-noise performance. The analysis showed that the oscillator loaded Q was increased by transforming original large-signal device admittances to optimal values and choosing a large characteristic impedance value for interconnecting transmission lines.

The three 6 GHz HEMT oscillators and the 9.1 GHz four-device SiGe HBT oscillator were demonstrated herein. The SiGe HBT four-device oscillator showed an excellent phase noise of -119 dBc/Hz and -138 dBc/Hz at 100 kHz and 1 MHz offset frequencies, respectively. The proposed technique is expected to provide lower phase noise by incorporating more devices. The goal for this project is to design a monolithic low phase-noise extended resonance oscillator at millimeter-wave frequencies.

Chapter 5

Low Phase-Noise Oscillators Employing Elliptic-Response Bandpass Filters

5.1 Introduction

Dielectric resonators are widely employed in current low phase-noise microwave oscillators because they provide very high unloaded quality factors on the order of a few thousand. However, the dielectric resonators are bulky and not planar. Many different types of planar-type microwave oscillators have been investigated to address these issues. Most of these works have focused on designing high-Q planar-type single resonators including active resonator [33], split ring resonator [34], spiral resonator [35], hair-pin resonator [41], and ring resonator [43]. These resonators are usually placed at the gate or base terminals of active devices as frequency stabilization elements in a series-feedback configuration.

This chapter proposes a phase noise reduction approach by employing a multiple-pole microstrip elliptic-response bandpass filter as a frequency stabilization element within the feedback loop of microwave oscillators. Filters consisting of multiple resonators can significantly enhance the oscillator Q as compared to single resonators, because group delay increases by adding more resonators. The first demonstration of low phase-noise oscillator design using multiple-pole bandpass filters is presented in [14] where multiple-pole filters are optimized using LC resonators, resulting in conventional Butterworth or Chevyshev filter response. In this work, elliptic-response bandpass filters are proposed for the design of low phase-noise oscillators for the first time. Elliptic filters generate large group-delay

56

peaks at their passband edges due to the transmission zeros resulting from cross coupling of resonators. By taking advantage of the large group-delay peaks, the elliptic filter is capable of providing high oscillator loaded Q. Generally the frequency-dependent group-delay characteristic of the elliptic filter is considered to be problematic due to the distortions it causes in many communications systems [36]. However, in this work, this group-delay response is employed to advantage for the design of low phase noise oscillators.

The organization of this chapter is as follows. Section 5.2 discusses the group-delay characteristics of elliptic-response filters and then presents the filter optimization for the application of low phase-noise oscillators. Section 5.3 describes the design approaches for a four-pole elliptic bandpass filter and a microwave oscillator employing the filter. Finally, Section 5.4 presents and discusses the simulation and measurement results for a 9 GHz SiGe HBT oscillator employing the four-pole elliptic filter.

5.2 Theory

5.2.1 Group-Delay Characteristics of Elliptic Filters

Generally, a transfer function of a lossless passive filter is represented by:

$$|S_{21}(\Omega)|^2 = \frac{1}{1 + \varepsilon^2 F_n^2(\Omega)} \tag{5.1}$$

where ε is a ripple constant related to a given return loss $L_R = 20 \, log|S_{11}|$ in dB, Ω is a frequency variable that is normalized to the passband cut-off frequency of the lowpass prototype filter, and $F_n(\Omega)$ represents a characteristic function that determines the filter response such as Butterworth, Chebyshev, and elliptic.

The characteristic function of filters can be expressed as a rational function having poles and zeroes. The characteristic function of elliptic filters has the same number of poles and zeroes, while that of Butterworth and Chebysheve filters has only poles but no zero. Due to

57

the existence of zeros, elliptic filters are capable of providing sharper filter skirt and higher selectivity than Butterworth and Chebyshev filters.

Fig. 5.1 shows the comparison of S_{21} and group-delay responses of Butterworth, Chevyshev, and elliptic four-pole bandpass filters. These three filters have the same center frequency of 9 GHz, unloaded resonator Q of 200, and bandwidth of 300 MHz. Two transmission zeros close to the passband in the elliptic filter are clearly shown in Fig. 5.1(a), and large group-delay peaks at the edges of the passband are shown in Fig. 5.1(b). This is because the transmission zeros located close to the passband in the elliptic filter contribute to increasing the group delay at the passband edges. By designing an oscillator to perform at the frequency close to the passband edges marked by the dotted-line circles in Fig. 5.1(b), a low phase-noise performance can be achieved. It is worthwhile to mention that although the S_{21} of the filter does not have any sharp resonant peaks, it can generate a high oscillator loaded Q, because the oscillator loaded Q is dependent on the loop group delay as shown in (2.11).

5.2.2 Filter Design and Optimization

In microwave circuits, the elliptic-response filter is mainly realized with a selective quasi-elliptic function having only one pair of transmission zeros, which provides an intermediate response between elliptic and Chevyshev filters. The characteristic function of the quasi-elliptic filter is represented by:

$$F_n(\Omega) = cosh\left[(n-2)cosh^{-1}(\Omega) + cosh^{-1}\left(\frac{\Omega_t\Omega - 1}{\Omega_t - \Omega}\right) + cosh^{-1}\left(\frac{\Omega_t\Omega + 1}{\Omega_t + \Omega}\right)\right] \quad (5.2)$$

where $\pm\Omega_t$ are the frequency locations of a pair of transmission zeros, and n is the degree of the filter.

Fig. 5.2 shows the coupling structure of a four-pole quasi-elliptic filter where the dots

58
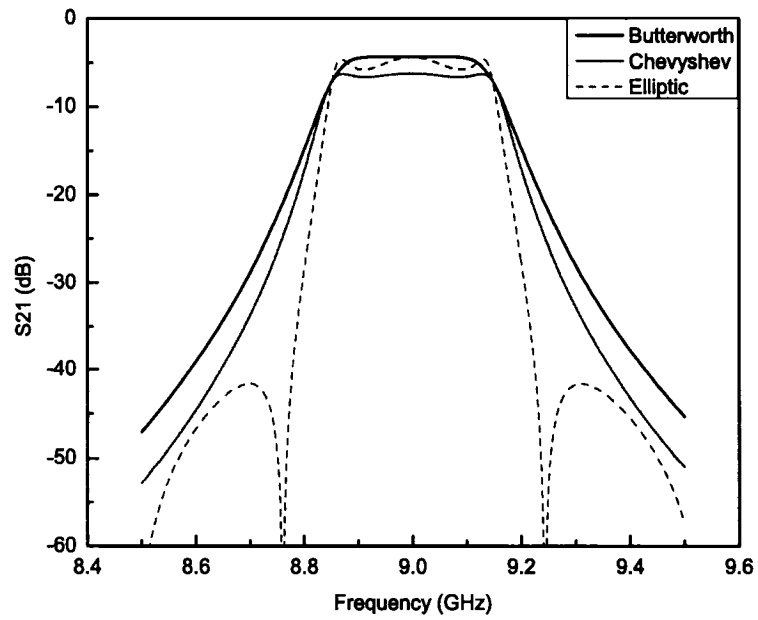
(a)
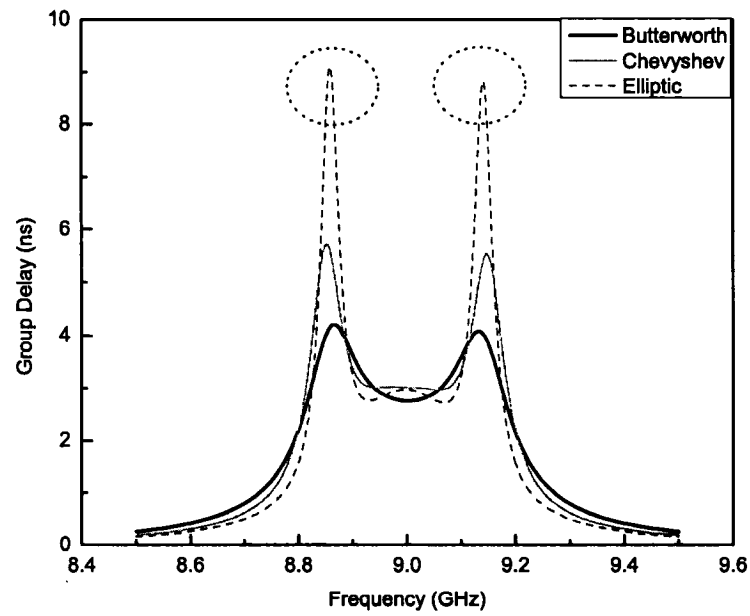
(b)

Figure 5.1: Comparison of (a) S_{21} and (b) group-delay responses of Butterworth, Chevyshev, and elliptic bandpass filters

59

```
Input      ①              ④        Output
    ———————→●------------►●—————————→
            │              ▲
            │              │
            ▼              │
            ●————————————►●
            ②              ③
```

⑪ : Resonant Mode

———— : Direct Coupling
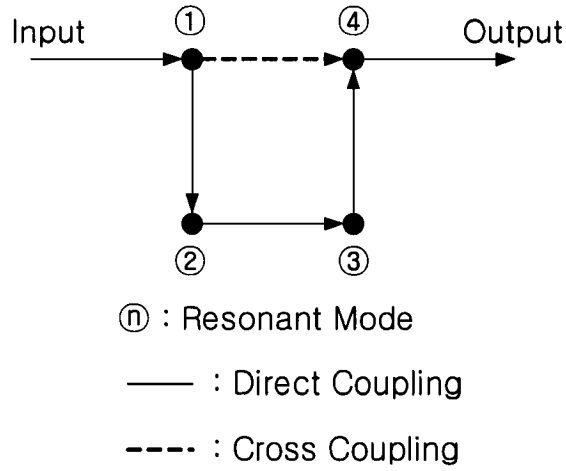
---- : Cross Coupling

Figure 5.2: Coupling structure of a four-pole elliptic filter with a cross coupling

represent resonant modes. Resonators 1-2, 2-3, and 3-4 are connected through direct couplings and resonators 1-4 are cross-coupled. The cross coupling introduces a single pair of transmission zeros, leading to the elliptic response of the filter. The cross-coupling coefficient must have a negative sign when the direct-coupling coefficients are positive.

The four-pole quasi-elliptic filter needs to be be optimized for the design of low phase-noise oscillators. In the usual filter design, the specifications including passband frequencies, stopband frequencies, return loss, and attenuation at stopband edges are taken into account depending on the application. However, phase noise is the important specification to be considered in the low phase-noise oscillator design. Phase noise figure of merit defined in Chapter 2 is calculated based on the S_{21} of the filter, represented by:

$$PNFOM = 10 \cdot log(|S_{21}|) - 20 \cdot log\left(\frac{\omega_0}{2} \cdot \frac{d(\angle S_{21})}{d\omega}\right)$$ (5.3)

where ω_0 is the oscillation frequency.

Given that the S_{21} of the quasi-elliptic filter is a function of passband bandwidth (BW), locations of zero (Ω_t), and return loss(R_L) as shown in (5.7) and (5.4), PNFOM is expressed

60

as a function of these parameters.

$$PNFOM = f(BW, \Omega_t, R_L) \qquad (5.4)$$

In this work, the filter optimization is performed for a four-pole quasi-elliptic bandpass filter with a center frequency of 9 GHz in order to minimize PNFOM. Coupling matrices and input and output (I/O) coupling coefficients are first obtained for various bandwidths, return losses, and locations of zeros as shown in Table 5.1. Based on these design parameters, an Agilent ADS schematic circuit for the filter synthesis is then used to obtain the S_{21} of various filters as shown in Fig 5.3. Here, the lumped RLC elements represent the four synchronously tuned resonators and are determined in terms of the filter design parameters as follows [36].

$$
\begin{aligned}
C_0 &= \frac{Q_e}{\omega_0 Z} \times 10^{12} \ (pF) \qquad L_0 = \frac{Z}{\omega_0 Q_e} \times 10^{12} \ (nH) \\
R_Q &= \frac{Q_u Z}{Q_e} \ (ohm) \qquad\qquad\qquad\qquad\qquad (5.5)
\end{aligned}
$$

where ω_0 is the angular frequency at the midband frequency of filter 9 GHz, Q_e is the external quality factors of resonators at the input and output, and Q_u is the unloaded quality factor of resonators. To obtain the unloaded quality factor for the resonators used in this work, a 9 GHz microstrip open square-loop resonator was designed and simulated on a Rogers RO3003 substrate ($\varepsilon_r = 3.0$, H = 30 mils) using IE3D simulator. The simulated unloaded Q is 320, which is used in the filter optimization.

The quarter-wavelength transmission lines are used to represent the couplings and their characteristic impedances are determined by [36]:

61

Table 5.1: Coupling matrices and I/O coupling coefficients for different passband bandwidths, return losses, and locations of transmission zeros

Ω_t	L_R	BW (%)	M12	M23	M14	Q_e
1.6	10	1	0.0068432	0.0068325	-0.0015286	165.40682
1.6	10	2	0.0136864	0.013665	-0.0030572	82.70341
1.6	10	3	0.0205296	0.0204975	-0.0045858	55.13561
1.6	10	4	0.0273728	0.02733	-0.0061144	41.35170
1.6	10	5	0.034216	0.0341625	-0.007643	33.08136
1.6	5	2	0.0125314	0.0128318	-0.0023448	129.41298
1.6	10	2	0.0136864	0.013665	-0.0030572	82.70341
1.6	15	2	0.0150734	0.0148006	-0.0041778	61.26625
1.6	20	2	0.0166122	0.0162916	-0.0059266	48.33954
1.6	25	2	0.0181522	0.0181888	-0.008646	39.52632
1.2	10	2	0.0121592	0.0158714	-0.0072402	83.76893
1.6	10	2	0.0136864	0.013665	-0.0030572	82.70341
2	10	2	0.0139934	0.0129544	-0.0017712	82.11529
2.4	10	2	0.0141044	0.0126208	-0.0011706	81.90947
2.8	10	2	0.014164	0.0124312	-0.0008364	81.75679

62
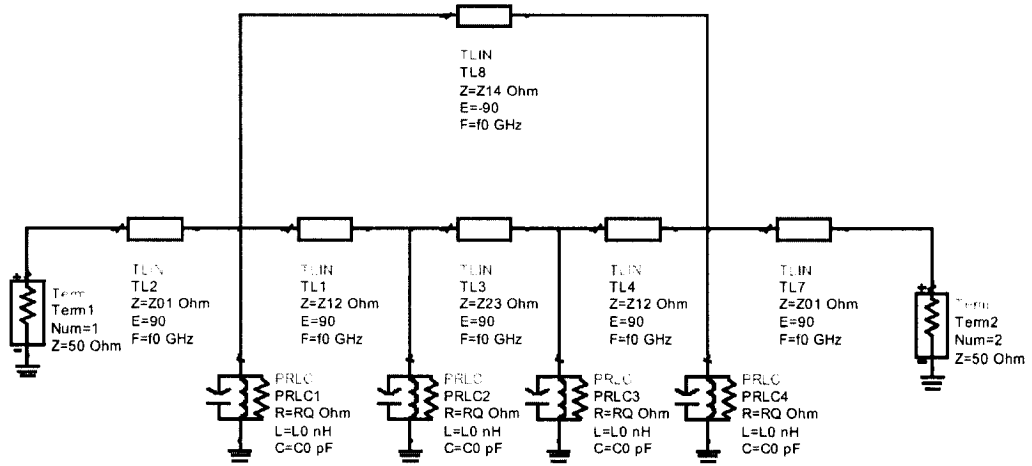
Figure 5.3: Agilent ADS schematic circuit for filter simulations

$$Z01 = Z \qquad Z12 = \frac{Z}{Q_e M12}$$

$$Z23 = \frac{Z}{Q_e M_{23}} \qquad Z14 = \frac{Z}{Q_e |M_{14}|} \qquad (5.6)$$

where $Z = 50$ (Ω) is the I/O terminal impedance.

The effect of filter bandwidth on phase noise is first investigated by varying it from 1 % to 5 %. The insertion loss and group delay and PNFOM of the filters versus passband bandwidth are shown in Fig. 5.4. As bandwidth decreases, the insertion loss and group delay increase simultaneously and the PNFOM decreases, which indicates that narrow filter bandwidth is advantageous for low phase-noise performance. Next to be considered is the effect of the location of transmission zeros on phase noise as shown in Fig. 5.5. When $\Omega_t = 1.2$, transmission zeros are not clearly observed and the filter S_{21} response somewhat resembles a Chevyshev response, thereby producing the highest PNFOM and the worst phase noise. Except the $\Omega_t = 1.2$ case, other locations of transmission zeros present similar responses. Finally, the effect of return loss on PNFOM is investigated as shown in Fig. 5.6. As the return loss decreases, the filter shows a sharper selectivity, thus resulting in a

63

higher group delay at the cost of insertion loss.

PNFOM is plotted as a function of passband bandwidth, location of transmission zeros, and return loss by taking the minimum values of PNFOM for various filters, as shown in Fig. 5.7. It is observed that PNFOM increases with passband bandwidth and PNFOM decreases with location of transmission zeros up to $\Omega_t = 2.0$, from which it almost flattens out. For the variation of return loss, PNFOM shows the minimum value when the return loss is 10 dB. Based on the simulations for filter optimization, the optimum condition occurs when the bandwidth is as narrow as possible, $\Omega_t > 2.0$, and $R_L \approx 10dB$.

64
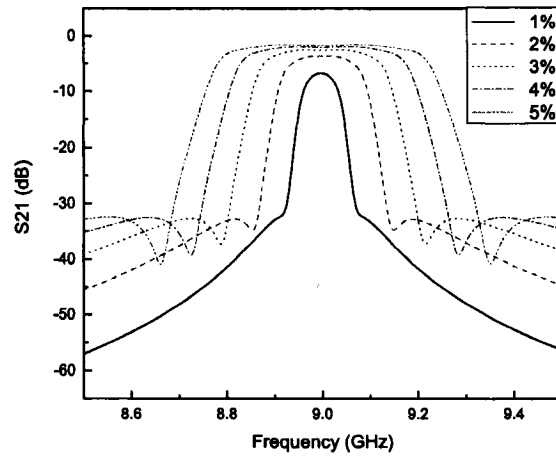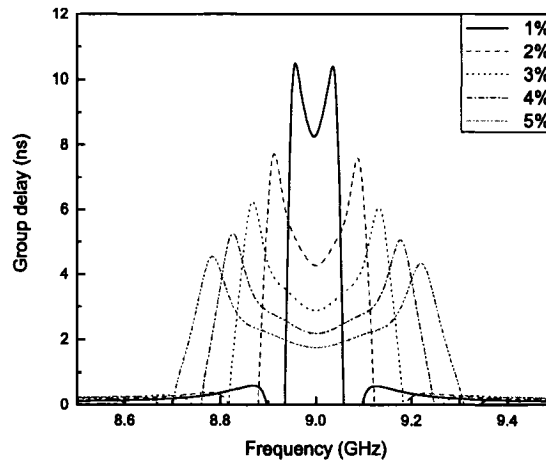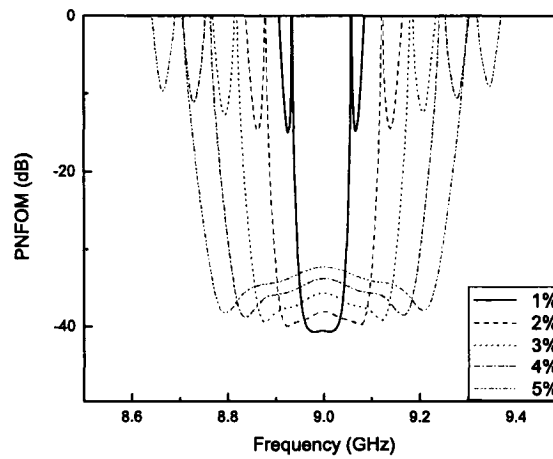
Figure 5.4: (a) Insertion loss, (b) group delay, and (c) PNFOM versus passband bandwidth

65
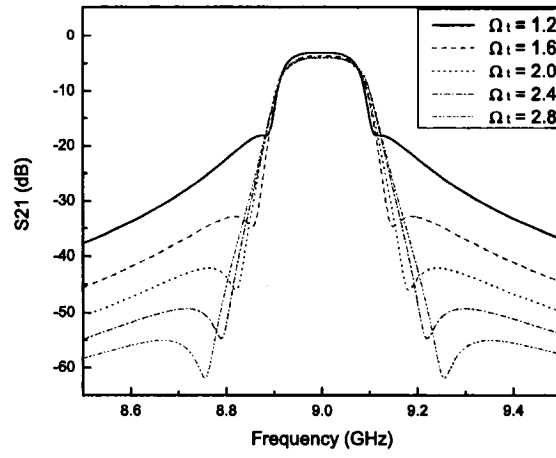
(a)
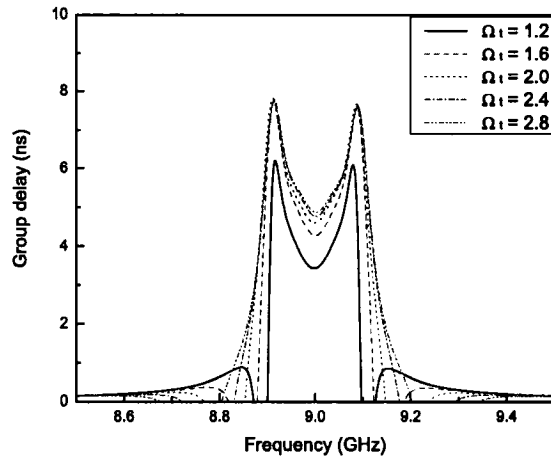
(b)
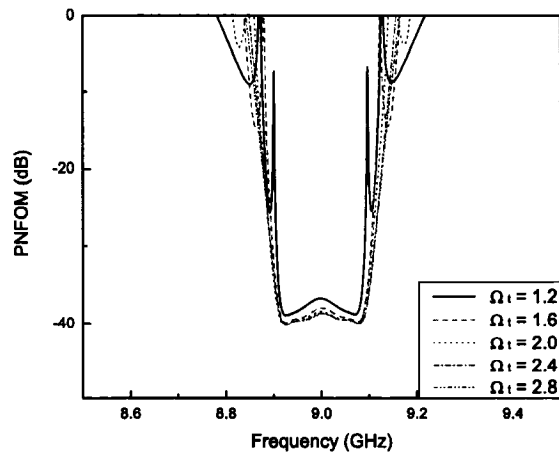
(c)

Figure 5.5: (a) Insertion loss, (b) group delay, and (c) PNFOM versus location of transmission zeros

66
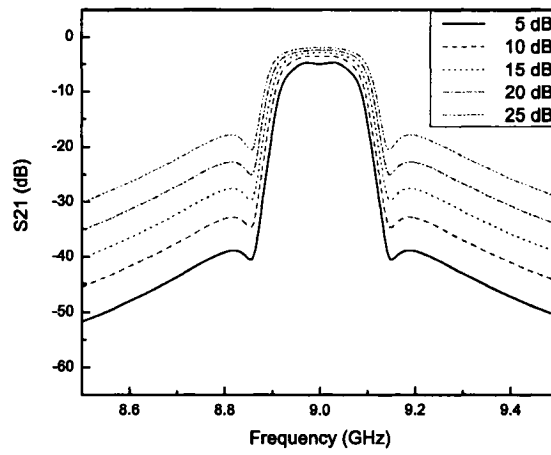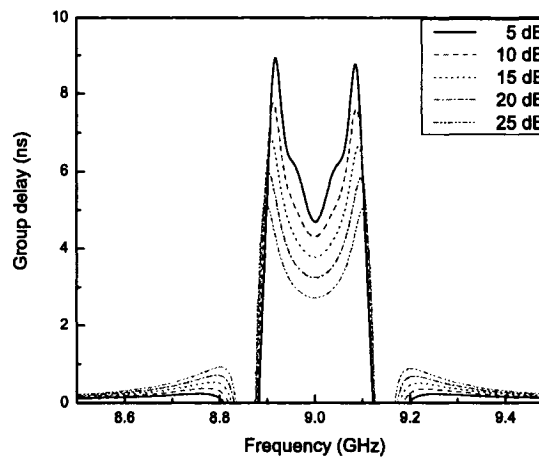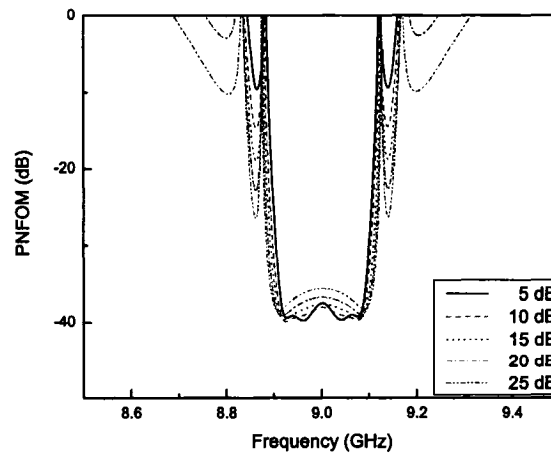
Figure 5.6: (a) Insertion loss, (b) group delay, and (c) PNFOM versus return loss

67
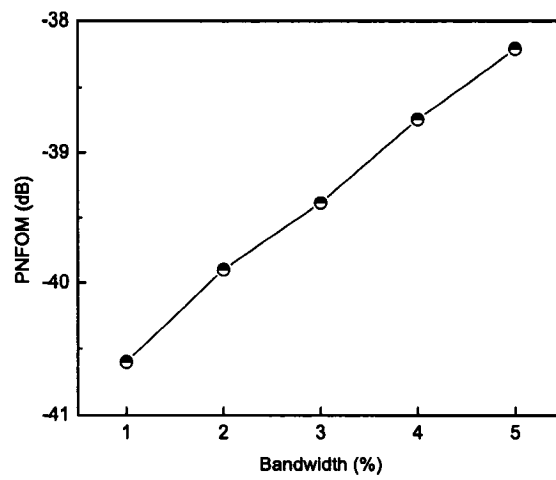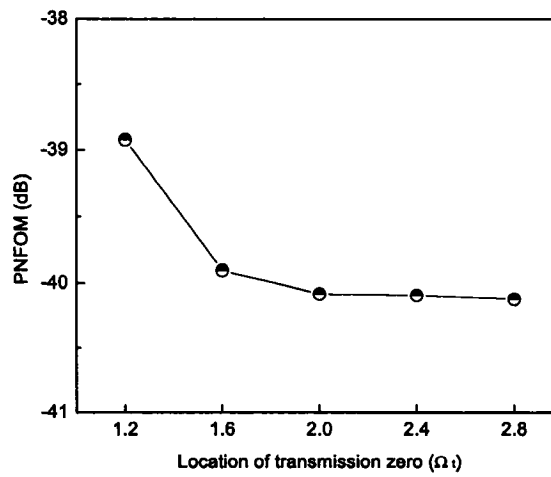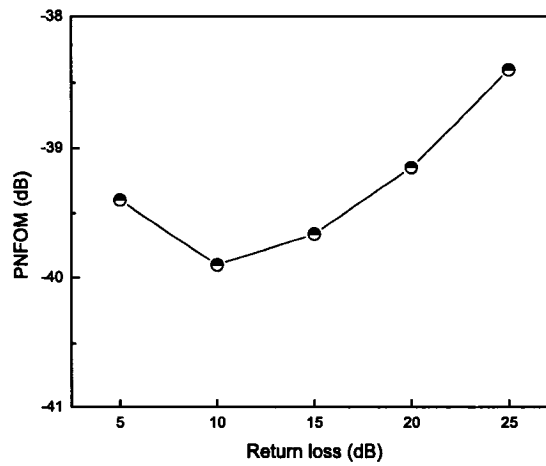
Figure 5.7: PNFOM versus (a) passband bandwidth, (b) location of transmission zeros, and (c) return loss

68

5.3   Circuit Design

5.3.1   Elliptic Bandpass Filter Design

An elliptic bandpass microstrip filter with a center frequency of 9 GHz is designed on a Rogers RO3003 substrate (ε_r = 3.0, H = 30 mils) to realize an X-band low phase-noise oscillator. Open square-loop resonators are used to realize both positive and negative couplings for elliptic response. Here, the location of transmission zeros and the return loss are selected at Ω_t = 2.2 and R_L = 30 dB. A bandwidth of 2 % is chosen to provide 5 dB insertion loss, because the maximum available gain of the active device used in this work (NESG2030M04) is 7.5 dB. These filter specifications are not fully optimized for low phase noise performance because the filter design was done before the analysis of the filter optimization was performed. For the above specification, the coupling matrix (M), and I/O coupling coefficients (Q_e) are given by:

$$M = \begin{bmatrix} 0 & 0.0182 & 0 & -0.0027 \\ 0.0182 & 0 & 0.0154 & 0 \\ 0 & 0.0154 & 0 & 0.0182 \\ -0.0027 & 0 & 0.0182 & 0 \end{bmatrix} \tag{5.7}$$

$$Q_e = 82.11529 \tag{5.8}$$

Based on the above coupling matrix and I/O coupling coefficient, full-wave EM simulations using IE3D^{TM} are performed to determine the physical layout. The spacing between resonator i and j is determined by satisfying the following condition [36].

$$M_{ij} = \frac{f_{p2}^2 - f_{p1}^2}{f_{p2}^2 + f_{p1}^2} \tag{5.9}$$

69

9.9 mm

10.7 mm
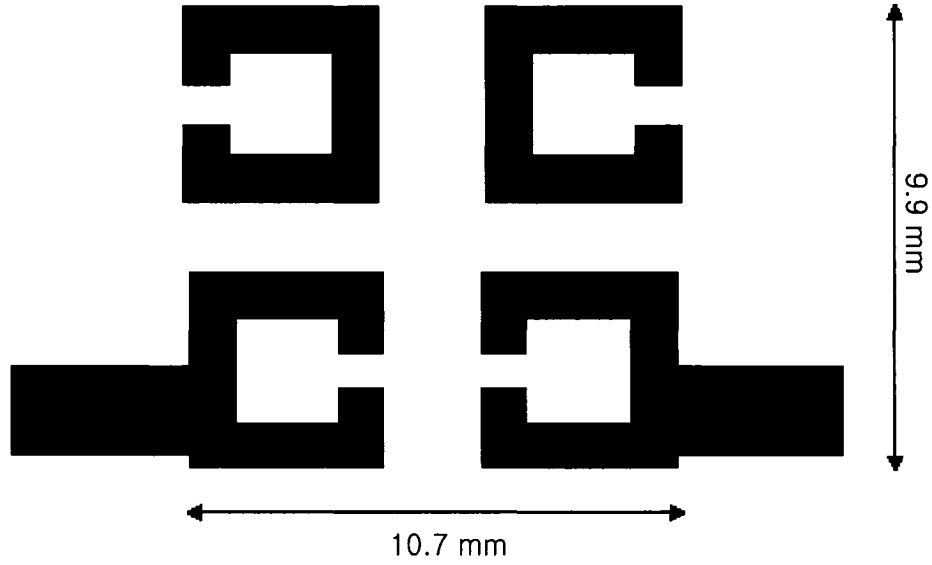
Figure 5.8: Layout of the four-pole elliptic bandpass filter

where M_{ij} is the coupling coefficient between resonator i and j, and f_{p1} and f_{p2} are the lower and higher split resonant frequencies when only resonator i and j are coupled. The tapping location is determined by using S_{11} of the input or output resonator when the resonator is singly loaded with a tapped transmission line [36].

$$Q_e = \frac{f_0}{\Delta f_{+90°} - \Delta f_{-90°}} \tag{5.10}$$

where $\Delta f_{+90°}$ and $\Delta f_{-90°}$ are the frequencies at which the phase of S_{11} shows $+90°$ and $-90°$ difference with respect to the phase at the center frequency f_0 [37].

The layout of the elliptic filter is shown in Fig. 5.8. The overall physical size of the filter is $10.7\ mm \times 9.9\ mm$. The open gaps of two open-loop resonator 1 and 4 face each other in order to provide the negative coupling coefficient from their electric coupling. Fig. 5.9 shows the simulation and measurement results for the elliptic filter. Notably, one transmission zero is not found in the lower stopband, which is attributable to a frequency-dependent cross coupling [39]. In Fig. 5.9(b), the group-delay peaks are shown at both ends of the passband and the upper passband has a higher group-delay peak. Using the group delay and the insertion loss of the filter, PNFOM is calculated and shown in Fig. 5.10. The lowest

70
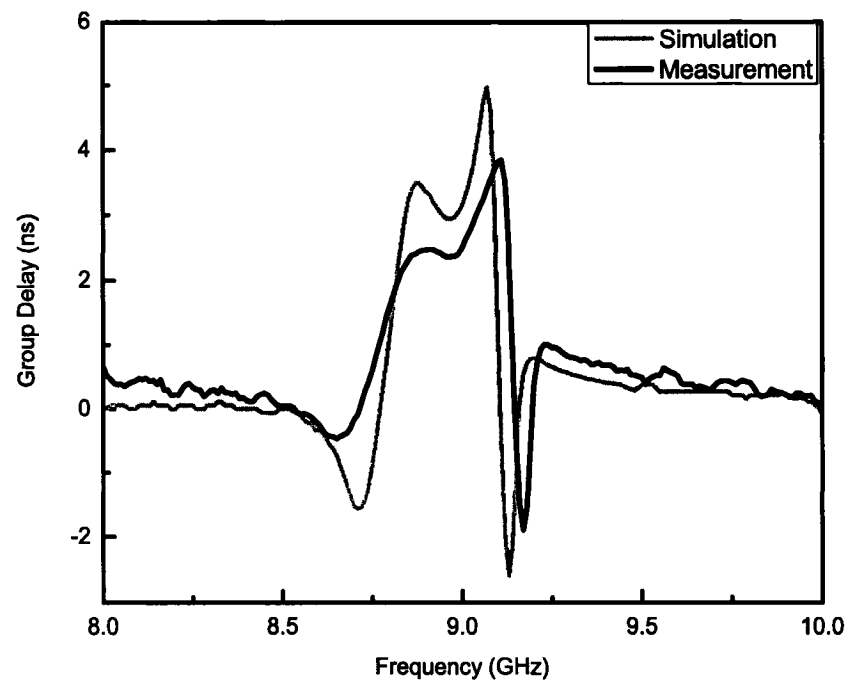
(a)
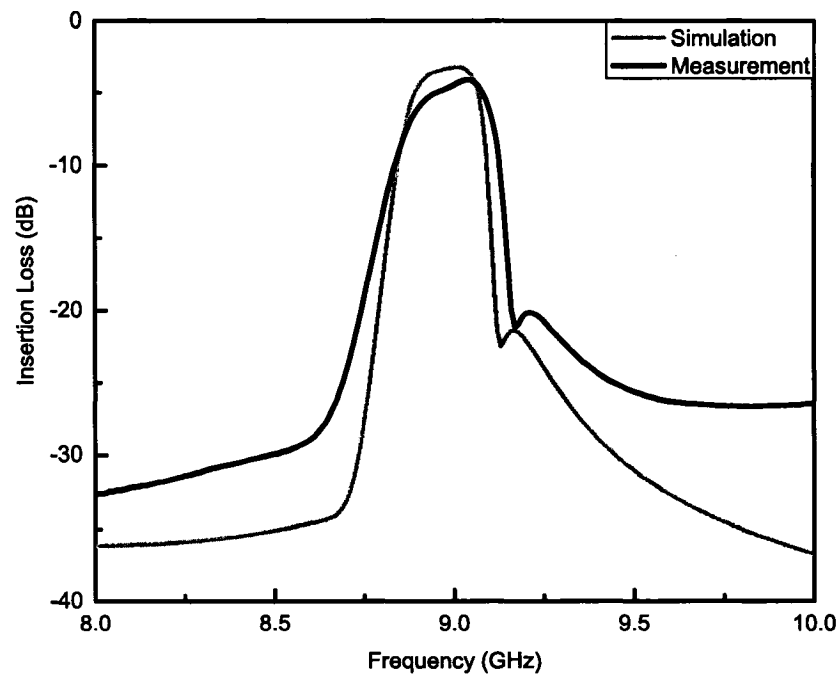
(b)

Figure 5.9: Simulation and measurement results for the four-pole elliptic bandpass filter :
(a) insertion loss (b) group delay

71
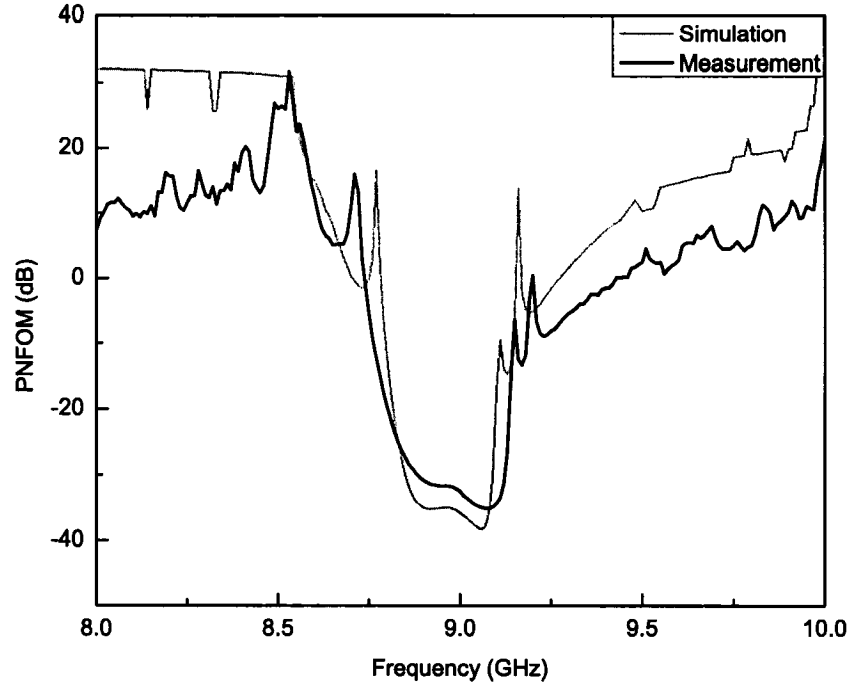
Figure 5.10: Phase noise figure of merit of the four-pole bandpass filter

PNFOM is at 9.07 GHz close to the frequency of the highest group delay, suggesting the optimum oscillation frequency.

5.3.2 Oscillator Design

An X-band microwave oscillator is designed based on the elliptic bandpass filter described in the previous section. Due to the bandpass response of the filter, a parallel feedback configuration is chosen to design the external feedback network. A circuit schematic of the oscillator employing the elliptic bandpass filter is shown in Fig. 5.11.

The oscillator design procedure is summarized here. First, the input and output of the transistor are bilaterally conjugate-matched to 50 Ω. The elliptic filter is then placed at the base terminal as a frequency-stabilization element. In this way, any impedance mismatch between the transistor and the filter can be prevented. The amplifier formed in this way (marked by the solid-line box in Fig. 5.11) is simulated using the harmonic balance simulator. The voltages and currents at the input and output terminals of the amplifier part (V_1,

72

Amplifier part

Four-pole bandpass filter

(V_2, I_2)

Π feedback network

Base T-line 2   Base T-line 1 $Y_L = G_L + jB_L$

jB_2

SiGe HBT
(NESG2031M05)   Output Matching Network   Collector T-line 1 jB_1

Input Matching Network

Bilaterally conjugated matched amplifier

(V_1, I_1)
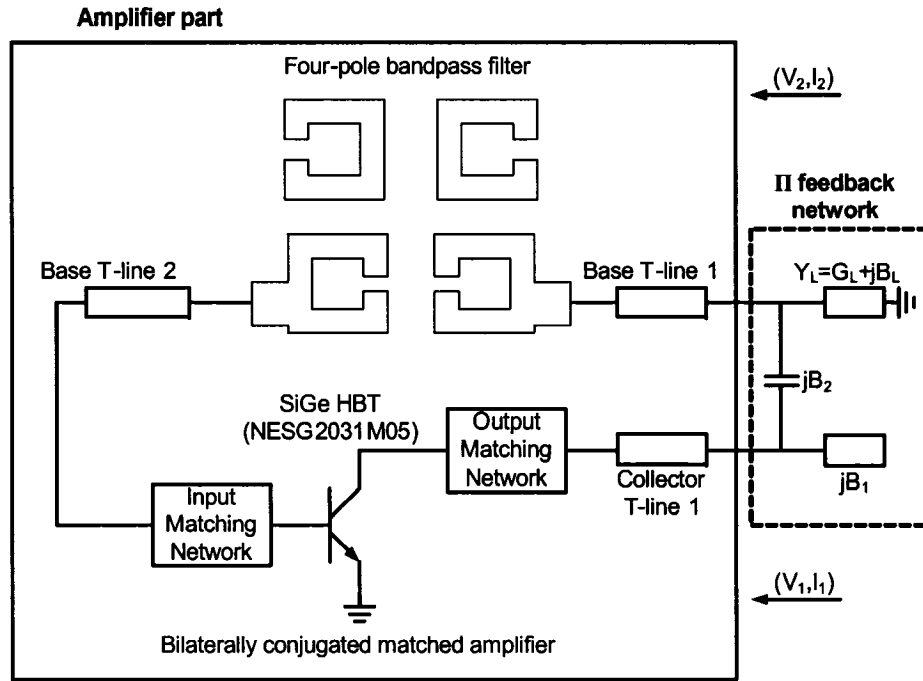
Figure 5.11: Circuit schematic of the X-band SiGe HBT oscillator employing the four-pole elliptic bandpass filter.

Table 5.2: Input and Output Terminal Voltages, Currents and Element Values of the Π-Feedback Network

$V_1(V)$	$I_1(mA)$	$V_2(V)$	$I_2(mA)$
$0.492e^{-7.37°}$	$8.2e^{8.84°}$	$0.594e^{-23.8°}$	$-11.9e^{-23.8°}$
B_1	B_2	G_L	B_L
2.775 mS	46.875 mS	9.028 mS	-9.642 mS

V_2, I_1, I_2) are determined at a specific RF input power level. Finally, the Π-feedback network is synthesized using the simulated voltages and currents [30]. The simulated terminal voltages and currents and the determined element values of the embedding Π feedback network are presented in Table. 5.2.

5.4 Experimental Results

The oscillator employing the four-pole elliptic-response bandpass filter is fabricated on a Rogers RO3003 substrate with a dielectric constant of 3.0 and a thickness of 30 mils. The active device is a packaged SiGe HBT (NEC NESG2030M05) biased at a collector-emitter voltage (V_{ce}) of 2 V with a collector current of 15 mA. The top view of the fabricated oscillator circuit is shown in Fig. 5.12.

The oscillator is measured with a spectrum analyzer (Agilent 8564E). The output spectrum of the oscillator is shown in Fig. 5.13. The measured oscillation frequency is 9.05 GHz with the output power of 3.5 dBm after deembeding cable and bias tee. The total consumed dc power is 30 mW, corresponding to an rf-dc efficiency of 7.5%. The oscillator phase noise is measured based on the FM discriminator technique with a phase noise measurement system (Agilent E5504A). As shown in Fig. 5.14, the measured phase noise is -116 dBc/Hz and -140 dBc/Hz at 100 kHz and 1 MHz offset frequency, respectively. The measured phase noise shows a good agreement with the simulations at 1 MHz offset frequency in the $1/f^2$ region, as shown in Fig. 5.14. At the oscillation frequency, the simulated oscillator loaded Q of the filter is 130. The $1/f^3$ phase noise corner frequency is formed in the proximity of 200 kHz. This oscillator is evaluated in terms of the oscillator FOM defined in (4.27). The FOM of the four-pole filter oscillator is calculated as -204.4 dB/Hz. The measured performance for the oscillator is summarized in Table 5.3. In this experiment, the filter response was not fully optimized for the low phase noise performance. The simulated result for an oscillator employing an optimized elliptic filter shows 3 dB phase noise improvement as compared to the demonstrated oscillator.

74
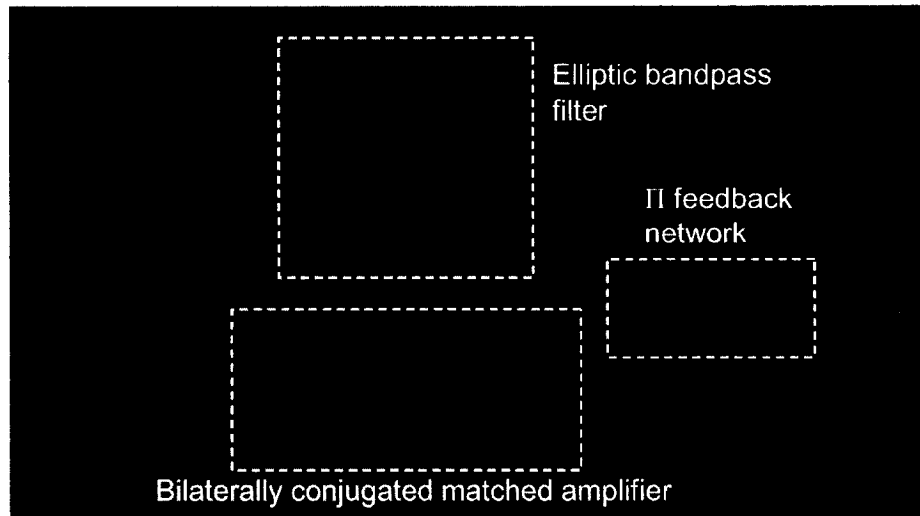
Figure 5.12: Photograph of the designed X-band SiGe HBT oscillator.
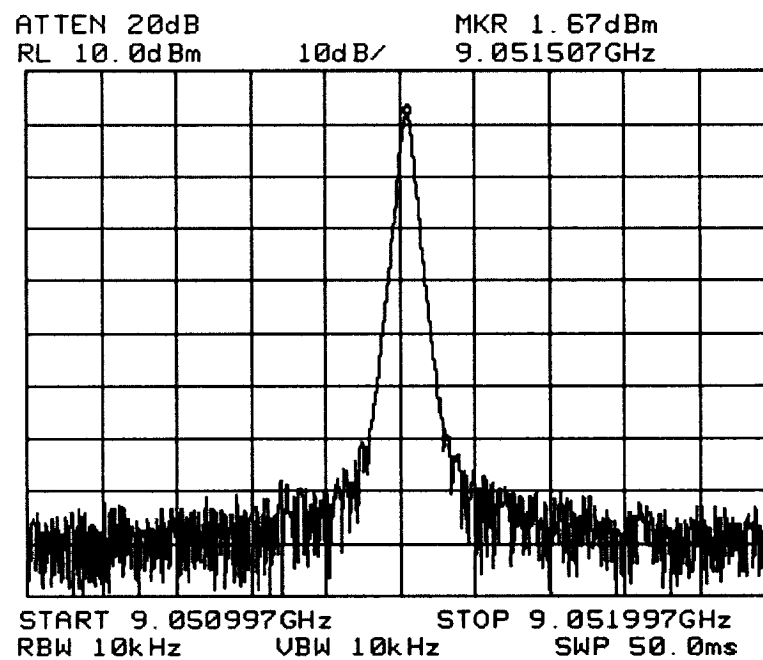
Figure 5.13: Measured output spectrum of the oscillator.

75
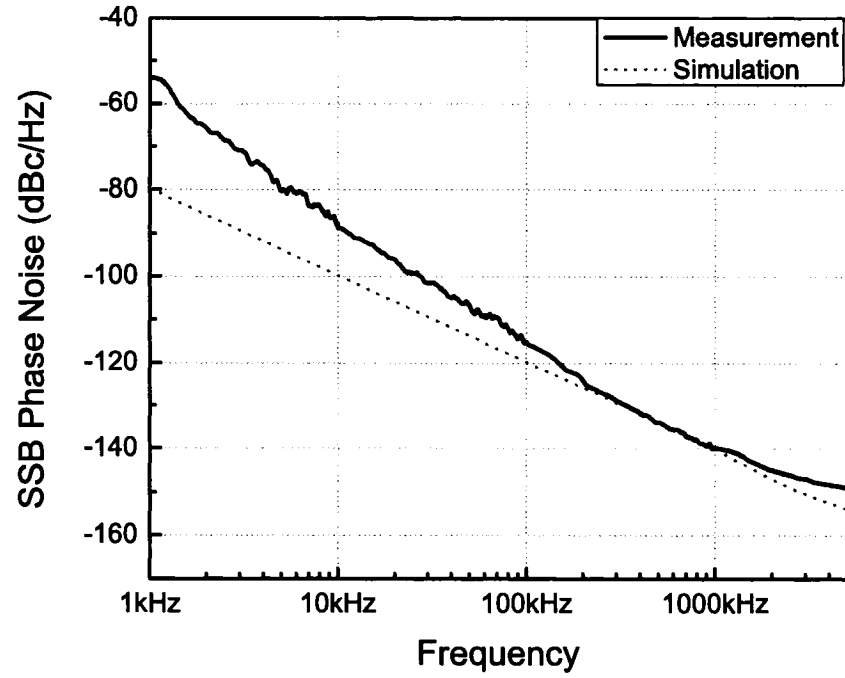
Figure 5.14: Measured and simulated phase noise for the SiGe HBT X-band oscillator.

Table 5.3: Performance Summary for the X-band four-pole bandpass filter oscillator

Frequency	9.05 GHz
Output power	3.5 dBm
DC power consumption	30 mW
DC-RF efficiency	7.5 %
Phase noise	-116 dBc/Hz @100 kHz
	-140 dBc/Hz @1 MHz
Second harmonic rejection	-14.5 dBc
Third harmonic rejection	-25 dBc
FOM	-204.4 dBc/Hz

76

5.5 Comparison with Other works

Table 5.4 compares the performance of the SiGe HBT four-device extended-resonance oscillator and the four-pole elliptic-filter oscillator with other reported microwave planar free-running oscillators at C-band and X-band. The four-device extended resonance oscillator and the oscillator employing the four-pole elliptic filter show the phase noise performance of - 119 dBc/Hz and - 116 dBc/Hz at 100 kHz offset frequency, respectively. To the author's best knowledge, the two demonstrated oscillators present the lowest phase noise performance among other published X-band microwave planar hybrid free-running oscillators.

Table 5.4: Comparison with other reported microwave planar hybrid oscillators

Device	Resonator	F_o (GHz)	P_o (dBm)	Eff (%)	$L(f)$ (dBc/Hz @100kHz)
Si BJT[41]	Hairpin resonator	9	9	4.5	-112
Si BJT[42]	Microstrip resonator	9.95	7	-	-113
HEMT[43]	Ring resonator	12	5.33	48.7	-96.17
HEMT[44]	Active resonator	10	10	2	-114.4
Si BJT[45]	Open-loop resonator	5.84	-0.5	-	-113.2
SiGe HBT (Extended resonance oscillator)	Extended resonance	9.1	9.7	14	-119
SiGe HBT (Four-pole filter oscillator)	Microstrip bandpass filter	9.05	3.5	7.5	-116

5.6 Conclusion

In this chapter, a low phase noise microwave oscillator employing a four-pole elliptic microstrip bandpass filter was presented. The filter optimization for the design of low phase-noise oscillators was also presented using the insertion loss and group delay of elliptic filters. It was shown that an oscillator loaded Q of 130 is achievable at the passband edges of the elliptic filter. The demonstrated X-band oscillator using a SiGe HBT packaged device showed an excellent phase noise of -140 dBc/Hz at 1 MHz offset frequency. In future research, a low phase-noise oscillator employing an elliptic bandpass filter optimized for low phase-noise performance will be demonstrated. Also, the relatively large dimension of the proposed oscillator needs to be reduced by utilizing the recent advancements in filter miniaturization techniques [46]-[48].

Chapter 6

Design of Push-Push and Triple-Push Oscillators for Reducing $1/f$ noise upconversion

6.1 Introduction

The rapid growth in communication systems demands wider bandwidths for faster data rates. Consequently, wireless systems are forced to operate at higher and higher frequencies. Recently, push-push and triple-push oscillators have brought much attention because they allow for an extended operation frequency range of active devices [49]-[51].

Push-push oscillators employ two sub-oscillators with the balanced operation and only the second harmonics are combined at the output load. In triple-push oscillators, only the third harmonic signals are combined at the output load by achieving a phase difference of 120° among three fundamental signals. Since the resonators in push-push and triple-push oscillators operate at half and one-third the design frequency, higher resonator Qs are achievable. In addition, designing at half and one-third the desired frequency allows for increased device gains [51]. Because of these advantages, the approach based on push-push and triple-push principle has been identified as an attractive method for low phase noise oscillator design at microwave and millimeter-wave frequencies.

The low frequency $1/f$ noise plays a dominant role in determining the close to carrier phase noise performance in oscillators. It is well known that $1/f$ noise is upconverted to the carrier frequency, resulting in a $1/f^3$ region near the carrier frequency. Recently, a

79

linear time-variant (LTV) theory for phase noise was introduced [11]. Based on this theory, the $1/f$ noise upconversion is strongly dependent on the symmetry property of the oscillation waveform. Further, mathematical analysis suggests that the $1/f$ noise upconversion is closely related to even harmonic components due to the relationship between waveform symmetry and harmonic content [53]. Therefore, $1/f$ noise upconversion in push-push and triple-push oscillators needs to be carefully taken into account because push-push and triple-push oscillators use the harmonic signals from two or three fundamental sub-oscillators for doubling or tripling the operation frequency. Moreover, the fact that common microwave devices such as MESFETs and HEMTs have high $1/f$ noise corner frequency up to several MHz suggests that this issue must be studied in detail. To the author's best knowledge, this is the first work that takes advantage of naturally generated harmonic waveforms in push-push and triple-push oscillators to optimize the phase noise performance.

In this chapter, the effect of waveform symmetry on phase noise in push-push and triple-push oscillators is investigated. In Section 6.2, the 1/f noise upconversion process based on LTV theory is briefly reviewed, and the significance of waveform symmetry in push-push and triple-push oscillators is discussed. In Section 6.3, the design of low phase-noise push-push and triple-push oscillators is described in terms of $1/f$ noise upconversion. Section 6.4 presents and discusses the simulation and measurement results of the microwave push-push and triple-push oscillators based on GaAs MESFET.

6.2 Theory

6.2.1 Waveform Symmetry and $1/f$ Noise Upconversion

Hajimiri's time-variant phase noise theory can be adopted in order to explain the characteristics of $1/f$ noise upconversion in push-push and triple-push oscillators [11]. This theory was summarized in details in Chapter 2. As mentioned earlier, the phase noise in

$1/f^3$ region is represented by:

$$L(\Delta\omega) = 10 \, log \left(\frac{c_0^2}{8q_{max}^2} \cdot \frac{\overline{i_n^2}/\Delta f}{\Delta\omega^2} \cdot \frac{\omega_{1/f}}{\Delta\omega} \right) \tag{6.1}$$

Also, the relationship between the device noise $1/f$ corner frequency and the $1/f^3$ phase noise corner frequency can be characterized using the Fourier coefficients of the ISF.

$$\omega_{1/f^3} = \omega_{1/f} \cdot \frac{c_0^2}{2\Gamma_{rms}^2} \tag{6.2}$$

where c_0 is twice the direct current (dc) value of the ISF and Γ_{rms} is the root mean square (rms) value of the ISF.

Based on the above equation, $1/f$ noise upconversion can be significantly suppressed by minimizing c_0. Since the value of c_0 is twice the dc value of the ISF over a period, c_0 is strongly dependent on the symmetry of the oscillation waveform. In other words, the symmetry of the waveform rise and fall times and their slopes reduces the value of c_0, which contributes to reducing $1/f$ noise upconversion.

Based on Hajimiri's theory, two conditions for minimizing the dc value of the ISF were proposed [53]. The first condition requires the oscillation waveform to have an even symmetry about a point shifted ϕ radian from the origin, represented by:

$$f(t) = \sum_{n=0}^{\infty} a_n \cos(n\omega t - n\phi) \tag{6.3}$$

It should be noted that all harmonic components in (6.3) are included but their phases should be identical for the first condition of waveform symmetry to be satisfied. On the other hand, the waveform corresponding to the second condition is represented by:

$$f(t) = \sum_{n=1,3,5,\ldots}^{\infty} a_n \cos(n\omega t + \theta_n) \tag{6.4}$$

where θ_n is the phase of the nth harmonic. This waveform is composed of only odd har-

81

monics with arbitrary phases. In this case, the rising and falling slopes are opposite, leading to zero dc value of ISF.

To explain two waveform conditions graphically, four examples of simple waveforms are depicted in Fig. 6.1. The waveforms in Fig. 6.1(a)- (c) are the examples for explaining the first waveform symmetry condition. These waveforms are expressed in the Fourier series representations, represented by:

$$f(x) = \cos(x) + 0.4 \cdot \cos(2x + \theta_0) \tag{6.5}$$

where $\theta_0 = 0°, 45°$, and $90°$.in Fig. 6.1(a)-(c). The waveform in Fig. 6.1(d) is the example of the second waveform symmetry condition and is represented by:

$$f(x) = \cos(x) + 0.4 \cdot \cos(3x + 45°) \tag{6.6}$$

The waveform in Fig. 6.1(a) satisfies the first waveform symmetry condition because of the equal phases in the fundamental and the second harmonic components. This waveform shows that its rise and fall times are symmetrical, leading to small c_0. Two waveforms in Fig. 6.1(b) and (c) do not satisfy the second waveform symmetry condition because of their even harmonic components. They also violate the first waveform symmetry condition because the fundamental and second harmonic components have different phases. These two waveforms, therefore, show the asymmetry in the rise and fall times, which causes $1/f$ noise upconversion to become significantly large. The waveform in Fig. 6.1(d) satisfies the second waveform symmetry condition without any even harmonic component. Consequently, the rise and fall slopes as well as the rise and fall times are symmetrical, resulting in small c_0.

The oscillation waveform in (6.7) is now considered in order to relate the amplitude and phase of the even harmonic component to phase-noise performance in the $1/f^3$ region.

82
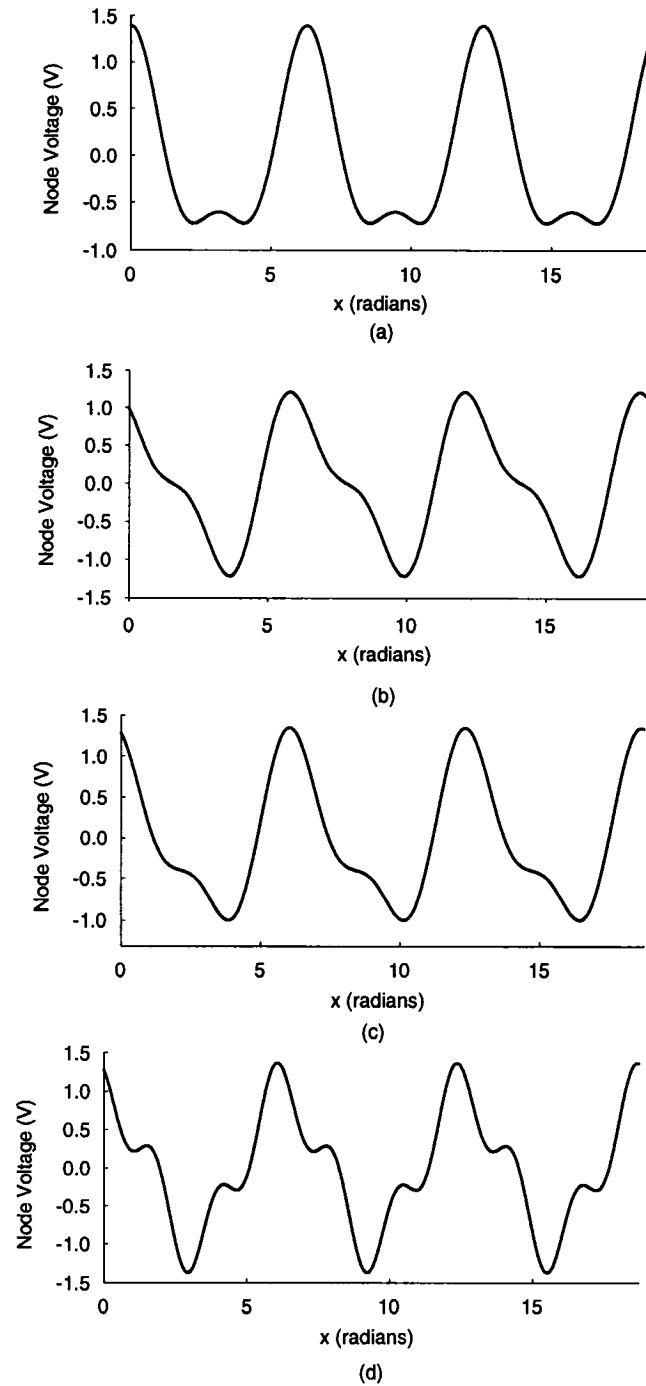
Figure 6.1: Examples of symmetrical and asymmetrical oscillation waveforms (a) Symmetrical waveform that satisfies the first waveform symmetry condition [$\theta_0 = 0°$ in (6.5)] (b) Asymmetrical waveform [$\theta_0 = 45°$ in (6.5)] (c) Asymmetrical waveform [$\theta_0 = 90°$ in (6.5)] (d) Symmetrical waveform that satisfies the second waveform symmetry condition in (6.6)

83
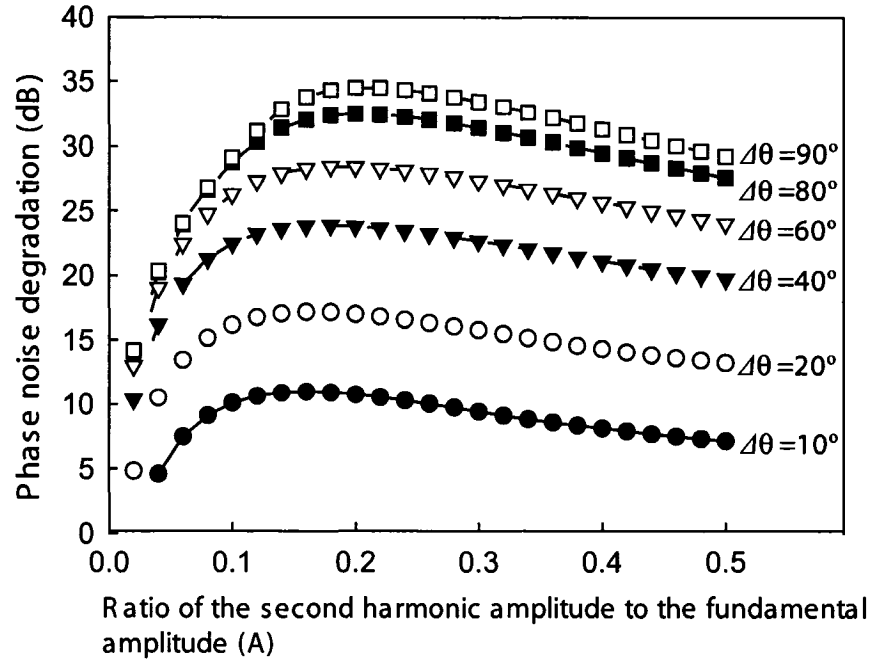
Figure 6.2: Relationship between phase noise degradation in $1/f^3$ region and the second harmonic amplitude and phase

$$f(x) = \cos(x) + A \cdot \cos(2x - \Delta\theta))$$
(6.7)

Herein it is assumed that when c_0 is equal to 0.02, the phase noise due to white noise is equal to the phase noise due to $1/f$ noise upconversion at a specific offset frequency $(\Delta\omega)$. The phase noise at this point is denoted as $L_{ref}(\Delta\omega)$. By calculating the dc value of the ISF of (6.7) using an approximate method given in [11], the phase noise degradation over $L_{ref}(\Delta\omega)$ can be obtained as a function of the second harmonic amplitude (A) and phase $(\Delta\omega)$ as shown in Fig. 6.2. This figure indicates that the second harmonic amplitude or the phase difference between the fundamental and second harmonic signals should be minimized to improve phase noise in the $1/f^3$ region.

6.2.2 $1/f$ Noise Upconversion in Push-Push Oscillators

A push-push oscillator is a frequency doubling oscillator that consists of two symmetrical sub-oscillators with out-of-phase operation. Fig. 6.3 shows the basic configuration for push-push oscillators. Each sub-oscillator is designed to operate at half the design frequency. By coupling two sub-oscillators, the two output signals have a phase difference of 180° and are represented by:

$$V_1(t) = A_1 e^{j\omega_0 t} + A_2 e^{j2\omega_0 t} + A_3 e^{j3\omega_0 t} + A_4 e^{j4\omega_0 t} + \cdots \tag{6.8}$$

$$V_2(t) = A_1 e^{j(\omega_0 t - \pi)} + A_2 e^{j2(\omega_0 t - \pi)} + A_3 e^{j3(\omega_0 t - \pi)} + A_4 e^{j4(\omega_0 t - \pi)} + \cdots \tag{6.9}$$

By combining the two signals, the fundamental and odd harmonic components are canceled, but the even harmonics are added constructively at the output network, thus delivering the second harmonic signals to the output load R_L as follows.

$$V_{out}(t) = 2 A_2 e^{j2\omega_0 t} + 2 A_4 e^{j4\omega_0 t} + \cdots \tag{6.10}$$

From the viewpoint of phase noise, one advantage of push-push oscillators is that a high Q can be achieved since the resonator is designed at half the design frequency [52]. There-
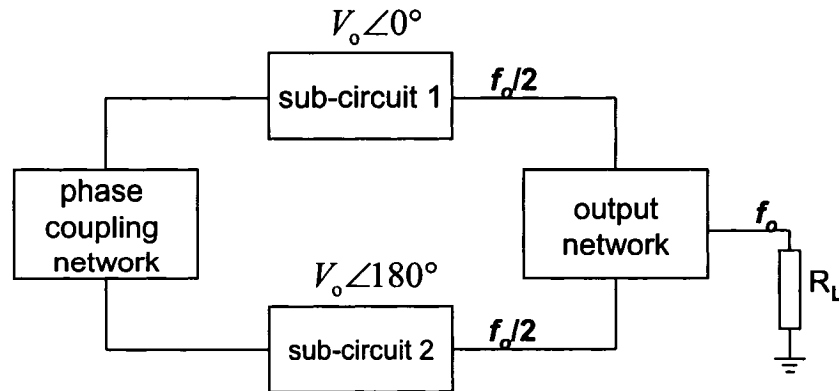
Figure 6.3: Basic configuration of a push-push oscillator

85

fore, it is believed that the push-push principle provides a low phase-noise performance as well as an extended frequency range. In this dissertation, it is however suggested that the push-push oscillator may be vulnerable to a large $1/f$ noise upconversion, if not carefully designed.

Generally, one of the figures of merit in fundamental microwave oscillators is the second harmonic rejection for reduced interference. This requirement results in an oscillation waveform that satisfies the second waveform symmetry condition. However, the situation is different in push-push oscillators. As discussed in [11], $1/f$ noise upconversion is closely related to the waveform symmetry of each sub-oscillator. Although the final output signal of the push-push oscillator is symmetrical, since push-push oscillators employ the second harmonic components in two sub-oscillators for doubling the output frequency, the second harmonic power levels in sub-oscillators need to be increased for improved dc-rf efficiency. Based on the fact that the second waveform symmetry condition applies only to odd harmonics, it is, in principle, violated in the push-push oscillator design. The presence of the strong second harmonics distorts the waveforms of two sub-oscillators, leading to a considerable asymmetry in the rise and fall times. To rectify this problem, one can instead pursue the first waveform symmetry condition in the design of push-push oscillators. Therefore, it is proposed to minimize $1/f$ noise upconversion in push-push oscillators by ensuring that the fundamental and harmonic components generated by each sub-oscillator have equal phases.

6.2.3 $1/f$ Noise Upconversion in Triple-Push Oscillators

Recently, the concept of triple-push oscillator design was proposed and implemented [51]. Fig. 6.4 shows the basic configuration for triple-push oscillators. Triple-push oscillators consist of three sub-oscillators with 120° phase difference. By achieving 120° phase difference, the fundamental and second harmonic components are canceled and only the third harmonic components from the three sub-oscillators are combined at the output load.

86
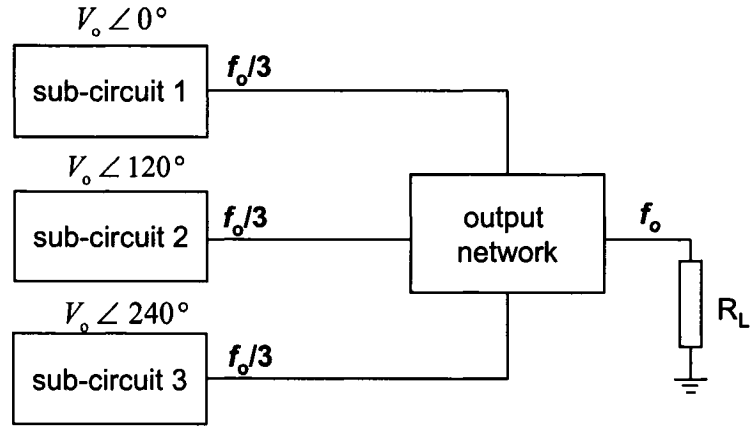
Figure 6.4: Basic configuration of a triple-push oscillator

Since the resonator is designed at one-third the design frequency in triple-push oscillators, it can provide high Q values [51].

When triple-push oscillators are analyzed in terms of $1/f$ noise upconversion, they have a merit that the even harmonic components are not used for the output signal. Therefore, one can eliminate the second harmonic components that exist in individual sub-oscillators by properly designing triple-push oscillators in order to satisfy the second waveform symmetry condition.

6.3 Design Approach

6.3.1 Push-Push Oscillator

As proposed in the previous section, by satisfying the first waveform symmetry condition in push-push oscillators, $1/f$ noise upconversion can be minimized. This condition is satisfied by minimizing the phase difference between the fundamental and harmonic waveforms at the device port (i.e. drain). Approximate phase-noise improvement as a function of amplitude and phase of second harmonic with respect to the fundamental signal is given in Fig. 6.2. Because in a push-push oscillator, the second harmonic power should be maximized, the value of $\Delta\theta$ should be reduced to suppress the $1/f$ noise upconversion. In

87

this work, the sub-oscillator is designed to have 50 Ω output load to eliminate any output matching circuitry. The reactive value of gate and source terminations are, then, optimized to maximize the second harmonic power level, while minimizing the dc value of ISF. This is done through the parameter sweep function in Agilent-ADS. To demonstrate the aforementioned design procedure to minimize $1/f$ noise upconversion, two push-push oscillators are designed to have symmetrical and asymmetrical waveforms at the drain ports, respectively.

Fig. 6.5 shows the circuit layout of the designed push-push oscillators. The microstrip lines are coupled at the source ports to provide the balanced operation. The outputs of two coupled sub-oscillators are combined through a Wilkinson power combiner. The gate shorted-stubs are used to enhance instability as feedback elements. Fig. 6.6(a) shows the simulated voltage waveforms at two drain ports of the asymmetrical push-push oscillator. Two waveforms show 180° phase difference because of the balanced operation. The asymmetry of rise and fall times in the waveforms is shown in Fig. 6.6(a).
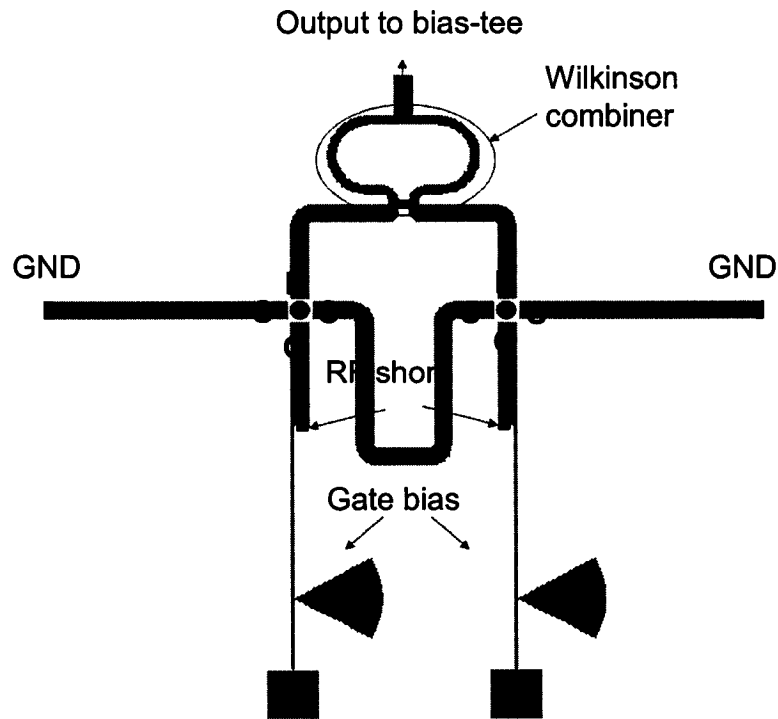
Figure 6.5: Circuit layout of the push-push oscillator

88

To determine the Fourier coefficients and phases for the waveforms, fast Fourier transform (FFT) is applied to the waveform and the results are listed in Table 6.1. The Fourier transform analysis presents large differences among the phases of all harmonics. The phase deviation of the second harmonic from the fundamental phase is approximately 29° and the phase deviation of the third harmonic is 16°. These large phase differences result in a significant asymmetry of the waveforms, leading to a larger $1/f$ noise upconversion.

The push-push oscillator with symmetrical waveforms is designed by optimizing the feedback stub length. The simulated waveforms at two drain ports of the symmetrical push-push oscillator are shown in Fig. 6.6(b). The symmetry of the rise and fall times is clearly observed except in the circled region. As mentioned earlier, the phases of all harmonics must be equal to satisfy the first waveform symmetry condition. As listed in Table 6.1, the fundamental, second, third, and fifth harmonic phases show acceptable agreements in the symmetrical push-push oscillator. Although the fourth harmonic phase has the largest deviation of 12.3° from the fundamental phase, the asymmetry effect due to the fourth harmonic is not significant because of its small amplitude. The Fourier transform analysis indicates that the asymmetry shown in the circled region in Fig. 6.6(a) is due to the third harmonic phase deviation of 5.8° from the fundamental phase.

89
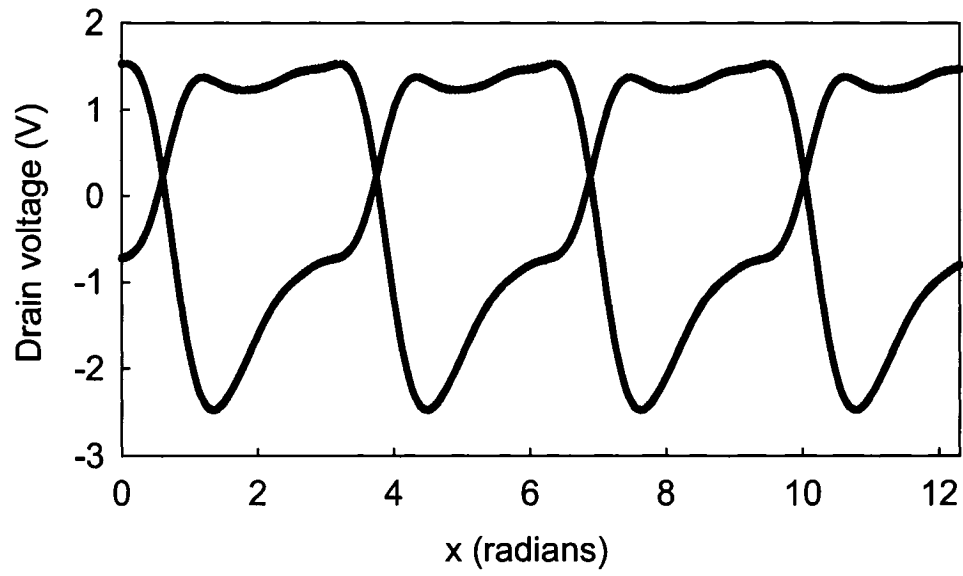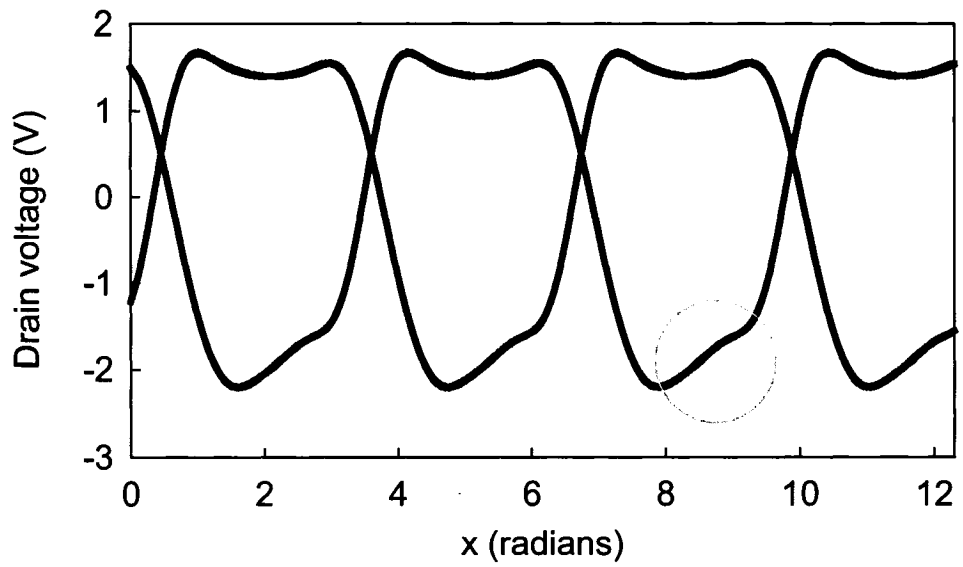
Figure 6.6: Simulated voltage waveforms at the drain ports of two push-push oscillators. (a) asymmetrical waveform. (b) symmetrical waveform.

90

Table 6.1: Fourier coefficients of the simulated waveforms in the push-push oscillators

Harmonics	Symmetrical waveform		Asymmetrical waveform	
	Amplitude	Phase(°)	Amplitude	Phase(°)
1st	1.475	114.56	1.784	115.34
2nd	-0.435	113.28	-0.48	86.55
3rd	-0.324	120.38	-0.566	131.05
4th	0.054	126.86	0.104	125.83
5th	0.008	114.45	0.154	131.70
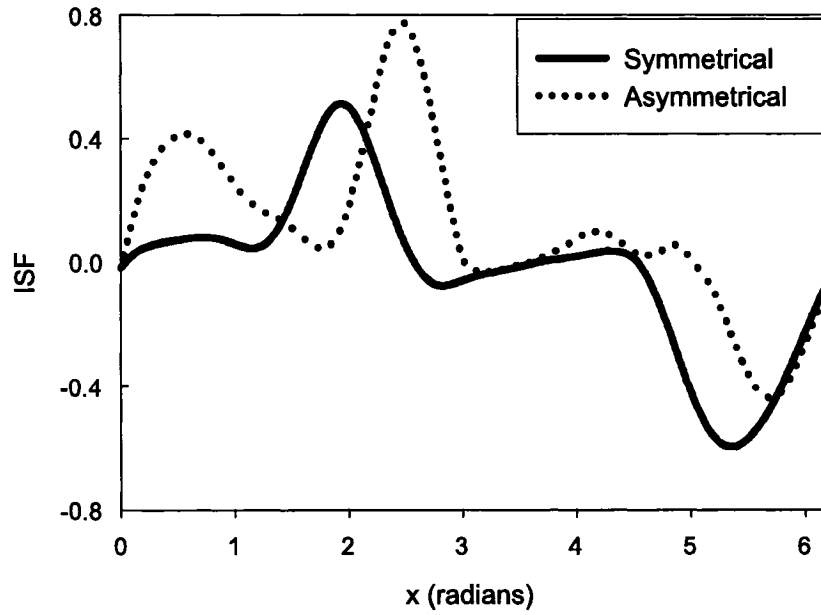
Figure 6.7: ISFs of the symmetrical and asymmetrical push-push oscillators.

To obtain the dc values of the ISFs quantitatively, the ISFs of two push-push oscillators are calculated using the analytical method introduced in [11]. Two calculated ISFs are depicted in Fig. 6.7. The dc values of the ISFs for the symmetrical and asymmetrical push-push oscillators are calculated as 0.0239 and 0.109, respectively. The ISF dc value of the asymmetrical push-push oscillator is 4.56 times larger than that of the symmetrical

push-push oscillator.

6.3.2 Triple-Push Oscillator

As previously mentioned, the second waveform symmetry condition can be satisfied in triple-push oscillators by eliminating the even harmonic components properly. One simple and effective design method to satisfy the second condition is to use the even-harmonic termination stubs in the individual sub-oscillators of a triple-push oscillator. By employing the even harmonic termination stubs, only even harmonic components are eliminated but the third harmonic power can be maintained. Therefore, the waveform symmetry can be achieved without affecting the output power.

Two triple-push oscillators with symmetrical and asymmetrical waveforms were designed in order to compare their phase noise characteristics. Fig. 6.8 shows the circuit layout of the triple-push oscillator with symmetrical waveforms. To provide a 120° phase difference, three microstrip lines at drain ports are connected. The triple-push oscillator is designed such that the center point of three connected transmission lines provides a virtual short at the fundamental and second harmonic frequencies. A coaxial cable is connected through the back side of the substrate to the circuit's center point to extract the third harmonic output power. In other words, the three microstrip lines at drain ports are used for a phase coupling network as well as power combining. As shown in Fig. 6.8, shorted stubs are employed to eliminate the second harmonic components at the drain nodes. The lengths of the shorted stubs are quarter-wavelength at the fundamental frequency. In this design, waveform symmetry is achieved by suppressing even harmonic components, thereby reducing the $1/f$ noise upconversion. In the other design, the even harmonic termination stubs are not used to evaluate $1/f$ noise upconversion and its relation to waveform symmetry.

Fig. 6.9(a) and (b) show the simulated waveforms at the drains of three devices for two triple-push oscillators. The waveforms at the device drains for the oscillator without the even-harmonic termination stubs are shown in Fig. 6.9(a), which exhibits a signifi-
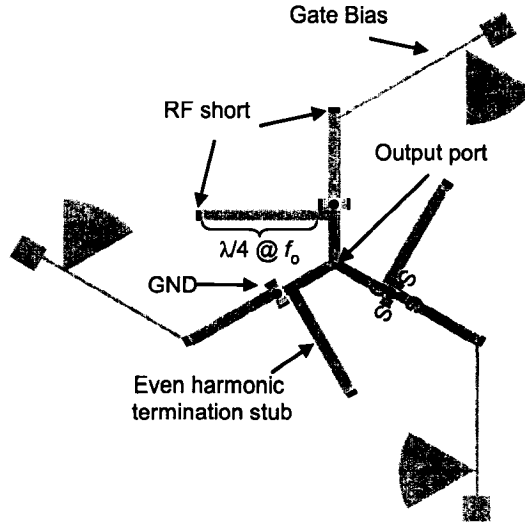
Figure 6.8: Circuit layout of the symmetrical triple-push oscillator

cant waveform asymmetry. The result of the Fourier transform analysis for the simulated waveforms is shown in Table. 6.2. In the case of the symmetrical waveforms, because the amplitudes of the even harmonic components are negligibly small, the second waveform symmetry condition is satisfied. For the asymmetrical waveforms case, the second waveform symmetry condition is, however, violated, because the second harmonic amplitude is significantly large. Moreover, the first waveform symmetry condition is also violated due to the large phase differences between the fundamental and harmonic components.

Fig. 6.10 shows the calculated ISFs for two simulated waveforms. The dc values of the ISFs for the symmetrical and asymmetrical waveforms are 0.008 and 0.195, respectively. This indicates that the asymmetrical triple-push oscillator has a much larger $1/f$ noise up-conversion factor, thereby causing increase in phase noise in the $1/f^3$ region, as compared to the symmetrical triple-push oscillator.

93
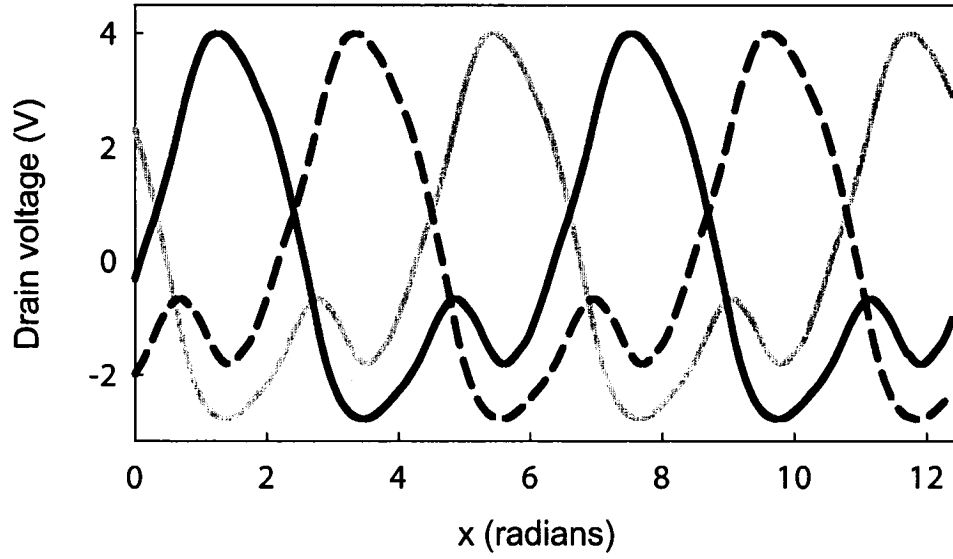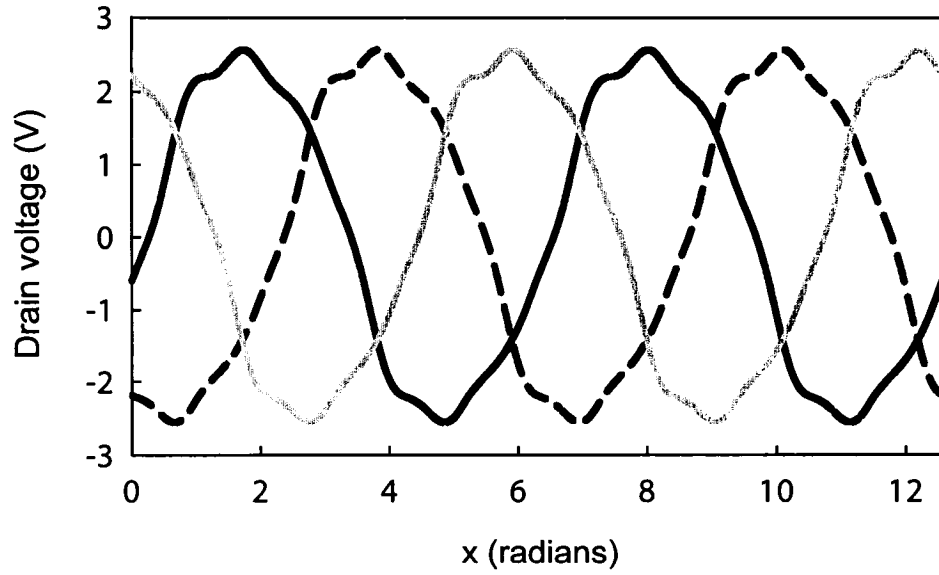
Figure 6.9: Simulated voltage waveforms at the drain ports of two triple-push oscillators.
(a) asymmetrical waveform. (b) symmetrical waveform.

94

Table 6.2: Fourier coefficients of the simulated waveforms in the triple-push oscillators

Harmonics	Symmetrical waveform		Asymmetrical waveform	
	Amplitude	Phase(°)	Amplitude	Phase(°)
1st	2.56	-100.24	2.75	79.24
2nd	0.03	-51.51	1.46	63.34
3rd	-0.19	2.23	0.22	-2.68
4th	-0.01	-8.1	-0.05	-6.76
5th	-0.08	-8.4	-0.18	12.38
6th	-0.01	11.45	-0.02	3.70
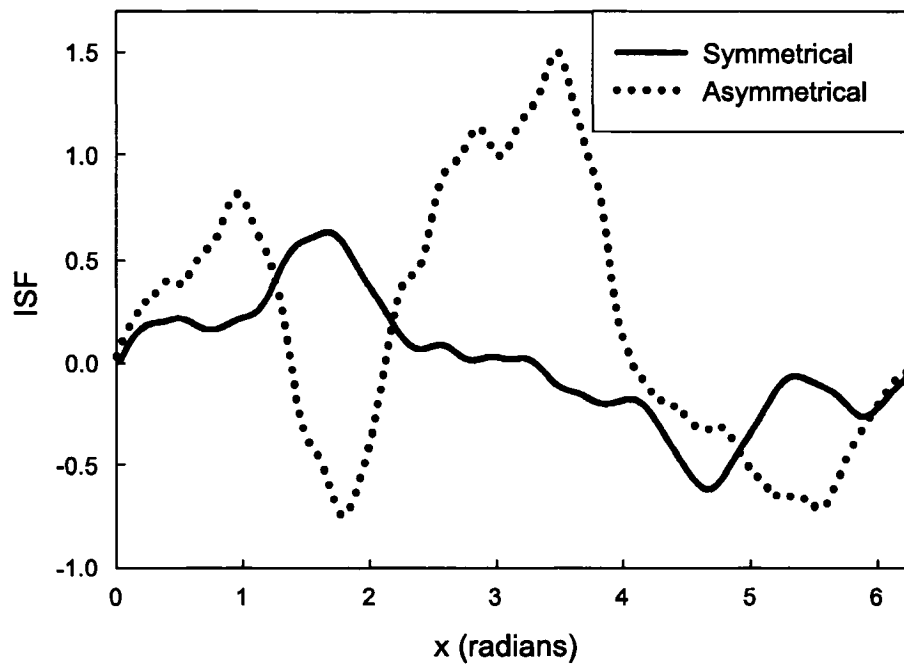
Figure 6.10: ISFs of the symmetrical and asymmetrical triple-push oscillators.

95

6.4 Experimental Results

6.4.1 Push-Push Oscillator

Two push-push oscillators with symmetrical and asymmetrical waveforms were fabricated on Rogers substrates with a dielectric constant of 3.38 and a thickness of 32 mils. Fig. 6.11 shows the photographs of the symmetrical and asymmetrical push-push oscillators, respectively. These oscillators were measured with Agilent 8564E Spectrum Analyzer. Fig. 6.12 shows the frequency spectrum of the symmetrical push-push oscillator. The measured frequency is 5.62 GHz and the output power is 2.9 dBm. Suppressions of the fundamental signal and the third harmonic signal are -20 dBc and -24 dBc, respectively. The imperfect suppressions may be attributed to fabrication errors and slight differences in the characteristics of the active devices [59]. In the asymmetrical push-push oscillator, the frequency and the output power are 5.77 GHz and 1.9 dBm. Suppressions of the fundamental signal and the third harmonic signal are -19 dBc and -18 dBc, respectively.

The phase noise of the two push-push oscillators was measured based on the FM discriminator technique using Agilent E5504A phase noise measurement system. Fig. 6.13 shows the phase noise measurement results for the two oscillators. The symmetrical push-push oscillator exhibits the $1/f^3$ phase noise corner frequency of 1.58 MHz. On the other hand, in the asymmetrical push-push oscillator, the $1/f^3$ region extends to approximately 9 MHz. This significant difference in the corner frequency indicates that the waveform symmetry contributes to reducing the $1/f$ noise upconversion and improving the phase noise in the $1/f^3$ region. Indeed, the phase noise of the symmetrical push-push oscillator is improved by 15 dB at 100 kHz offset frequency as compared to the asymmetrical push-push oscillator. At 1 MHz offset frequency, the phase noises of the symmetrical and asymmetrical push-push oscillator are -121 dBc/Hz and -109 dBc/Hz, respectively, corresponding a 12 dB reduction in phase noise. In addition, it is shown that the two phase noises are converged near 10 MHz, indicating that the waveform symmetry does not considerably affect

96

the phase noise in the $1/f^2$ region [11]. The dotted line represents the estimated phase noise improvement for the symmetrical push-push oscillator based on the simulation, which is 12 dB in the $1/f^3$ region.

Based on the time varying phase noise theory [11], the square of the dc value of the ISF is proportional to phase noise in the $1/f^3$ region. From the ISF calculation, the estimated phase noise difference in the $1/f^3$ region between the two push-push oscillators is approximately 13 dB. The measured phase noise shows 12-15 dB improvement from 10 kHz to 1 MHz, which is in very good agreement with the estimated phase noise difference based on the theory.

(a)

(b)

Figure 6.11: Photographs of the fabricated push-push oscillators (a) symmetrical push-push oscillator (b) ssymmetrical push-push oscillator

98

Figure 6.12: Frequency spectrum of the symmetrical push-push oscillator

Figure 6.13: Phase noise measurement result for the symmetrical and asymmetrical push-push oscillators. The dotted line indicates the expected phase noise improvement in $1/f^3$ region for the symmetrical oscillator based on the simulation.

99

6.4.2 Triple-Push Oscillator

Fig. 6.14 shows two triple-push oscillators fabricated on the same substrate used for the push-push oscillators. Fig. 6.15 shows the frequency spectrum of the implemented symmetrical triple-push oscillator with the even harmonic termination stubs. The measured frequency is 6.0 GHz and the output power is 0 dBm. Suppressions of the fundamental signal and the second harmonic signal are -20 dBc and -28 dBc, respectively. In the asymmetrical triple-push oscillator without the even harmonic termination stubs, the oscillation frequency and the output power are 5.85 GHz and 2 dBm. Suppressions of the fundamental signal and the third harmonic signals are -22 dBc and -22 dBc, respectively. The output power difference between the two triple-push oscillators can be attributed to the even harmonic termination and its effect on the fundamental and other harmonic power levels [60].

Phase-noise measurement results for the two triple-push oscillators are shown in Fig. 6.16. A 15 dB improvement at 100 kHz is observed in the symmetrical triple-push oscillator by suppressing the second harmonic components at the drain nodes. In the case of the symmetrical triple-push oscillator with the even harmonic termination stubs, it is observed that the effect of the device noise is dominant up to 2 MHz but the phase noise rolls off as the slope of -20 dB/dec above 2 MHz offset frequency. On the contrary, the $1/f^3$ region extends up to 10 MHz in the asymmetrical triple-push oscillator without the even-harmonic termination stubs. The dotted line represents the estimated phase noise improvement for the symmetrical triple-push oscillator from the simulation. The phase noise reduction in simulation is 26 dB in the $1/f^3$ region.

From the ISF calculation, the phase noise difference in the $1/f^3$ region for the two triple-push oscillators is expected to be approximately 28 dB. The simulated phase noise difference in the $1/f^3$ region is 26 dB. However, the measured phase noise difference is approximately 15 dB. The reason for this discrepancy can be attributed to the second harmonic power level increase in the experimental circuit compared to the simulated structure.

100

(a)

(b)

Figure 6.14: Photographs of the fabricated triple-push oscillators (a) symmetrical triple-push oscillator (b) asymmetrical triple-push oscillator
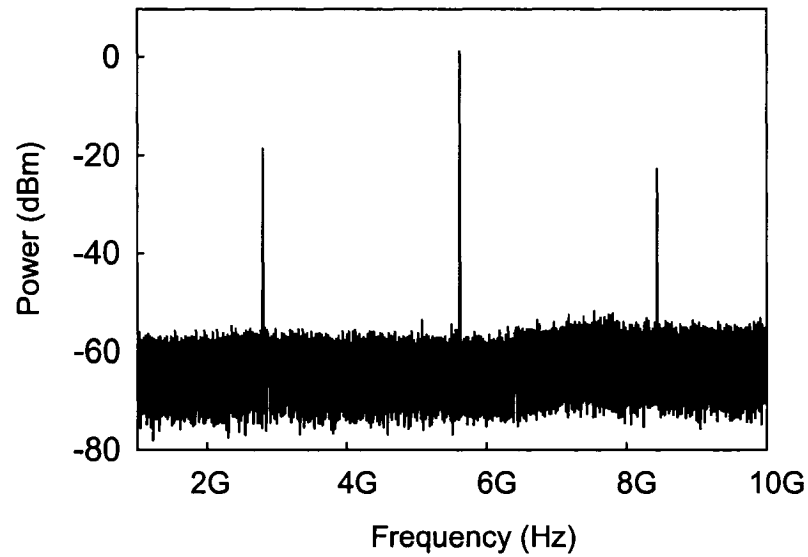
101

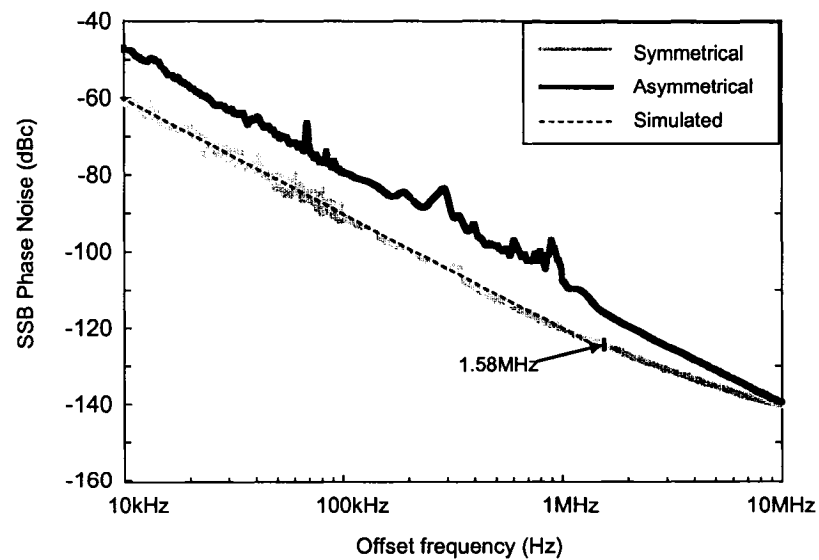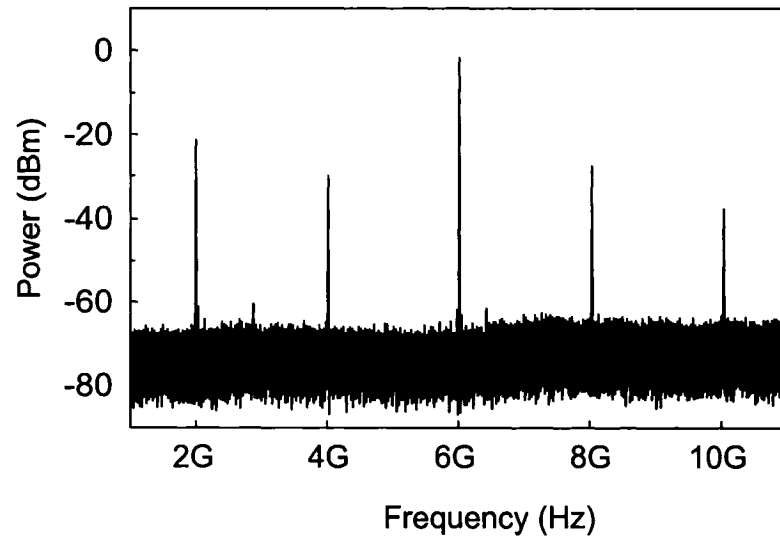Figure 6.15: Frequency spectrum of the symmetrical triple-push oscillator
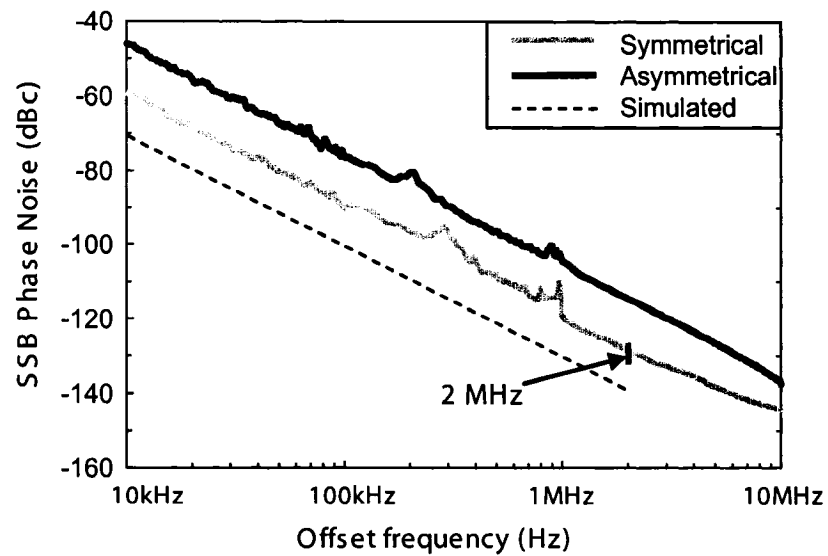
Figure 6.16: Phase-noise measurement result for the symmetrical and asymmetrical triple-push oscillators. The dotted line indicates the expected phase noise improvement in $1/f^3$ region for the symmetrical oscillator based on the simulation.

102

6.5 Conclusion

In this chapter, for the first time waveform symmetry was considered in the design of push-push and triple-push oscillators in order to minimize $1/f$ noise upconverion. Further, the design requirements for push-push and triple-push oscillators were studied.

The design methods for push-push and triple-push oscillators can be applied in conjunction with other design techniques to achieve low phase noise. For instance, low phase noise push-push oscillators can be designed employing high Q resonators such as microstrip hairpin resonator [41] and slot ring resonator [61], and then can be tuned to satisfy the first waveform symmetry condition. In the case of triple-push oscillators, the application of the proposed design technique becomes much simpler. First, a low phase-noise triple-push oscillator can be designed by employing high Q resonators, and then $1/f$ noise upconverion can be additionally reduced by adding even harmonic termination stubs.

As a proof of principle, two push-push oscillators with symmetrical and asymmetrical waveforms were fabricated. The measurement results reveal that the phase noise of the symmetrical push-push oscillator is less than that of the asymmetrical push-push oscillator by 15 dB at 100 kHz offset frequency. For the symmetrical triple-push oscillator, a 15 dB phase noise reduction at 100 kHz offset frequency was also observed, as compared to the asymmetrical triple-push oscillator. The simulation and measurement results showed that the waveform symmetry is a crucial factor in the design of push-push and triple-push oscillators because the large second harmonic signals in sub-oscillators can degrade the phase noise considerably due to the $1/f$ noise upconverion.

Chapter 7

Conclusion

7.1 Summary of Work

This thesis presented novel low phase-noise design techniques based on multiple-device and multiple-resonator oscillator topologies. These include multiple-device oscillators based on the extended resonance technique, low phase-noise oscillators employing microstrip elliptic-response bandpass filters, and push-push and triple-push oscillators with symmetrical waveforms.

In the first part of the thesis, a new low phase-noise multiple-device extended resonance oscillator was proposed. The novel feature of the proposed oscillator is that the power-dividing and -combining circuit serves to increase the oscillator Q by utilizing its filter nature. Therefore, phase noise improves beyond the 1/N rate relative to the number of devices employed due to both the high oscillator Q from cascading N resonant circuits and power combining. To validate its superiority, a SiGe HBT extended-resonance oscillator is demonstrated to produce excellent phase-noise performance (-119 dBc/Hz and -138 dBc/Hz at 100 kHz and 1 MHz offset frequencies).

In the second part of the thesis, a low phase-noise microwave oscillator employing a four-pole elliptic microstrip-line bandpass filter was presented. In elliptic filters, large group delay peaks are formed at the edges of the passband due to the transmission zeroes located in the vicinity of the passband. By designing an oscillator to perform in the vicinity of the group delay peaks, markedly low phase-noise performance can be achieved.

104

The demonstrated oscillator using a SiGe HBT packaged device evidences state of the art phase-noise performance (-116 dBc/Hz and -140 dBc/Hz at 100 kHz and 1 MHz offset frequencies) with the oscillator loaded Q of 130. The above two oscillators showed the lowest phase-noise performance that has ever been reported to date in free-running microwave planar hybrid oscillators at X band.

In the last part of the thesis, $1/f$ noise upconversion in push- and triple-push oscillators was studied, and the design requirements for minimizing $1/f$ noise upconversion were presented. In push-push oscillators, the presence of the large second harmonic components may degrade the waveform symmetry of the oscillation waveforms, leading to the significant 1/f noise upconversion. To minimize 1/f noise upconversion in push-push oscillators, the phases of Fourier coefficients of all harmonics must be equal. In triple-push oscillators, the waveform symmetry can readily be achieved by eliminating all even harmonic components. The experimental results showed that 12-15 dB phase-noise improvement at 100 kHz offset frequency were achieved by satisfying the waveform symmetry condition in push-push and triple-push oscillators.

The intellectual advantage of this thesis lies in the development of novel approaches based on the use of high-order resonant circuits to overcome phase-noise performance limit. This work may therefore improve the overall performance of microwave communication systems with a new class of low phase-noise oscillators.

7.2 Future Work

Although the design techniques proposed here are demonstrated at C-band and X-band in hybrid circuits, they are applicable to millimeter-wave low phase-noise oscillators by employing a monolithic integrated circuit format. The rapid growth of wireless communication systems demands wider bandwidths for high data-rate transmission for multimedia applications. To address this demand, the development of high-performance wireless trans-

mitter and receiver systems at millimeter-wave frequencies has experienced acceleration. In the United States, the band 38.6 - 40.0 GHz is used for licensed high-speed microwave data links, and the 60 GHz band can be used for unlicensed short range data links with data rate up to 2.5 Gbit/s, while 71-76, 81-86 and 92-95 GHz bands are also used for point-to-point high-bandwidth licensed communication links with data rates as high as 10 Gbits/s. Other applications of millimeter-wave systems can be found in automotive radar systems designed to improve road safety at 24 GHz and 77 GHz. [62]-[64]

At millimeter-wave frequencies, solid-state devices possess several fundamental limitations including their intrinsic low gain, high noise figure, and low power capability, all of which make the design of low phase-noise millimeter oscillators quite challenging. Moreover, high losses incurred from substrates is another limiting factor in oscillator performance. The design techniques proposed in this work can be expected to address these problems as follows.

7.2.1 Millimeter-wave Extended Resonance Oscillator

The extended-resonance oscillator can be designed at millimeter-wave frequencies for various applications. The excellent phase-noise performance demonstrated at the X-band is also expected at millimeter-wave frequencies. Further, the extended resonance oscillator is expected to provide high power levels through its power-combining feature. One possible solution compatible with the CMOS and BiCMOS processes is presented in Fig. 7.1. Differential circuit topology is considered by employing differential transmission lines in order to suppress common-mode substrate coupling and noise [65]. Differential gain cells will be designed to present optimum input and output admittances to maximize the overall loop group delay. For this future work, possible practical challenges related to monolithic implementation must be identified and addressed. Further, the frequency tuning capability of such oscillators needs investigation for their applications in various millimeter-wave communication and radar systems.

106

power combining extended resonance circuit

power dividing extended resonance circuit
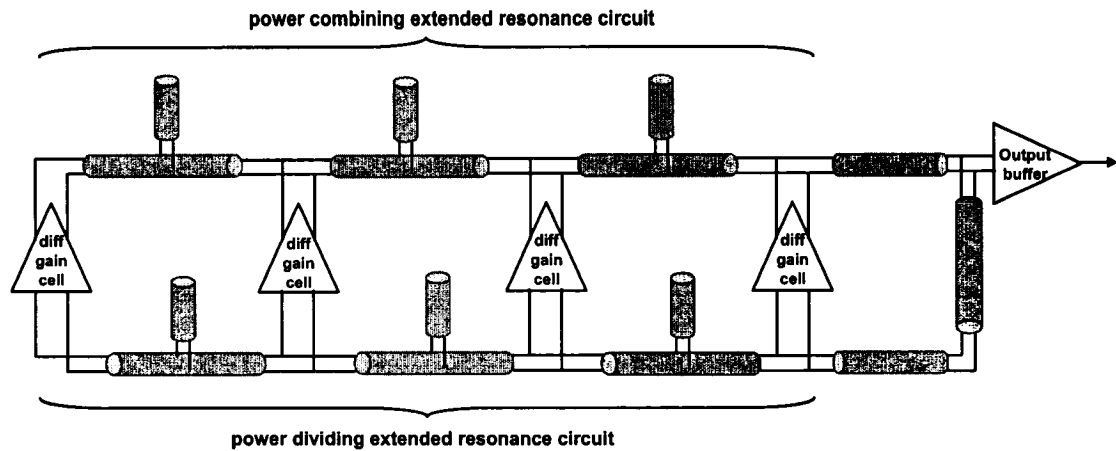
Figure 7.1: Schematic of millimeter-wave SiGe and CMOS four-device extended resonance oscillator

7.2.2 MMIC Low-Phase Noise Oscillators Employing Active Elliptic Filters

Using multiple-pole filters, millimeter-wave integrated low phase-noise oscillators can be explored. A major challenge for monolithic integration of elliptic and other types of high-order resonators lies in reducing their insertion losses at millimeter-wave frequencies. To overcome this problem, active high-order resonant circuits employing negative resistance devices can be employed in the design of low phase-noise oscillators. As shown in Fig. 7.2(a), an elliptic filter can be coupled to three negative resistance devices for loss compensation, thereby considerably increasing the group delay of the filter. A simple feedback around a transistor is used to provide negative resistance that compensates the resonator losses. The schematic of a possible millimeter-wave oscillator circuit is presented in Fig. 7.2(b). A trisection filter can be employed to achieve a high group delay peak at only one passband edge for size reduction. Each resonator is coupled with a negative resistance device (a transistor with feedback). A simple phase shifter based on varactors can be employed to provide frequency-tuning capability. In this future work, the following fundamental issues related to this oscillator design need to be addressed.

1. Stability considerations: Although the negative resistance circuit can compensate the

107
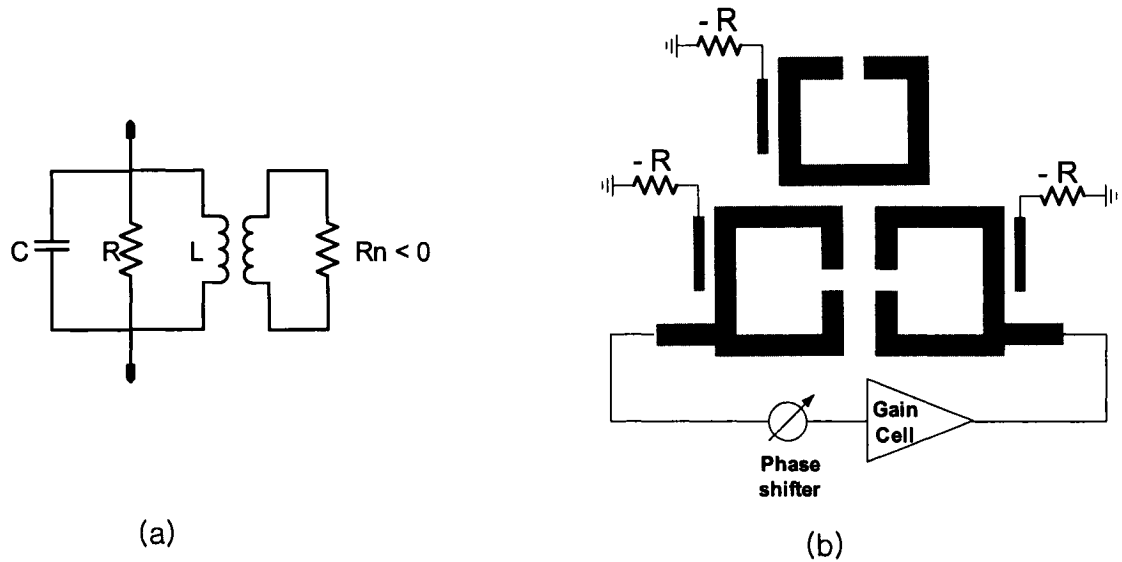
Figure 7.2: (a) Active resonator : the resonator loss is compensated by a coupled negative resistance (b) Schematic of a low phase-noise millimeter-wave oscillator using an active elliptic-filter

resonator losses, the instability issues that may arise can hinder its practical use. Because the negative resistance circuit is likely to generate another oscillation loop, instability needs to be rigorously addressed.

2. Noise considerations: Recently, a low phase noise oscillator using an active resonator has been reported [44]. This oscillator is based on a standard resonator circuit coupled to a negative resistance device and differs from the high-order resonant circuit proposed herein. However, no work has yet been conducted to identify the effect of noise generated from the negative resistance circuit and its impact on oscillator phase noise. Without a quantitative understanding of this issue, a heuristic design may result in unexpected degradation in oscillator phase-noise performance. Thus the quantitative effect of the negative resistance device noise on the overall circuit phase noise needs further investigation.

3. Filter miniaturization: In IC design, chip size directly impacts its cost. Although a quarter-wave resonator size would be quite small at millimeter-wave frequencies, the overall VCO size needs to be optimized with a mind to the cost factor.

108

Bibliography

[1] J. Choi, and A. Mortazawi, *"Microwave oscillators,"* Encyclopedia of RF and Microwave Engineering, New Jersey: J. Wiley & Sons, 2005, vol.3, pp. 2818-2827.

[2] K.Hosoya, K. Ohata, M. Funabashi, T. Inoue, and M. Kuzuhara, "V-band HJFET MMIC DROs with low phase noise, high power, and excellent temperature stability," *IEEE Trans. Microwave Theory & Tech.*, vol. 51, no. 11, pp. 2250-2258, Nov. 2003.

[3] D. B. Leeson, "A simple model of feedback oscillator noise spectrum," in *Proc. IEEE*, vol. 54, Feb. 1966, pp. 329-330.

[4] S. A. Mass, *Nonlinear microwave and RF circuits*, Boston: Artech House, 2003.

[5] A. Hajimiri and T. Lee, *The design of low noise oscillators*, Kluwer academic publishers: Boston, 2005.

[6] B. Razavi, *RF microelectronics*, Prentice Hall: New Jersey, 1998.

[7] J. Nallatamby, M. Prigent, M. Camiade, and J. J. Obregon, "Extension of the Leeson formula to phase noise calculation in transistor oscillators with complex tank," *IEEE Trans. Microwave Theory & Tech.*, vol. 51, no. 3, pp. 690-696, March, 2003.

[8] T. E. Parker, "Current developments in SAW oscillator stability," in *Proc. 31st Annu. Frequency Control Symp.*, June, 1977 pp. 359-364.

[9] W. P. Robins, *Phase noise in signal sources*, Peter Peregrinus Ltd.: London, 1982.

[10] X. S. Yao, and L. Maleki, "Multiloop optoelectronic oscillator," *IEEE J. Quantum Electron.*, vol. 36, no. 1, pp. 79-84, Jan. 2000.

[11] A. Hajimiri and T. H. Lee, "A general theory of phase noise in electrical oscillators," *IEEE J. Solid-State Circuits*, vol. 33, no. 2, pp. 179-194, Feb. 1998.

[12] E. L. Holzman, *Solid-state microwave power oscillator design*, Artech house: Boston, 1992.

[13] K. Chang and C. Sun, "Millimeter-wave power combining technique," *IEEE Trans. Microwave Theory & Tech.*, vol. MTT-31, pp. 91-107, Feb. 1983.

[14] M. M. Driscoll, "Low noise oscillator design and performance," presented at *IEEE Frequency Control Symp.*, New Orleans, LA, June 2002.

109

[15] K. Kurokawa, and F. M. Magalhaes, "An X-band 10-watt multiple-IMPATT oscillator," *Proc. IEEE*, vol. 59, pp. 102-103, Oct. 1971.

[16] K. Kurokawa, "The single-cavity multiple-device oscillator," *IEEE Trans. Microwave Theory & Tech.*, vol. 19, pp. 793-801, Oct. 1971.

[17] R. Adler, "A study of locking phenomena in oscillators," *Proc. IRE*, vol. 34, pp. 351-357, June 1946 (reprinted *Proc. IRE*, vol. 61, pp.1380-1385, Oct. 1973).

[18] R. A. York, and T. Itoh, "Injection- and phase-locking techniques for beam control," *IEEE Trans. Microwave Theory & Tech.*, vol. 46, no. 11, pp. 1920-1929, Nov. 1998.

[19] H. Chang, X. Cao, U. Mishra, and R. A. York, "Phase noise in coupled oscillators: Theory and Experiment," *IEEE Trans. Microwave Theory & Tech.*, vol. 45, no. 5, pp. 604-615, May. 1997.

[20] T. Makino, M. Nakajima, and J. Ikenoue, "Noise reduction mechanism of a power combining oscillator system," *Elect. Commun. Jap.*, vol. 62-B, no. 4, pp. 37-44, May. 1979.

[21] M. M. Driscoll, "A SAWR oscillator vibration sensitivity and phase noise reduction technique using multiple resonators and RF outputs," in *Proc. 50st Annu. Frequency Control Symp.*, May, 1995, pp. 514-518.

[22] J. van der Tang, P. van de Ven, D. Kasperkovitz, and A. van Roermund, "Analysis and design of an optimally couple 5-GHz quadrature LC oscillator," *IEEE J. Solid-State Circuits*, vol. 37, no. 5, pp. 657-661, May. 2002.

[23] M. M. Driscoll, "The use of multi-pole bandpass filters and other multiple resonator circuitry as oscillator frequency stabilization elements," in *Proc. 50st Annu. Frequency Control Symp.*, June, 1996, pp. 782-789.

[24] J. Choi, and A. Mortazawi, *"Microwave oscillators,"* Encyclopedia of RF and Microwave Engineering, New Jersey: J. Wiley & Sons, 2005, vol.3, pp. 2818-2827.

[25] S. Qi, K. Wu, and Z. Ou, "Hybrid integrate HEMT oscillator with a multiple-ring nonradiative dielectric resonator feedback circuit," *IEEE Trans. Microwave Theory & Tech.*, vol. 46, no. 10, pp. 1552-1558, Oct. 1998.

[26] J. Choi, and A. Mortazawi, "A novel multiple-device low phase noise oscillator based on the extended resonance technique,", in *IEEE MTT-S Int. Microwave Symp. Dig.*, San Francisco, CA, 2006, pp. 577-580.

[27] A. Martin, A. Mortazawi, and B. C. De Loach, Jr., "An eight-device extended-resonance power-combining amplifier," *IEEE Trans. Microwave Theory & Tech.*, vol. 46, no. 6, pp. 844-850, June 1998.

[28] A. Martin, and A. Mortazawi, "A class-E power amplifier based on an extended resonance technique," *IEEE Trans. Microwave Theory & Tech.*, vol. 48, no. 1, pp. 93-97, Jan. 2000.

110

[29] A. Mortazawi, and B. C. De Loach, Jr., "Multiple element oscillators utilizing a new power combining technique," *IEEE Trans. Microwave Theory & Tech.*, vol. 40, no. 12, pp. 2397-2402, Dec. 1992.

[30] K. L. Kotzebue, "A technique for the design of microwave transistor oscillator," *IEEE Trans. Microwave Theory & Tech.*, vol. 32, pp. 719-721, July 1984.

[31] M. Lee, S. Yi, S. Nam, Y. Kwon, and K. Yeom, "High-efficiency harmonic loaded oscillator with low bias using a nonlinear design approach," *IEEE Trans. Microwave Theory & Tech.*, vol. 47, no. 9, pp. 1670-1679, Sep. 1999.

[32] M. Tiebout, "Low-power low-phase-noise differentially tuned quadrature VCO design in standard CMOS," *IEEE J. Solid-State Circuits*, vol. 36, no. 7, pp. 1018-1024, July 2001.

[33] Y.-T. Lee, J. Lee, and S. Nam, "A new phase noise reduction method of oscillator by loaded Q improvement using dual feedback topology," *IEEE Microw. Wireless Compon. Lett.*, vol. 15, no. 1, pp. 39-41, Jan. 2005.

[34] J. Jung, and C. S. Cho, J. W. Lee, J. Kim, and T. H. Kim "A low phase noise microwave oscillator using split ring resonators,", in *Proc. 36th Eur. Microw. Conf.*, Manchester, UK, 2006, pp. 95-98.

[35] Y.-T. Lee, J.-S. Lim, C.-S. Kim, D. Ahn and S. Nam, "A compact-size microstrip spiral resonator and its application to microwave oscillator," *IEEE Microw. Wireless Compon. Lett.*, vol. 12, no. 10, pp. 375-377, Oct. 2002.

[36] J. Hong, and M. J. Lancaster, *Microstrip filters for RF/microwave applications*, New York: J. Wiley & Sons, 2001.

[37] R. S. Kwok, and J. -F. Liang, "Characterization of high-Q resonators for microwave-filter applications," *IEEE Trans. Microwave Theory & Tech.*, vol. 47, no. 1, pp. 111-113, Jan. 1999.

[38] A. E. Atia and A. E. Williams, "Measurements of intercavity couplings," *IEEE Trans. Microwave Theory & Tech.*, vol. 23, no. 6, pp. 519-522, June 1975.

[39] J. S. Hong, and M. J. Lancaster, "Theory and experiment of novel microstrip slow-wave open-loop resonator filters," *IEEE Trans. Microwave Theory & Tech.*, vol. 45, no. 12, pp. 2358-2365, Dec. 1997.

[40] Y. Cassivi and K. Wu, "Low cost microwave oscillator using substrate integrated waveguide cavity," *IEEE Microwave Wireless Compom. Lett.*, vol. 13, pp. 48-50, Feb. 2003.

[41] L. Dussopt, D. Guillois, and G. M. Rebeiz, "A low phase noise silicon 9 GHz VCO and 18 GHz push-push oscillator," in *IEEE MTT-S Int. Microwave Symp. Dig.*, vol. 2, June 2002, pp. 695-698.

111

[42] A. P. S. Khanna, E. Topacio, E. Gane, and D. Elad, "Low jitter silicon bipolar based VCO's for applications in high speed optical communication systems," in *IEEE MTT-S Int. Microwave Symp. Dig.*, vol. 3, May 2001, pp. 1567-1570.

[43] L.-H. Hsieh, and K. Chang, "High-efficiency piezoelectric-transducer tuned feedback microstrip ring-resonator oscillators operating at high resonant frequecies," *IEEE Trans. Microwave Theory & Tech.*, vol. 51, pp. 1141-1145, Apr. 2003.

[44] Y.-T. Lee, J. Lee, and S. Nam, "High-Q active resonators using amplifiers and their applications to low phase noise free-running and voltage-controlled oscillators," *IEEE Trans. Microwave Theory & Tech.*, vol. 52, no. 11, pp. 2621-2626, Nov. 2004.

[45] E. Park, and C. Seo, "Low phase noise oscillator using microstrip square open loop resonator,", in *IEEE MTT-S Int. Microwave Symp. Dig.*, San Francisco, CA, 2006, pp. 585-588.

[46] J. S. Hong, and M. J. Lancaster, "Compact microwave elliptic function filter using novel microstrip meander open-loop resonators," *Electron. Lett.*, vol. 32, no.6, pp. 563-564, Mar. 1996.

[47] M. Sagawo, K. Takahashi, and M. Makimoto, "Miniatuized hairpin resonator filters and their application to receiver front-end MICs," *IEEE Trans. Microwave Theory & Tech.*, vol. 37, no. 12, pp. 1991-1997, Dec. 1989.

[48] J. Gu, F. Zhang, C. Wang, Z. Zhang, M. Qi and X. Sun, "Miniaturization and Harmonic Suppression Open-loop Resonator Bandpass Filter with Capacitive Terminations,", in *IEEE MTT-S Int. Microwave Symp. Dig.*, San Francisco, CA, Jun. 2006, pp. 373-376.

[49] J. R. Bender et. al., "Push-push design extends bipolar frequency range,", *Micro RF*, vol. 22, pp. 91-98, Oct. 1983.

[50] F. X. Sinnesbichler, "Hybrid millimeter-wave push-push oscillators using silicon-germanium HBTs," *IEEE Trans. Microwave Theory & Tech.*, vol. 51, no. 2, pp. 422-430, Feb. 2003.

[51] Y. Tang, and H. Wang, "Triple-push oscillator approach: Theory and experiments," *IEEE J. Solid-State Circuits*, vol. 36, no. 10, pp. 1472-1479, Oct. 2001.

[52] K. W. Kobayashi, A. K. Oki, L. T. Tran, J. C. Cowles, A. Gutierrez-Aitken, F. Yamada, T. R. Block and D. C. Streit, "A 108-GHz InP-HBT monolithic push-push VCO with low phase noise and wide tuning bandwidth," *IEEE J. Solid-State Circuits*, vol. 34, no. 9, pp. 1225-1232, Sep. 1999.

[53] J. E. Post, Jr., I. R. Linscott, and M. H. Oslick, "Waveform symmetry properties and phase noise in oscillators," *Electron. Lett.*, vol. 34, no. 16, pp. 1547-1548, Aug. 1998.

112

[54] D. K. Shaeffer and S. Kudszus, "Performance-optimized microstrip coupled VCOs for 40-GHz and 43-GHz OC-768 optical transmission," *IEEE J. Solid-State Circuits*, vol. 38, no. 7, pp. 1130-1138, July 2003.

[55] J. Choi and A. Mortazawi, "Design of push-push oscillators for reducing 1/f noise upconversion,", in *IEEE MTT-S Int. Microwave Symp. Dig.*, Long Beach, CA, Jun. 2005, pp. 1531-1534.

[56] J. Choi and A. Mortazawi, "Design of push-push and triple-push oscillators for reducing 1/f noise upconversion," *IEEE Trans. Microwave Theory & Tech.*, vol. 53, no. 11, pp. 3407-3414, Nov. 2005.

[57] H. B. Chen, A. van der Ziel, and K. Amberiadis, "Oscillator with odd-symmetrical characteristics eliminates low-frequency noise sidebands," *IEEE Trans. Circuits Syst.*, vol. 31, no. 9, pp. 807-809, Sep. 1984.

[58] B. Hughes, N. G. Fernandez and J. M. Gladstone, "GaAs FET's with a Flicker-Noise Corner below 1MHz," *IEEE Trans. Electron Devices*, vol. 34, no. 4, pp. 733-741, Apr. 1987.

[59] F. X. Sinnesbichler and H. Geltinger and G. R. Olbrich, "A 38-GHz push-push oscillator based on 25-GHz fT BJT's," *IEEE Microwave Guided Wave Lett.*, vol. 9, no. 4, pp. 151-153, Apr. 1999.

[60] P. Berini, M. Desgagne, F. M. Ghannouchi, and R. G. Bosisio, "An experimental study of the effects of harmonic loading on microwave MESFET oscillators and amplifiers," *IEEE Trans. Microwave Theory & Tech.*, vol. 42, no. 6, pp. 943-950, Jun. 1994.

[61] H. Xiao, T. Tanaka and M. Aikawa, "A low phase noise Ku-band push-push oscillatr using slot ring resonator," in *IEEE MTT-S Int. Microwave Symp. Dig.*, Jun. 2004, pp. 1333-1336.

[62] B. Razavi, "A 60-GHz CMOS receiver front-end," *IEEE J. Solid-State Circuits*, vol. 41, no. 1, pp. 17-22, Jan. 2006.

[63] C. H. Doan, S. Emami, D. A. Sobel, A. M. Niknejad, and R. W. Brodersen, "A 60-GHz CMOS receiver front-end," *IEEE Communications Magazine*, pp. 17-140, Dec. 2004.

[64] I. Gresham, N. Jain, T. Budka, A. Alexanian, N. Kinayman, B. Ziegner, S. Brown, and P. Staecker, "A compact manufacturable 76-77 GHz radar module for commercial ACC applications," *IEEE Trans. Microwave Theory & Tech.*, vol. 49, no. 1, pp. 44-58, Jan. 2001.

[65] D. Guckenberger, and K. T. Kornegay, "Design of a differential distributed amplifier and oscillator using close-packed interleaved transmission lines," *IEEE J. Solid-State Circuits*, vol. 40, no. 10, pp. 1997-2007, Oct. 2005.

113

[66] M. Ito, K. Maruhashi, S. Kishimoto, and K. Ohata, "60-GHz band coplanar MMIC active filters," *IEEE Trans. Microwave Theory & Tech.*, vol. 52, no. 3, pp. 743-750, Mar. 2004.